Collective atom-light interactions with Rydberg superatoms

Nina Stiesdal

PhD dissertation

February 2022

Supervisor:
Sebastian Hofferberth, University of Southern Denmark and University of Bonn

Committee
Mads Thoudal Frandsen, University of Southern Denmark
Klaus Mølmer, Aarhus University
Tilman Pfau, University of Stuttgart

SDU

**UNIVERSITY OF
SOUTHERN DENMARK**

Resumé

Rydberg superatomer hvor $N \gg 1$ enkelte atomer deler en enkelt excitation udgør en platform, hvor det er muligt at etablere stærk kobling mellem en effektiv emitter og et felt med få fotoner. Denne kobling er mulig fordi Rydbergblokaden begrænser antallet af excitationer i et ensemble af ultrakolde atomer til en enkelt, og dermed omdannes ensemblet til et effektivt to-niveau-system. Excitationens kollektive karakter giver anledning til forstærket kobling mellem det effektive to-niveau-system og et drivende elektromagnetisk felt, og de faser, som dette felt præge de enkelte atomers fase, leder til en stærk ensretning af superatomets stråling tilbage i samme retning som det drivende felt. Dette projekt beskriver observation af kohærent indre dynamik i et Rydberg superatom og demonstrerer kontrolleret multifotonabsorption med en kæde af Rydberg superatomer. Vi observerer effekten af indre dynamik i superatomets kollektive enkeltfotonstråling efter en drivende puls. Vi observerer, at strålingsraten oscillerer som funktion af pulslængden, frem for at være konstant og bestemt af den kollektive koblingsstyrke til det drivende felt.

Denne observation indikerer, at strålingsraten afhænger af superatomets indre tilstand, og vi tilskriver denne afhængighed til en kohærent kobling mellem de N forskellige kollektive tilstande med en enkelt excitation.

For at opnå kontrolleret og præcis absorption af op til tre fotoner implementerer vi et kaskadesystem af op til tre superatomer. I dette tilfælde udnytter vi det faktum, at superatomerne opfører sig som absorbanter, der mættes ved absorption af en enkelt foton. Ved at maksimere raten for tab af faseinformation kan vi overføre den kollektive excitation fra den stærkt koblede tilstand med ensrettet stråling til tilstande, som ikke er koblet til lyset. Disse tilstande henfalder med henfaldsraten for et enkelt atom, men de er stadig exciterede, og derfor blokerer de superatomet for nye excitationer.

Afslutningsvist giver vi en perspektivering på, hvordan systemet diskuteret her kan optimeres, så fasetabet minimeres for med henblik på eksperimentelt observere vekselvirkninger imellem superatomerne. En sådan vekselvirkning vil være medieret af den ensrettede udveksling af fotoner langs det drivende felts mode, som effektivt udgør en ensrettet bølgeleder.

Abstract

Rydberg superatoms in which $N \gg 1$ individual atoms collectively share a single excitation offer a platform to realize strong coupling between an effective two-level quantum emitter and few-photon fields. This is possible as the Rydberg blockade limits the number of excitations in an ensemble of ultracold atoms to one, thereby effectively forming a two-level system. The collective nature of the excitation gives rise to the strongly enhanced coupling and the phase imprinted on the individual constituent atoms by the driving fields leads to a strong directionality of the superatom's emission back into the driving mode. This thesis reports on the observation of coherent internal dynamics within a superatom and the demonstration of controlled multi-photon absorption using a chain of cascaded Rydberg superatoms.

The effects of the internal dynamics are observed in the superatom's collective emission of a photon into the driving mode. As we change the length of the driving pulse, we observe oscillations in the decay rate instead of constant decay determined by the collective coupling strength to the driving field. This indicates a dependence on the internal dynamics of the decay, which we attribute to a coherent coupling between the N singly excited collective states of a superatom.

To realize controlled and exact absorption of up to three photons, we implement a cascaded system of up to three superatoms. Here, we exploit the fact that they act as absorbers that are saturated following absorption of a single photon. By maximizing the dephasing of the superatom, we transfer the collective excitation from a strongly coupled and directionally emitting collective bright state to dark states that are not coupled to the forward mode, but still excited such that the blockade prevents absorption of further photons.

Finally, this thesis gives an outlook on how to optimize our system of cascaded superatoms in the limit of weak dephasing to experimentally observe interactions between multiple superatoms, which are mediated by directional photon exchange along the probe mode, which effectively forms a chiral waveguide.

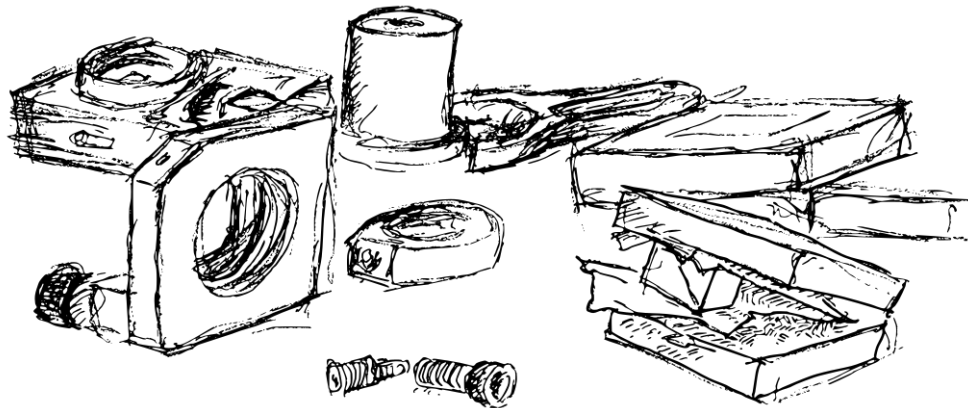**This thesis is based on the following publications:**

N. Stiesdal, H. Busche, J. Kumlin, K. Kleinbeck, H.P. Büchler, and S. Hofferberth:
Observation of collective decay dynamics of a single Rydberg superatom
Physical Review Research, 2, 043339 (2020), arXiv:2005.05089

N. Stiesdal., H. Busche, K. Kleinbeck, J. Kumlin, M.G. Hansen, H.P. Büchler, and S. Hofferberth:
Controlled multi-photon subtraction with cascaded Rydberg superatoms as single-photon absorbers
Nature Communications, 12, 4328 (2021), arXiv:2103.15738

Other publications:

N. Stiesdal., J. Kumlin, K. Kleinbeck, P. Lunt, C. Braun, A. Paris-Mandoki, C. Tresp, H.P. Büchler, and S. Hofferberth:
Observation of Three-Body Correlations for Photons Coupled to a Rydberg Superatom
Physical Review Letters, 121, 103601 (2018), arXiv:1806.00062

J. Kumlin, K. Kleinbeck, N. Stiesdal., H. Busche, S. Hofferberth, and H.P. Büchler
Nonexponential decay of a collective excitation in an atomic ensemble coupled to a one-dimensional waveguide
Physical Review A, 102, 063703 (2020), arXiv:2006.14977

Contents

Chapter 1

Introduction

The interaction of electromagnetic radiation with matter is one of the most fundamental processes in nature. The early universe expanded through radiation pressure, energy transfer through photosynthesis enables life as we know it on Earth, and the interaction between light and matter is essential for our perception of the world.

The most basic form of light-matter interaction is that of a single photon with a single quantum emitter, such as an atom. This interaction can be described by quantum mechanics which was developed over the last 100 years, in particular quantum electrodynamics. The development of lasers in the 1960s has opened new ways of exploring light-matter interactions experimentally [1]. It has also led to the development of central techniques in modern atomic physics such as laser cooling and optical trapping of atoms [2–5]. These developments have facilitated a high degree of control over quantum systems even down to the single-photon and single-atom level [6, 7].

The simplest approach to describing a bulk-medium interacting with light is to describe the medium as a sum of N independent emitters interacting with the light without affecting each other. This approach is sufficient for many purposes, in particular if there is no interaction between the constituent emitters. In other cases, however, this approach is too simplistic, even in the absence of direct emitter-emitter interaction [8].

Picturing two atoms as classical radiating dipoles, the fields that they emit will eventually overlap and interfere. Depending on the relative phase of the fields, the interference can either be constructive or destructive. The same is the case for ensembles of atoms. Even without direct atom-atom-interaction, the emission from many excited atoms will overlap and interfere. In 1956 Dicke pointed out that the collective emission from several two-level quantum emitters can occur at different rates compared to individual emitters as the presence of other emitters alters the environment into which a given emitter radiates [9]. Constructive and destructive interference effects lead to enhanced or suppressed emission, famously known as super- and subradiance respectively.

Superradiance effects have been widely studied for a wide range of emitters. The first observation of superradiance in the optical domain was reported in a hot atomic vapor in 1973 [10]. An overview of early theoretical and experimental work can be found in the reviews by Andreev, Emel'yanov, and Il'inskiĭ [11] and Gross and Haroche [12].

Subradiance, the elusive flipside of superradiance, has not received as much attention, in part due to the difficulties related to preparing emitters in collective states which couple only weakly to light-fields if at all. Observations have been made in hot atomic vapors and with a pair of ions [13, 14], and more recently in ultracold atomic ensembles [15, 16].

In the past years collective atom-light interactions have been studied in an increasing number of contexts, for example in disordered systems, such as small and dense cold atom ensembles [17–19], ordered atomic ensembles [20], between molecules [21, 22], in dense hot atomic vapors [23, 24], in alkali-earth-atoms with narrow-linewidth transitions [25], between nuclei [26] and between trapped ions [27]. The recent progress in preparing large structured arrays of individual atoms in optical tweezers or lattices [28–31] has inspired proposals to engineer optical media consisting of emitters with well-defined spacing and geometry, that exploit collective effects to achieve enhanced an optical response. Applications include absorbers and mirrors formed by just a few tens of emitters in two-dimensional [32–36] and enhanced photon storage in subradiant emitter chains [37, 38]. A first proof of principle of a subradiant mirror has recently been demonstrated [39].

This approach of modifying the electromagnetic environment of the emitters through the presence of other emitters is related to cavity electrodynamics, where the environment is modified by placing an emitter inside a resonator, where its coupling to resonator modes is enhanced by its mirror image [40, 41].

In analogy to the resonator, the number of optical modes with which emitters can interact can be reduced by coupling the emitters to a waveguide. Examples include tapered optical nanofibers, hollow-core fibers, integrated optical and even superconducting microwave waveguides [42–52].

In the latter case, the emitters are not atoms, but superconducting qubits. More generally waveguide quantum electrodynamics can be realized with any quantum-emitter, such as molecules, quantum dots, and color centers [53–56].

This thesis focuses on another kind of effective quantum emitter that is based on collective excitation: Rydberg superatoms [57]. The superatom is made of N individual ultracold atoms in a strongly confined ensemble which are coupled to a Rydberg state. The strong interactions between Rydberg atoms lead to an excitation blockade that limits the number of possible excitations to a single one that is collectively shared by all N atoms [58]. By coupling to the Rydberg state in a two-photon Raman scheme, the Rydberg superatom becomes an effective two-level system [59–63]. The limitation to a single collective excitation turns the superatom into a perfectly nonlinear two-level system, similar to an individual atom.

Rydberg atoms have generally been highly successful tools for quantum nonlinear optics [64, 65]. They can be used to observe highly nonclassical states of light [66–69], and to implement devices such as photon-photon quantum gates [70], single photon switches and transistors [71–75], and single photon sources [76, 77]. Rydberg superatoms as discussed above have been used to realize single photon absorbers, removing a single photon from a probe pulse [78].

This application is possible because the collective nature of the excitation leads to a strongly enhanced coupling between the superatom and few-photon probe fields in the presence of a strong control field. The existence of well-defined phase relations between the individual constituent atoms leads to a strongly enhanced directional coupling to the single optical mode of the probe field in the forward direction. Hence, the combination of the superatom and the mode of the probe field effectively acts as a single quantum emitter coupled to a one-dimensional directional waveguide [42]. The coupling strength between the superatom and this effective waveguide is determined by the number of atoms contributing to the collective state, scaling as $\sqrt{N}$. Given that N typically is on the order of 10^4, the emitter-waveguide coupling is strong compared to many other systems. The directionality allows us to realize chained systems of multiple superatoms interacting with the same waveguide by simply placing multiple atomic ensembles into the path of a single probe field.

This thesis begins with a brief review of the theoretical background for collective effects.

We discuss the collective states of many atoms sharing a single excitation as in the Rydberg superatom. We also highlight how Rydberg superatoms can be treated in the language of waveguide QED when they are formed in a trap.

Based on this theoretical discussion, we continue with a description of how we experimentally realize the Rydberg superatoms in the form of ensembles ultracold rubidium atoms trapped in optical dipole traps. The experimental setup allows us to realize multiple superatoms in series. Therefore, we analyze the collective dynamics of a multi-superatom system where interaction between superatoms is mediated by the unidirectional emission from single superatoms into the mode defined by the probe field.

While we predict effects of collective states of many superatoms coupled to the same field, the Rydberg superatoms themselves are also formed by a collective excitation shared between many emitters. Therefore, we experimentally investigate the internal dynamics of a single superatom by considering the emission from the superatom after exposure to a driving field. This emission depends on the collective state of the constituent atoms.

We expand the system to a chain of up to three Rydberg superatoms and demonstrate that this system can be applied as a multi-photon subtractor when the system parameters are optimized for this application: The subtraction relies on storage in a dephased state and requires high dephasing rate.

Finally, we consider how to optimize the system parameters for the opposite regime, where dephasing is minimal. In this regime we hope to implement a chain of Rydberg superatoms as a cascaded quantum system.

Chapter 2

Collective light-matter interactions

When describing systems of many atoms, it is often considered sufficient to treat all atoms as being independent. However, this approach neglects that emitters influence and thus modify the emission characteristics of each other, and as a consequence it does not always lead to correct results. In 1954 Dicke demonstrated, that a single excited two-level neutron behaves fundamentally different depending on whether it is alone or a second, unexcited, neutron is nearby [9]. Furthermore, Dicke described how an ensemble of N emitters can emit with a strongly modified and drastically higher emission rate compared to N individual emitters. Dicke called this effect superradiance. Since the publication of Dicke's seminal paper almost 70 years ago the collective effects of many identical emitters have been intensively studied.

The superradiance can be intuitively understood in a classical framework by treating each emitter as an oscillating dipole with a fixed phase. When the small dipoles are oscillating in phase, the emitted field is subject to constructive interference and the resulting response is a stronger emission signal - superradiance. On the other hand, the dipoles can also oscillate out of phase, which leads to destructive interference and weaker emission - subradiance. This picture of an interplay between many small radiators may be instructive for imagining these effects. In reality, the effects have a quantum origin and are caused by exchange of virtual photons mediating dipole-dipole interaction between the emitters [79].

In the scope of this thesis, we will primarily be concerned with the case of a single excitation shared collectively by $N \gg 1$ atoms. This regime has recently experienced a renewed interest particularly in the years from 2006 and until today with extensive work from among many others Scully and Svidzinsky [80–82], Friedberg and Manassah [83, 84], Kurizki [85], and Agarwal [86].

To develop an intuition for the collective effects, it is instructive to consider a two-atom system compared to a single atom, as we will do in the first section of this chapter. Next, the introduction is extended to two two-level atoms and to a discussion of collective effects when more than a single atom is considered. In particular, we consider how the exchange of virtual photons can mediate emitter-emitter interaction and drastically change the behavior of many-emitter systems for even few collective excitations. For instance, such collective excitations can have enhanced coupling strengths to certain fields and strongly directional spontaneous emission.

The enhanced coupling to certain modes makes the collective excitations discussed here resemble waveguide systems. Therefore, we also shortly review of the dynamics of many emitters coupled to waveguides. In particular we consider how a waveguide can mediate emitter-emitter interactions even over long distances. It is important to note that there are

many effects which can be described as collective, and which give rise to modified emission rate. For a discussion of terminology, we refer to [8] In this thesis, we focus exclusively on the super- and subradiant collective states with few excitations shared between many emitters.

2.1 Two-atom collective states

The simplest system for observation of collective effects is a set of two coupled emitters. This system has been studied in great detail [87–89]. See also, for instance, the introduction of ref. [90]. In this section we briefly consider such a system as a basis for the further analysis.

Individually, the single atoms are described with the two states $|g\rangle$ for the ground state, and $|e\rangle$ for the excited state, and the single atom is assumed to decay from $|e\rangle \to |g\rangle$ with decay rate given by the natural linewidth Γ. This decay is described by the jump operator $\sigma = |g\rangle \langle e|$. In the density matrix formalism for a single emitter, the decay can be described by the density matrix element ρ_{ee} following from the Optical Bloch equations [91]

$$\rho_{ee}(t) = \rho_{ee}(0)e^{-\Gamma t} \tag{2.1}$$

$$\rho_{gg}(t) = 1 - \rho_{ee}(0)e^{-\Gamma t} \tag{2.2}$$

$$\rho_{ge}(t) = \rho_{eg}^*(t) = \rho_{ge}(0)e^{-\frac{\Gamma}{2}t}. \tag{2.3}$$

The last equation shows how any initial coherences also decay with Γ, and in particular how the coherences are independent of the populations in the case of pure decay. This indicates that coherence cannot be established in a decaying two-level system.

The decay of the system is described by considering the expectation value of the jump operators [92]:

$$W(t) = \langle \sigma^\dagger \sigma \rangle. \tag{2.4}$$

If the system starts in the excited state, it emits with

$$W(t) = \exp(-\Gamma t). \tag{2.5}$$

Next, we consider the case of two atoms. The dimensionality of the combined Hilbert space is four, spanned by the pair states given by both atoms in the ground state, $|gg\rangle$, two single-excitation states $|eg\rangle, |ge\rangle$, and the doubly excited state $|ee\rangle$.

It is assumed that the atoms are far enough apart to ensure that they do not have overlapping wavefunctions. It is further assumed that they are stationary and coupled only via radiation [87–89]. Finally, it is assumed that the atoms are much closer than the wavelength of the transition $|e\rangle \leftrightarrow |g\rangle$. In the absence of any coupling, the single-excitation states are degenerate. However, there is a dipole-moment between the states

$$\langle eg| \vec{D} |ge\rangle = \langle e_1| \vec{d_1} |g_1\rangle + \langle g_2| \vec{d_2} |e_2\rangle \tag{2.6}$$

where $\vec{D}$ is the dipole operator of the full system, $\vec{d_j}$ is the dipole operator on the jth atom, and subscripts indicate the atom in question. This dipole moment results in a coupling, which lifts the degeneracy. This is the quantum analogy to the classical interference of the radiated fields introduced above. It can also be seen as an exchange of virtual photons causing the single excitation to "hop" between the two emitters.
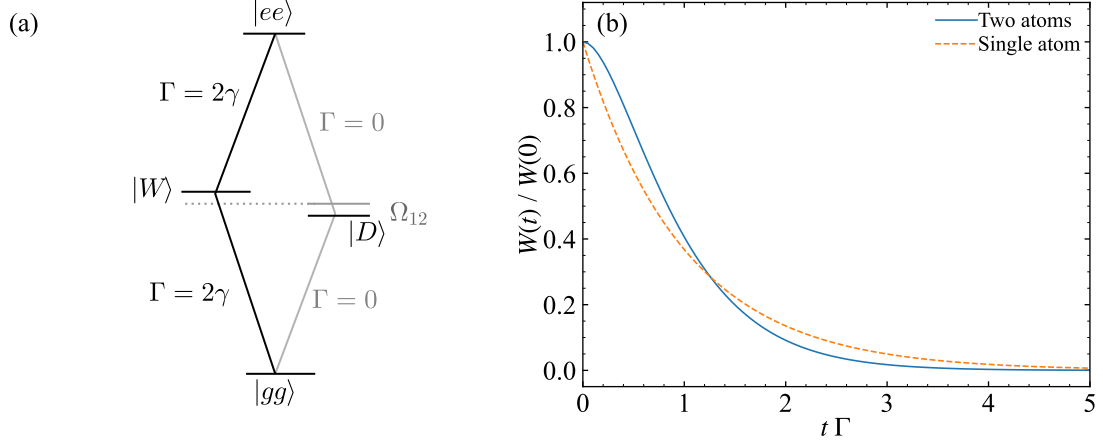
Figure 2.1: The collective states of two atoms. a) Level scheme for two atoms with the collective bright and dark state. b) Emission from two collectively excited atoms starting in $|ee\rangle$ compared to the emission from two independent atoms.

With this interaction it is convenient to describe the two-atom system in a basis of collective superposition-states,

$$|\pm\rangle = \frac{1}{\sqrt{2}}(|ge\rangle \pm |eg\rangle), \tag{2.7}$$

rather than the single-atom states. The same basis can be applied for non-interacting atoms, but does not offer any advantage over the single-atom states.

For the interacting atoms, the interaction causes an energy shift of $|+\rangle$ and $|-\rangle$ relative to the same states for non-interacting atoms with energy Ω_{12} as shown in figure 2.1. This shift, called the collective Lamb shift, is in general present between collective states, and has been measured in many different systems [23, 24, 26, 27, 50, 93]. In this thesis, however, we determine the resonance frequency of interest experimentally based on spectroscopy of the already shifted state, and therefore we will not consider the shift further [94].

When writing the new density-matrix elements in this basis, and assuming that the atoms are close, we arrive [89]

$$\dot{\rho}_{ee,ee} = -2\Gamma\rho_{ee,ee}, \tag{2.8}$$

$$\dot{\rho}_{++} = 2\Gamma\rho_{ee,ee} - 2\Gamma\rho_{++}, \tag{2.9}$$

$$\dot{\rho}_{--} = 0, \tag{2.10}$$

$$\dot{\rho}_{+-} = -\Gamma\rho_{+-}, \tag{2.11}$$

with solutions

$$\rho_{ee,ee} = \rho_{ee,ee}(0)e^{-2\Gamma t}, \tag{2.12}$$

$$\rho_{++} = \left(\rho_{++}(0) + 2\Gamma t\rho_{ee,ee}(0)\right)e^{-2\Gamma t}, \tag{2.13}$$

$$\rho_{--} = \rho_{--}, \tag{2.14}$$

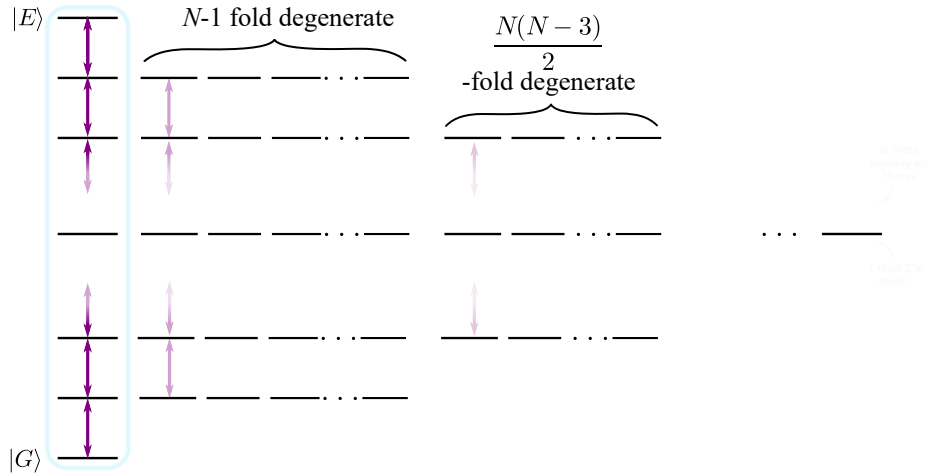$$\rho_{+-} = \rho_{+-}e^{-(\Gamma+2i\Omega_{12})t}. \tag{2.15}$$

7

Figure 2.2: Illustration of the ladder system defined by Dicke. The superradiant 'ladder' is marked with a blue frame. Besides the Dicke superradiant states, the ladder system also contains other states with modified decay rates. The ladder system is characterized by the degeneracy of states [9]. Depending on the step in the ladder, these states may also feature superradiant emission, but not as strong as the states in the Dicke superradiant ladder. The figure is adapted from ref. [9].

These equations highlight that excitation to $|-\rangle$ is trapped, and that coherences between $|+\rangle$ and $|-\rangle$ cannot be introduced solely by decay. In addition, the coherences depend on the energy shift Ω_{12}, which again depends on the exact dipole-dipole interaction between the atoms.

From these equations it is seen that both the doubly excited state and the symmetric state decays with rate 2Γ. The decay of $|ee\rangle$ can be intuitively understood as $|ee\rangle$ being two atoms decaying independently. Clearly, this decay prepares the $|+\rangle$-state, but does not affect the population in $|-\rangle$. The state $|-\rangle$ on the other hand does not decay, and therefore excitations to this state are effectively trapped

The decay rate for a fully inverted system is given by the expectation value of all possible decay channels,

$$W(t) = 2\Gamma(1 + 2\Gamma t)e^{-2\Gamma t}. \tag{2.16}$$

The super- and subradiance of $|+\rangle$ and $|-\rangle$ respectivly hold only for atoms with negligible inter-atomic distance relative to the transition wavelength $r \ll \lambda$. In the case where the atoms are further separated, the decay rates rates are modified depending on the inter-atomic distance. This leads to a small but non-zero decay of the $|-\rangle$-state, which is then said to be subradiant. As the atoms are moved further apart, the decays of $|\pm\rangle$ oscillate, being super- and subradiant in turn [89].

When the atoms are further separated, the relative position of the atoms gives rise to angular dependency of light emission, leading to suppression of emission in some directions and enhancements in others [89]. The first observation of different decay rates as a function of controlled inter-particle distance was made with two trapped ions [14].

2.2 N-atom super- and subradiance

The results found for two two-level atoms can be extended to the situation of N atoms, which we consider in this section. When the N atoms are all close relative to the wavelength of their transition, $r \ll \lambda$, there exist strongly superradiant states, which decay much faster than corresponding radiant states for N independent atoms, depending on the number N [9].

Applying the methodology of the two-atom system analysis, one can rewrite the full N-atom system as a state $|a_1 a_2 \cdots a_N\rangle$ where a_j is the state of the jth atom which is either $|e\rangle$ or $|g\rangle$. This leads to a system with dimension 2^N for which the dipole-coupling terms can again be calculated. The fastest decay happens for a symmetric state with $N/2$ excitations. In this case, the decay is $W(t) \sim N^2$ [9].

Figure 2.2 illustrates the ladder-system introduced by Dicke in analogy to the spin-triplet-singlet system of two spin $1/2$ particles. The symmetric states make up an N-let ladder where decay is superradiant. Other ladders of states with lower degrees of symmetry can also be identified, depending on their degeneracy, and excitations to these states are effectively trapped at the lowest step of their respective ladder.

It follows that a symmetric Dicke state is decoupled from the other states with lower symmetry but same number of excitations, and that such a symmetric state decays only within its 'own ladder' as shown in figure 2.2. The fully excited state itself is not superradiant, but every step below it is, and as the system decays from the fully inverted state, quantum correlations build up between the atoms [12, 79]. As a consequence, the system radiates faster and faster until the number of excitations is $N/2$. Therefore, the signature of a superradiant system with $N \gg 1$, which starts in the fully inverted state, is to first decay normally, but then, after a delay time depending on the number of atoms, emit a strong pulse [79]. The exact pulse height is also determined by N.

The superradiant effects are also present for atoms in an extended ensemble. This case was also considered by Dicke, and has in itself received a lot of attention. A large ensemble of collectively interacting atoms has directional superradiant emission [19, 25, 95, 96]. In the case of an elongated medium, for instance, the emission is primarily along the long axis. Imagining a system of many small dipoles, this can be understood as building more constructive interference along a longer axis [11, 89, 97].

The superradiance is caused by the appearance of correlations between the emitters, carried by exchange of virtual photons. These correlations drop off with distance, and the correlation-length is eventually determined by the uncertainty in the excitation-wavevector. [11].

2.2.1 Single photon superradiance

While the most superradiant state is the half-inverted one, where correlations have built fully up, every step in the ladder of symmetric states decays with enhanced decay rate. The only exception is the fully inverted state, which decays with $N\Gamma$ similar to N independent atoms. In this section we describe the superradiant emission of a single photon from an ensemble of $N \gg 1$ emitters sharing a single excitation. The superradiant emission from this state is called single photon superradiance [43, 98, 99]. First we consider the Dicke state, and then we consider the regime where the N emitters have a spatial distribution such that the excitation contains the phase of the exciting field at each emitter.
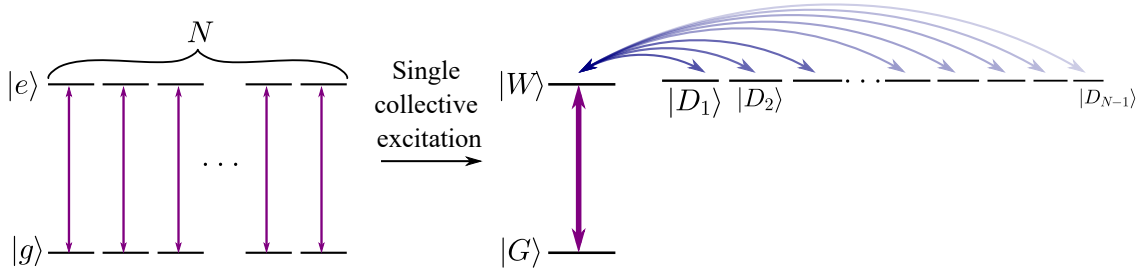
Figure 2.3: N independent atoms sharing a single excitation can be described by a set of N orthogonal collective states. One state, $|W\rangle$, couples to the ground state with enhanced coupling strength to $|G\rangle$ and driving fields. The coupling strength depends on N. The $N-1$ other states are not coupled to $|G\rangle$, but depending on the system in question, they can be coupled to $|W\rangle$, as is the case for the timed Dicke state. This corresponds to the second-lowest step in the ladder shown in figure 2.2.

This single excitation Dicke state is

$$|W\rangle = \frac{1}{\sqrt{N}} \sum_{j=1}^{N} |gg \cdots e_j \cdots g\rangle. \tag{2.17}$$

Considering the coupling between this state and the ground state $|G\rangle = |gg \cdots g\rangle$, we find that

$$\langle G| \vec{D} |W\rangle = \frac{1}{\sqrt{N}} \sum_{j=1}^{N} \langle g| \vec{d} |e\rangle = \sqrt{N} \langle g| \vec{d} |e\rangle. \tag{2.18}$$

Compared to a single atom, the N atoms couple to the collective ground state with a coupling that is enhanced with a factor $\sqrt{N}$ compared to N independent atoms where one atom is excited. This enhanced coupling is also present in the decay. This state thus decays with $N\Gamma$, which is N times faster than a single excited atom.

While the state in equation 2.17 describes the symmetric superposition of a single atom being excited and the rest being in the ground state, an N atom system with a single excitation also has $N-1$ other superpositions with lower degree of symmetry, $|D_n\rangle$. This is illustrated in figure 2.3 These states are orthogonal to each other and orthogonal to the states of equations 2.17, such that

$$\langle W|D_n\rangle = 0, \qquad \langle D_n|D_m\rangle = \delta_{nm}. \tag{2.19}$$

Given the orthogonality of the states, the dark states are also decoupled from the light, and as the two-atom $|-\rangle$-state, the $N-1$ dark states have zero decay-rate. Therefore, excitation to one of these states is trapped.

The enhanced decay from the state described by equation 2.17 is only true for the special case where the atoms are indistinguishable, stationary, and non-interacting. For extended ensembles of atoms, the exact geometry has to be taken into account, and the state given in equation 2.17 may have completely different decay dynamics.

In the case of an extended atomic ensemble it is more realistic to consider a state of a single excitation prepared by an incoming plane wave. This state must take the wave-phase experienced by the different atoms into account [80].

We assume that the excitation is imprinted with an interaction Hamiltonian of N two-level atoms interacting with a field with wave-vector $\vec{k_0}$ given by

$$H_{\text{int},k_0}(t) = \hbar g_0 \sum_{j=1}^{N} \left(e^{i\vec{k_0}\cdot\vec{r_j}} e^{-i(\omega-\omega_0)t} \sigma_j^\dagger a_{k_0} + h.c. \right), \tag{2.20}$$

where g_0 is the coupling strength of the light in the mode k_0 to the single atom, $\vec{r_j}$ describes the position of the jth atom, and $\sigma_j^\dagger$ is the creation operator of an excitation of this atom. a_{k_0} is the photon annihilation operator of a photon in mode $\vec{k_0}$, and ω_0 and ω are the resonance angular frequency of the driven transition and the angular frequency of the driving field respectively. In this equation, we assume a scalar field.

We now consider the time-evolution of a state with all atoms in the ground state under this Hamiltonian. We assume that a single atom couples weakly with the light, and that only a single photon is absorbed. With these assumptions, we arrive at a collectively excited state that is a symmetric superposition of the jth atom being in an excited state and the remaining atoms being in the ground state:

$$|W\rangle = \frac{1}{\sqrt{N}} \sum_{j=1}^{N} e^{i\vec{k}\cdot\vec{r_j}} |g, g, \cdots, e_j, \cdots, g\rangle. \tag{2.21}$$

This state is often referred to as the 'timed Dicke state'. The emission properties of this state were discussed in ref. [80], and the state was first called a timed state in ref. [100]. Here we follow the same steps of ref. [80] to see how the timed Dicke state has enhanced emission into the mode which imprints the excitation.

The state described by 2.21 has the same enhanced decay as the symmetric single-excitation Dicke state of closely spaced atoms described by equation 2.17. Both states also features an enhanced coupling to a resonant field which is a factor $\sqrt{N}$ stronger than N independent atoms. However, the phase factors in equation 2.21 become important when the spontaneous decay is considered. Contrary to the state of equation 2.17, the timed Dicke state contains information about the wave which caused the excitation, and as long as the phases remain coherent this state will radiate back into the mode that created it.

This effect is seen by considering the interaction Hamiltonian from equation 2.20 summed over all modes,

$$H(t) = \sum_{\vec{k}} H_{\text{int},k}(t). \tag{2.22}$$

The resulting time evolution under this Hamiltonian is

$$U_H(t) = \mathcal{T} \exp\left(-\frac{1}{\hbar} \int_0^t dt'\, H(t') \right) = \prod_{j=1}^{N} U_H^{(j)}. \tag{2.23}$$

Here $\mathcal{T}$ is the time ordering operator. $U_H(t)$ can be described by the single-atom evolution where $U_H^{(j)}$ describes the time evolution for one atom.

The single atom evolution can be described by the Weisskopf-Wigner treatment.

$$U_H^{(j)} = \gamma_j^\dagger \sigma_j, \tag{2.24}$$

where σ_j works on the jth atom, and

$$\gamma_j\dagger = \sum_{\vec{k}} \frac{g_{\vec{k}}}{\omega_{\vec{k}} - \omega + \frac{i}{2}\gamma} a_{\vec{k}}^\dagger \tag{2.25}$$

is the radiation operator which creates a photon [80, 91]. γ is the Weisskopf-Wigner spontaneous emission rate.

The time evolution of equation 2.21 can be considered by applying the operator of equation 2.23. In particular we can consider the decay from $|W\rangle$ to $|G\rangle$ as a function of time and assume no driving field: The photonic state is $|0\rangle$.

$$\langle G| U_H |W\rangle |0\rangle = \frac{1}{\sqrt{N}} \sum_{j=1}^{N} e^{i\vec{k_0}\cdot\vec{r_j}} \gamma_j^\dagger |0\rangle = \frac{1}{\sqrt{N}} \sum_{\vec{k}} \frac{g_{\vec{k}}}{\omega_{\vec{k}} - \omega + \frac{i}{2}\gamma} |1_{\vec{k}}\rangle \sum_{j=1}^{N} e^{i(\vec{k_0}-\vec{k})\cdot\vec{r_j}}. \tag{2.26}$$

Assuming that the atomic density is high, the summation over all positions can be replaced by an integral:

$$\sum_{j=1}^{N} e^{i(\vec{k_0}-\vec{k})\cdot\vec{r_j}} \simeq \frac{N}{V}(2\pi)^3 \delta^{(3)}(\vec{k_0} - \vec{k}), \tag{2.27}$$

where V is the volume of the atoms. Combining this with equation 2.21 we arrive at

$$\langle G| U_H |W\rangle |0\rangle \simeq \frac{\sqrt{N}}{V} \sum_{\vec{k}} \frac{g_{\vec{k}}}{\omega_{\vec{k}} - \omega + \frac{i}{2}\gamma} |1_{\vec{k}}\rangle \delta^{(3)}(\vec{k_0} - \vec{k}). \tag{2.28}$$

Equation 2.28 demonstrates that the state in equation 2.21 emits spontaneously only into the same direction as wave which made the excitation in the first place. Note that this result is independent of the geometry of the atomic distribution. The quality of the directionality of timed Dicke state depends on how large N is [101].

In ref. [80] it was suggested to use a heralded single photon-scheme to ensure that an atomic ensemble contains only a single excitation. However, there are other ways of ensuring this. One way is to use some sort of blockade mechanism to truncate the excitation ladder, such that only the first step state of the superradiant ladder can be reached. We will return to this in the next chapter and discuss how such a truncation is possible with the Rydberg blockade mechanism.

The single photon superradiance discussed above is sensitive to any effects disturbing or destroying the correlations between the atoms. Such effects include atomic motion and direct atom-atom interactions [87, 102, 103]. This sensitivity is apparent in the phase factor of equation 2.21. Any effect which causes changes in the phase factors leads to dephasing of the system. We will return to this point in chapter 5.

As the symmetric Dicke state of equation 2.17, the timed Dicke state of equation 2.21 also has $N - 1$ other dark sister-states. However, in the timed case these dark states are not completely decoupled from the bright state. For a random distribution of atoms, the exchange of virtual photons gives rise to coupling between the subradiant and superradiant states. This coupling leads to a transfer of population from the emitting state to the non-emitting states, since the timed Dicke state given by equation 2.21 is not an exact eigenstate of the interaction Hamiltonian [104]. This is illustrated with the couplings in figure 2.3.

This transfer in turn leads to a drop in emission [82, 84]. The severity of this effect depends on the exact system; in most cases the effect gives rise to only minor effects, or washes out
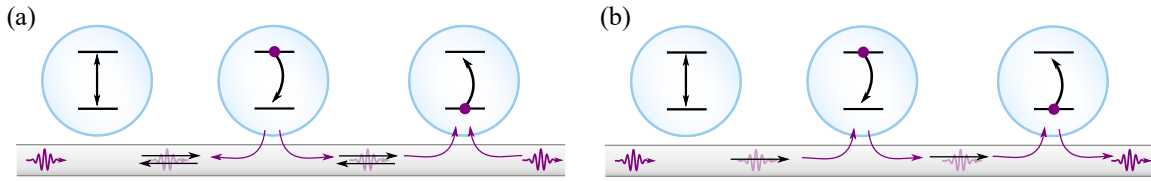
Figure 2.4: Different types of waveguides - determined by the emitter coupling. a) bidirectional waveguide allows the emitters to emit in both directions. b) chiral waveguide allows only emission into one direction.

due to other decoherence mechanisms. Therefore, in the limit $N \gg 1$ the coupling into these states can for most purposes be treated as a single decay term [85, 100]. However, coupling to subradiant states due to the exchange of virtual photons does modify the behavior of the superradiance of equations 2.17 and 2.21 [82, 83].

Until now we have only discussed the decay out of a system of N emitters prepared in a coherent, collective state. When the same system is subject to driving, it features additional, rich dynamics [105]. In case of resonant driving, the N atom collective state features transfer of population out of and back into the bright state [106, 107].

2.2.2 Collective effects in quantum technology

The superradiance and subradiance mechanisms discussed above are not only of interest for fundamental understanding of collective interaction of identical systems. They are also highly relevant in systems for quantum communication, information processing, and simulation, since the mere presence of nearby systems causes changes in the dynamics of a quantum system. The collective interaction and coherence is sensitive to dechoerence from other sources, but as the control over individual quanta for applications in quantum communication and computation, it becomes increasingly important to take these effects into account [108].

In the context of future quantum technology the collective effects can also be utilized to realize strong coupling and directionality of emission as seen in the discussion above, and this may be promising for future applications for instance in combination with ordered atomic geometries where the interaction between light fields and such ordered arrays can be tuned by varying the lattice spacing [32, 34, 38, 109]. Recently, a subradiant mirror consisting of a single layer of optically trapped atoms has been demonstrated [39]. There are corresponding theoretical proposals for using Rydberg atoms in these arrays because of the long-range Rydberg-Rydberg interactions allow long-range interactions between array-atoms [110, 111].

2.3 Waveguide QED

The above discussion shows how systems of many identical emitters behave collectively, and in particular how these collective states can have strong directional emission as it is the case for the timed Dicke state described by equation 2.21. This state of a single excitation shared between many atoms emits its excitation preferably back into the mode which wrote the excitation in the first place. Along these lines it is meaningful to consider systems which already have strong enhancement of coupling to specific system modes such as emitters coupled to cavities or waveguides.

Waveguide-emitter-systems are generally characterized by a waveguide coupling efficiency

defined as the ratio between emitter emission into the waveguide and into other modes. Thus, a single two level atom coupled to a waveguide, which emits into the waveguide with rate κ and out of the waveguide with γ_0 has a waveguide coupling efficiency

$$\beta = \frac{\kappa}{\kappa + \gamma_0}. \tag{2.29}$$

The state of the art is above 0.99 with 10 emitters for superconducting transmon qubits and 0.99 for quantum dots for a single dot in a cavity [112]. These impressive numbers have to be considered relative to the number of emitters, to the operation wavelength, and to the character of the waveguides.

Systems of many individual atoms coupling to nanofibers or solid state waveguides offer a different approach to waveguide-coupled systems: While individual emitters couple weakly, many emitters can be coupled simultaneously [46–48].

The β of equation 2.29 can be compared to the figure of merit in cavity QED,

$$\frac{g_0^2}{\kappa \gamma_0}. \tag{2.30}$$

Here, the coherent coupling inside the resonator, given by g_0 is compared to both parts of photon loss: The loss through the cavity mode, κ, and the loss into any other direction, with γ_0. In the strong coupling regime, g_0 is the dominating time-scale, and fully coherent Rabi oscillations can be observed for even single photons. This regime can never be reached in waveguide QED, since any single photon can only be re-emitted and thus lost.

The term waveguide covers a broad palette of physical structures guiding waves of some sort, and has a well-developed theoretical framework for discussing the coupling between quantum emitters and single propagating field modes. We can identify different types of waveguides, based on the directionality of emission into the waveguides: Bidirectional waveguides which allow emission into both direction, and chiral waveguides which allow only emission in one direction. These two types of waveguides are illustrated in figure 2.4 [42].

In this thesis, there is no actual waveguide in place, but clear parallels can be drawn between the free space systems which will be discussed in this thesis, and waveguide systems, and we will make use of this to discuss the applicability of Rydberg superatoms for quantum applications.

There are different ways of approaching the description of a field in a waveguide interacting with waveguide-coupled emitters. One approach is to integrate out the field and treat the atoms as a spin-system with couplings coming from the field and the directionality of the waveguide. In this section and the following chapter we take this approach [94, 113]. Another approach is to consider the scattering at each atom given by the scattering matrices. This approach allows the considering of non-coherent states [114].

2.3.1 Waveguide mediated emitter-interaction

Now, we consider how a single atom behaves in the case of coupling to a waveguide. In the simplest case, a single, excited atom coupled to an empty waveguide is subject to different decay rate depending on the waveguide type. An atom coupled to a waveguide with $\sqrt{\kappa}$ to a chiral waveguide will decay with rate κ, while it decays with 2κ in the case of a bidirectional waveguide. This can be intuitively understood as the atom having one or two decay channels available.

Note that in this case, the coupling strength given by κ determines the coherent atom evolution if the atom is driven with an input field, but κ also determines the incoherent decay. This is an important point which will be stressed again in section 3.3.

If a single atom is coupled to the waveguide, this also modifies the transmission through the waveguide.

When more than one atom is coupled to the waveguide, the emitted photons from on atom mediate an effective interaction when they are absorbed by another atom. The same holds for the virtual photons which mediate the interaction discussed in sections 2.1 and 2.2.

However, for atoms coupled to a waveguide these virtual photons are not limited to a distance determined by the dipole-dipole interaction and can travel along the waveguide and mediate interaction between even distant atoms [46]. The simple picture discussed here fails, however, when it becomes necessary to take retardation effects into account.

While it is assumed in most works on superradiance that direct atom-atom interaction is negligible, and that atoms are close enough that they can interact via exchange of virtual photons, there is no distance-requirements for a waveguide because all atoms coupled to the waveguide are coupled to the same optical mode, which can transport the information between the atoms. In particular for a bidirectional waveguide the light has to pass every atom before it can escape the waveguide. On the other hand, when the atoms are not randomly distributed along the waveguide, it is possible to tailor the response of the field when the atoms are spaced relative to the wavelength of the field propagating in the waveguide [47, 115].

Collective states in a waveguide

In this section, we paraphrase the detailed calculation of the processes discussed above. More details can be found in [116]. First, we consider two atoms coupled to a waveguide. It is assumed that the two atoms couple to the waveguide with the same coupling strength, and are stationary and located at positions x_1 and x_2.

Again, we assume that the system is not driven. Then, the two-atom system evolution can be described by a master equation of the form

$$
\begin{aligned}
\frac{\partial \rho}{\partial t} = &-i[J_{12}\sigma_1^+\sigma_2^- + J_{21}\sigma_2^+\sigma_1^-, \rho] + \kappa[\mathcal{D}[\sigma_1^-]\rho + \mathcal{D}[\sigma_2^-]\rho] \\
&+ \kappa F_{12}(\sigma_2^-\rho\sigma_1^+ - \frac{1}{2}\{\sigma_1^+\sigma_2^-, \rho\}) + \kappa F_{21}(\sigma_1^-\rho\sigma_2^+ - \frac{1}{2}\{\sigma_2^+\sigma_1^-, \rho\}),
\end{aligned}
\tag{2.31}
$$

where J_{12} describes the coherent coupling between the two atoms caused by exchange of virtual photons. κ is the decay rate of a single atom into the waveguide. As discussed above, κ depends on the type of waveguide.

The Lindblad-like terms $F_{jk}(\sigma_k^-\rho\sigma_j^+ - \{\sigma_j^+\sigma_k^-, \rho\}/2)$ handle the collective decay of the two atoms. F_{jk} is a dimensionless parameter determining how correlated the decay of the two atoms is. If $F_{jk} \neq 0$ there will be different decay rates of the states of the system, and the system will have one state decaying faster than Γ and one state decaying more slowly.

F_{jk} and J_{12} both depend on the type of waveguide. The bi-directional waveguide resembles the free-space situation discussed previously in the case where the two atoms are close together. The parameters are

$$
J_{12} = \kappa \sin(k|x_1 - x_2|), \qquad F_{12} = \cos(k|x_1 - x_2|).
\tag{2.32}
$$

In the situation where $x_1 = x_2$, J_{12} vanishes, such that there is no coherent coupling between the two atoms. This is the situation discussed for two free-space atoms close together aligned along some quantization axis. In this situation, only the correlated decay survives.

In the chiral case, on the other hand, the field can only propagate in one direction, and therefore the two parameters J_{12} and F_{12} cannot be rewritten as trigonometric functions.

$$J_{12} = -i\frac{\kappa}{2}\text{sgn}(x_1 - x_2)e^{ik(x_1-x_2)}, \qquad F_{12} = e^{ik(x_1-x_2)}. \tag{2.33}$$

Equations 2.32 and 2.33 shows that coupling the emitters to a waveguide turns any spatial dependency of the couplings into phase-dependency. Thus J_{12} and F_{12} are functions of the phase difference the light acquires while traveling between the atoms, rather than dropping off over distance.

For the two cases studied here, we can define two different types of states in analogy to the states discussed in the previous section: The Dicke super- and subradiant state, and a bright and a dark state, corresponding to the timed Dicke states prepared by a plane input wave

$$|W\rangle = \frac{1}{\sqrt{2}}\left(\sigma_1^+ + \sigma_2^+ e^{-k_0(x_1-x_2)}\right)|G\rangle, \qquad |D\rangle = \frac{1}{\sqrt{2}}\left(\sigma_2^+ - \sigma_1^+ e^{-k_0(x_1-x_2)}\right)|G\rangle, \tag{2.34}$$

$$|\pm\rangle = \frac{1}{\sqrt{2}}\left(\sigma_1^+ \pm \sigma_2^+ e^{-i\arg(F_{12})}\sigma_2^+\right)|G\rangle. \tag{2.35}$$

Note that the one-dimensionality of the problem is taken into account in the exponential. For certain conditions the two states coincide, but not for in all situations despite the apparent similarity.

For two atoms coupled to a bi-directional waveguide and being close together the states $|W\rangle$ and $|+\rangle$ overlap, and decay with 2Γ while $|-\rangle$ and $|D\rangle$ has decay rate 0. From equations 2.32 we see that the states are completely decoupled, $J_{12} \simeq 0$. The $e^{-2\Gamma t}$ of a system starting in $|W\rangle$ is shown in figure 2.5.

In the other limit, where the atoms are far apart, a system prepared in $|W\rangle$ decays for short times as

$$\rho_{ww}(t) \approx 1 - \frac{3}{2}\kappa t + O(\kappa^2 t^2) \simeq e^{-\frac{3}{2}\kappa t} \tag{2.36}$$

while the population in the dark state changes as

$$\rho_{DD} \simeq \frac{1}{8}(\kappa t)^2 + O(\kappa^3 t^3). \tag{2.37}$$

This modified decay rate can be understood as being caused by coupling to a not-collective decay channel in the backward direction [116]. For long times, the bright state decays much more slowly than the ideal superradiant case due to the population transfer into and out of the dark state.

In the case of a chiral waveguide where propagation is only allowed in one direction, the decay rate of a single atom is given by $\kappa = \gamma$. When two atoms are coupled to this waveguide, $|W\rangle$ and $|+\rangle$ coincide perfectly [116]. Again, $|W\rangle$ decays to $|G\rangle$ with 2κ and $|D\rangle$ does not decay directly to $|G\rangle$ at all.

However, $|W\rangle$ and $|D\rangle$ are still coupled together. This is seen from J_{12} in equation 2.33. This coupling leads to a modified decay behavior. Thus, considering the density matrix elements for the system prepared in W, they are given by

$$\rho_{WW}(t) = \frac{1}{4}e^{-\kappa t}(\kappa t - 2)^2 \tag{2.38}$$

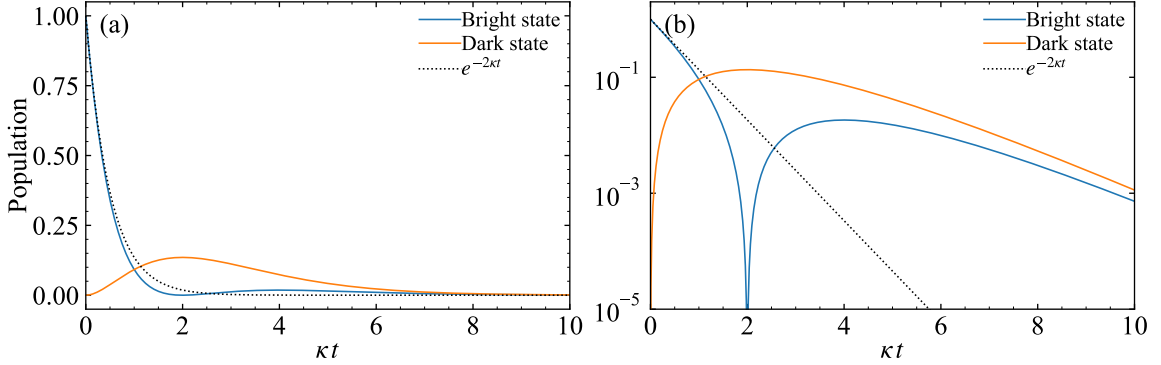$$\rho_{DD}(t) = \frac{1}{4}e^{-\kappa t}(\kappa t)^2. \tag{2.39}$$

Figure 2.5: Population in the bright and dark states of two two-level atoms coupled to a chiral waveguide. The system starts in the bright state. a) shows the populations plotted on a linear scale. b) shows the populations in a semi-logarithmic plot.
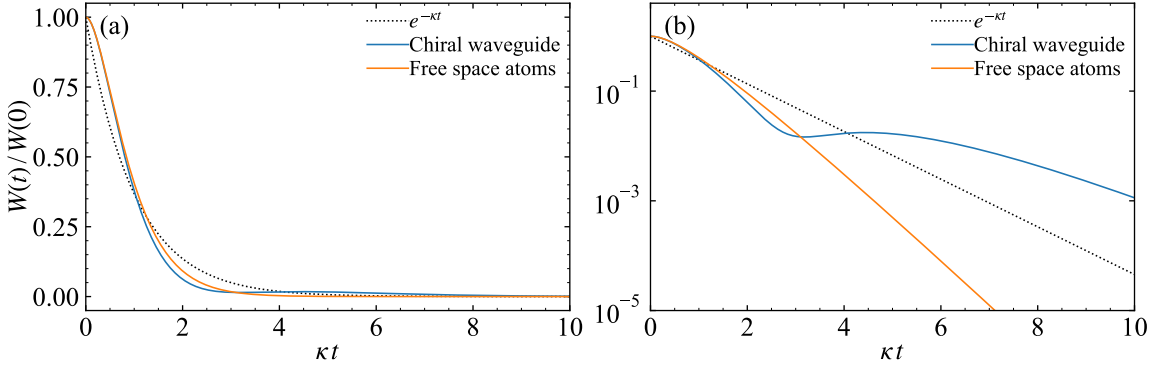

Figure 2.6: Emission from two inverted atoms coupled to a chiral waveguide, compared to emission from two free-space atoms as shown in figure 2.1. a) is shown with a linear scale, and b) is in a semi-logarithmic scale.

For short times, the population in the bright state does indeed decay with rate $\approx e^{-2\kappa t}$. Notably, the population in the bright state drops to zero at $\kappa t = 2$. At this point, all population has been transferred to the dark state, and since the photon emission is proportional to the population in the bright state, it thus also falls off to zero at this point in time. This corresponds to the excited population being stored or hidden in the in the dark state. The populations are illustrated in figure 2.5 and compared to the result for two atoms in free space, each decaying with rate $\Gamma = \kappa$: The population in $|W\rangle$ decays as $e^{-2\kappa t}$.

In the case of a fully inverted system, the intensity goes as [117]

$$I(t) \sim 10e^{-\kappa t} - 6\kappa t e^{-\kappa t} + \kappa^2 t^2 e^{-\kappa t} - 8e^{-2\kappa t} \tag{2.40}$$

This situation is shown in figure 2.6 a) and b).

Figure 2.6 a) shows that the deviation between the emission from two free-space atoms and two atoms coupled to a chiral waveguide are starting in the fully inverted state is initially small, but figure 2.6 b) which shows the same as a) but on a semi-logarithmic scale highlights that the emission behavior is fundamentally different: The chirally coupled atoms are expected to exhibit a dip in emission corresponding to a population transfer from the bright state to

17

the dark state similar to the one seen in the population shown figure 2.5.

However, this dip is challenging to observe since it only occurs at a low photon rate. We will discuss this further in section 3.7

Pausing for a minute and comparing these results to the results discussed for two atoms in free space. The results found for the bidirectional waveguide with closely spaced atoms are similar to the free-space case. However, the results for the chiral waveguide are in stark contrast to the free-space two-atom-case discussed previously.

The directionality of emission, which leads to the mixing between the bright and dark state of the two waveguide-coupled atoms, gives rise to a completely different dynamics, which features a true drop-off of emission, and a revival. This behavior is caused solely by the waveguide limiting the emission to one direction and thereby mediates coupling between the two atoms [117].

2.3.2   Many emitters coupled to a waveguide

The above discussion can be extended to N emitters in a waveguide. In this situation the set of dark states has size $N-1$, and due to the waveguide these states couple to each other and to the prepared bright state. Here we consider the decay of a single collective excitation shared between N waveguide-coupled atoms. Here we in particular follow [116].

In a bidirectional waveguide this decay depends on the exact relative distribution of the atoms. Thus, different limits have to be considered. In the limit where the atoms are spaced closer than one wavelength, the single photon superradiance is recovered. In the other limit, where the atoms are distributed on a much larger scale than the wavelength, but $N \gg 1$ such that the atom distribution is smooth over length-scale set by the wavelength, the phase difference between the atoms becomes important again. In this limit, one finds a similar dynamic as for two atoms coupled to the waveguide, and for N atoms in free space emitting collectively: The coupling to non-emitting states gives rise to a population transfer from the bright state, and thus a drop in emission. This drop is followed by revivals of emission as the population is transferred back into the bright state [82]. The exact position of the minima is given by the atom-distribution. Thus, ordered atomic arrays coupled to waveguides are a platform with many options for tailoring light-matter interaction.

If the waveguide is chiral, the directionality makes the behavior of the collective excitation N emitters prepared in a timed state independent of the exact position of the emitters. The probability of finding the system in the bright state goes as

$$P_W(t) = \frac{1}{N^2} e^{-\kappa t} [L_{N-1}^{(1)}(\kappa t)]^2, \tag{2.41}$$

where $L_{N-1}^{(1)}(x)$ is the associate Laguerre polynomial.

As in the case of two atoms this state decays as $e^{-N\kappa t}$ in the beginning. When longer times are considered, the population in the bright state features a series of revivals corresponding to coupling between the bright state and the dark states of the system. For intermediate times, $1 \ll N\kappa t \ll N^2$, the shared excitation decays with an overall algebraic behavior

$$P_W(t) \sim \frac{1}{(N\kappa t)^{3/2}} \tag{2.42}$$

This decay is eventually bounded by the single-atom decay with κ for times $\kappa t \gg N$.

Interestingly, algebraic decay of the shared excitation found in the chiral waveguide is also found for bidirectional waveguides as $N \to \infty$.

Thus, the collective dynamics seen for free space atoms are also observed for emitters coupled to waveguides, however, the introduction of waveguide coupling allows the emitters to be spatially distributed while still displaying collective behavior [118].

However, this behavior does not require a physical waveguide. Any system featuring directional emission is expected to feature such coupling between bright and dark states. Following this line of thought, the directionally emitting systems discussed in the previous section are interesting candidates for the realization of cascaded quantum systems due to the strong coupling to a driving field and reemission into this same field. In the following chapter, we discuss how to implement such systems with Rydberg states.

Chapter 3

Rydberg superatoms

In the previous chapter, we discussed how ensembles of two level atoms excited with even few photons can exhibit interesting properties in terms of directed emission and drastically modified coupling and decay rates.

These enhanced coupling rates are crucial to realize single photon control but rely on precise state preparation and control of the number of collective excitations. To realize this, we use the Rydberg blockade mechanism, which limits the number of excitations within a given volume and allows the creation of Rydberg superatoms. The superatoms are single collective excitations to a Rydberg state shared between many emitters. This chapter initially provides in section 3.1 a discussion of Rydberg physics for single Rydberg atoms. In section 3.2 the interactions between multiple Rydberg atoms are considered, and we discuss how these interactions can be used to realize the collective states considered in the previous chapter, in particular to realize Rydberg superatoms. In section 3.3 we give a theoretical model of a Rydberg superatom, and we discuss the predictions of this model.

The Rydberg superatoms are realized experimentally with ultracold atoms. The experimental setup for this is described in section 3.4, and in section 3.5 we consider how to create one, two, or three Rydberg superatoms. In section 3.5.2 we review previous results measured with a single Rydberg superatom. Finally, in section 3.7 we analyse the expected behavior of a system with multiple superatoms chained after each other, following the discussion given in chapter 2.

3.1 Rydberg states

Rydberg states are highly excited atomic states, where at least one valence electron has a principal quantum number $n > 10 - 20$ [1]. In the rest of this thesis we work with Rydberg states having a principal quantum number $n > 100$. The large principal quantum number of these Rydberg atoms alter several properties compared to the ground-state atoms, including physical size, binding energy, lifetime, and polarizability. These scalings are summarized in table 3.1.

Figure 3.1 a) shows the energy levels for Rubidium, which is the element used throughout this thesis. The direct transitions to the Rydberg P-states from the ground-state lies in the UV, and are very weak as seen from the $n^{-3/2}$-scaling of the dipole matrix element in table 3.1.

---

[1]The exact designation where Rydberg states begin, and low-lying states end is ambiguous.

Table 3.1: Scaling of important properties of Rydberg atoms with principal quantum number n [119], adapted from ref [120].

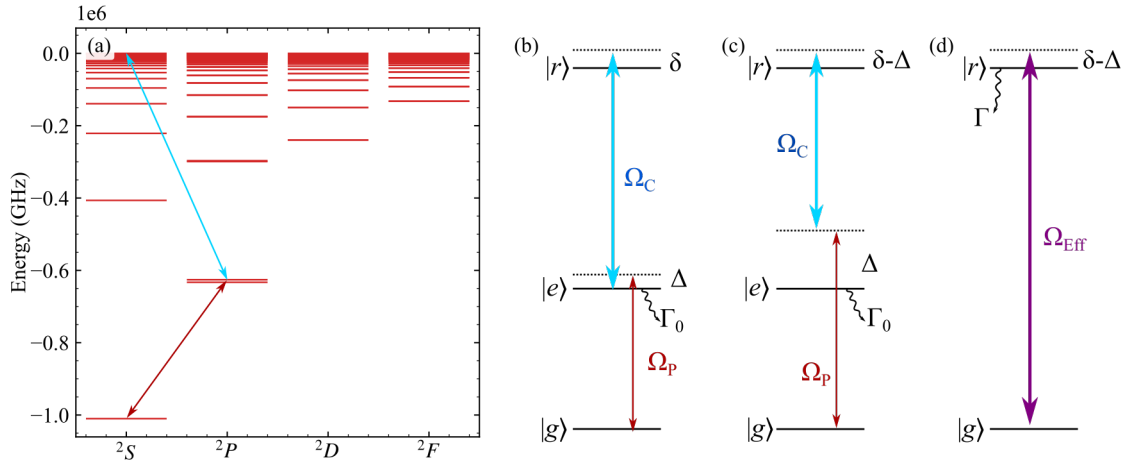| Property	Scaling with n	^{87}Rb, $100s$
Wavefucntion radius	n^2	$13810\,a_0$
Polarizability	n^7	$-6.197\,\mathrm{GHz}/(\mathrm{V/cm})^2$
Binding energy	n^{-2}	$1450\,\mathrm{meV}$
Transition dipole matrix element	$n^{-3/2}$	From $5P$, $0.0047\,\mathrm{e}\,a_0$

Figure 3.1: Rubidium level scheme and abstracted three-level system on and off resonance. a) Rubidium energy levels. The transition $|g\rangle = |5S_{1/2}, J = 1/2\rangle$ to a Rydberg state $|r\rangle = |nS_{1/2}, J = 1/2\rangle$, with $n \approx 100$, via the intermediate state $|e\rangle = |5P_{3/2}, J = 3/2\rangle$. b) and c) show the three level system of a) schematically. The transitions are driven with two fields, the probe field with Rabi frequency Ω_P, and the control field with Rabi frequency Ω_C. The two fields are detuned from single photon resonance with Δ and δ respectively. The intermediate state decays with Γ_0. c) shows how in the limit where $\Delta \gg \Omega_C, \Omega_P$ but $\delta - \Delta \approx 0$ the state $|e\rangle$ can be adiabatically eliminated, yielding a two-level system with effective Rabi frequeny and decay as described in the main text. This resulting two-level system is shown in d).

To increase the coupling strength, and to avoid the UV-regime, we address Rydberg states via a two-photon process as illustrated on figure 3.1 a). In our case we use excitations from $|g\rangle = |5S_{1/2}\rangle$ to a Rydberg state $|r\rangle = |nS_{1/2}\rangle$, $n = 111$, via the intermediate state $|e\rangle = |5P_{3/2}\rangle$. The excitation levels are shown schematically in figure 3.1 b) and c). The transitions are driven by a weak field between $|g\rangle$ and $|e\rangle$, called the probe field, and a strong field between $|e\rangle$ and $|r\rangle$, designated the control field. The two fields are shown in figure 3.1 with Rabi frequencies ω_p and Ω_c respectively. This type of scheme allows us to use a quantized probe field and a strong control field to couple to the Rydberg states, which is possible, because we probe $5S \rightarrow 5P$ and can benefit from this strong transition.

We usually work far-off single photon resonance where it is more likely to drive a two-photon Raman transition than a single-photon transition. We call this regime the Raman regime. In general, adiabatic elimination can be applied for a three-level system as the one sketched in figure 3.1 c) in the limit $\Delta \gg \Omega_c, \Omega_p$, and the dynamics can be described using an effective two-level system [91, 121]. This is illustrated in figure 3.1 d). In this limit, the two
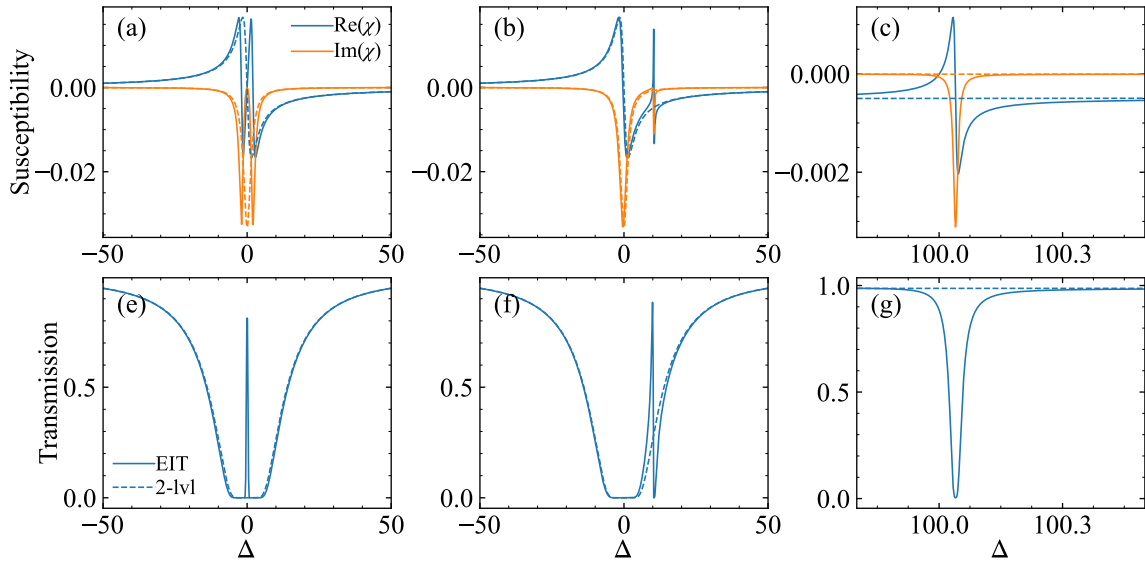
Figure 3.2: Susceptibility (top row) and absorption (bottom row) of a three level system as the ones shown in figure 3.1 with the control field on and off resonance as a function of probe detuning Δ. a) and e) show the situation for $\delta = 0$. b) and f) shows the situation for $\delta = 10$, and c) and g) show the situation for $\Delta = 100$. Note the scale difference between the different plots.

photon process has an effective Rabi frequency of

$$\Omega_{\text{eff}} = \frac{\Omega_p \Omega_c}{2\Delta}, \tag{3.1}$$

and an effective wave vector

$$\vec{k} = \vec{k_p} + \vec{k_c}. \tag{3.2}$$

Assuming the Rydberg lifetime to be long, i.e., assuming that the Rydberg decay rate can be neglected, the effective spontaneous decay rate from the excited state will depend on the intermediate-state decay rate Γ_0 as

$$\Gamma = \Gamma_0 \frac{(\Omega_c^2 + \Omega_p^2)}{4\Delta^2}. \tag{3.3}$$

In this case, the description of multiple two level atoms given in chapter 2 can be applied.

The adiabatic elimination works only in the limit where $\Delta \gg \Omega_C, \Omega_p$. Generally, we can calculate the susceptibility of the 3-level systems of figure 3.1 b) and c) using the density matrix formalism introduced in chapter 2. Besides the Raman regime where the system resembles a normal two-level-system, there is a different regime when the detuning is small as shown in figure 3.1 b).

In this regime with small detuning we find a phenomenon known as electromagnetically induced transparency EIT[2]. EIT can be understood as destructive interference of the absorption paths from the ground state to the two dressed excited states, where the dressing arises from the control field [122].

---

[2]Depending on the relative strength of the fields we may also speak of Autler-Townes-splitting, but this will not be covered further in this thesis.
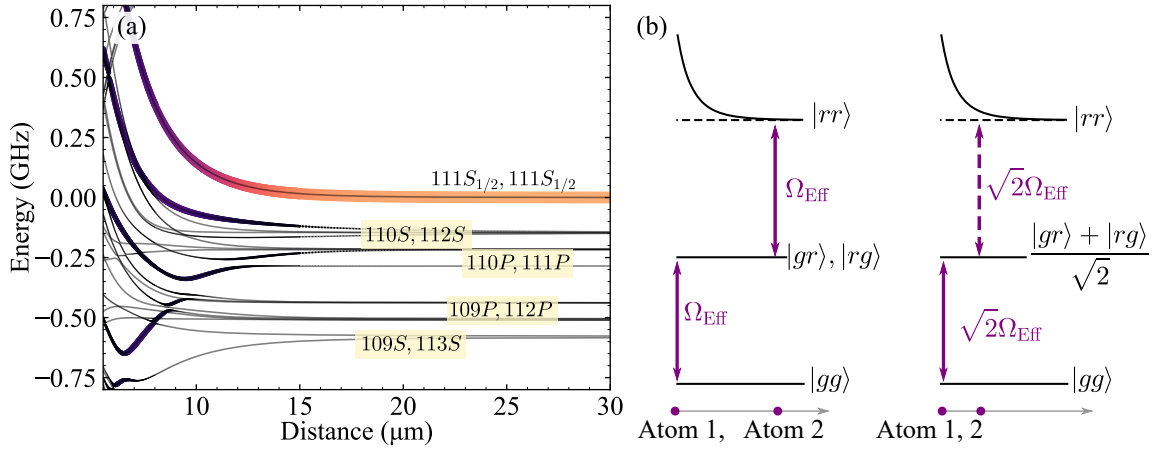
Figure 3.3: Rydberg blockade illustrated. a) Rydberg pairstate energies. The color-code shows the admixture of other pairstates to the $|111S_{1/2}, J = 1/2\rangle |111S_{1/2}, J = 1/2\rangle$-state for short distances. The values are calculated as described in [125]. b) shows a schematic drawing of the same effect. Two atoms far separated can be independently excited to Rydberg states. When the atoms are brought close together, however, the Rydberg interaction shifts the doubly excited state out of resonance with the driving field. The single-excitation state is now shared between the two atoms, which couple with an enhanced coupling strength.

On single photon resonance the probability of finding the system in the intermediate state $|e\rangle$ vanishes in the limit $\Omega_p \ll \Omega_c$. This is seen by considering the linear susceptibility χ of the three-level system of figure 3.1, which describes the field-response in the steady state limit [122].

When the two field frequencies are in resonance with the atomic transitions, the interference appears as full transmission of the probe field. The linear susceptibility χ is plotted in figure 3.2 a), b), and c) as a function of the probe detuning Δ, and the transmission is shown in figure 3.2 d), e), and f) for different values of δ. While the EIT medium is transparent to the probe field, the probe field propagates through the medium with a strongly modified speed. This follows from the sharp slope of the real part of χ plotted in figure 3.2. Thus, EIT has been used to create extremely slow light with $v = 10 \times 10^{-7}$ c [123]. In this limit it makes sense to describe a photon propagating through an EIT medium as a quasi-particle formed by a superposition of the light field and polarization of the medium, also known as slow light polaritons [124]. Other effects can be achieved when an EIT system is tuned by varying the detuning of the two fields off single-photon resonance as shown in figure 3.1 b) to c) leading to the behavior shown in figure 3.2 b) and f).

Moving even further from resonance, we return to the Raman regime as shown on figure 3.1 c). In figure 3.2 c) and g) one sees how the susceptibility feature changes, resemble that of a resonant two-level system except for a sign in the real part of susceptibility.

3.2   Interacting Rydberg atoms

The above discussion of light-matter interaction in Rydberg atoms holds for the case of no interaction between Rydberg states and for the case when there is never more than one excitation. The situation changes drastically when more than one Rydberg atom are present. The

high polarizability of Rydberg atoms shown in table 3.1 makes Rydberg atoms very sensitive to excitations in their vicinity. Consequently, the presence of a Rydberg atom leads to a shift of the Rydberg states for neighboring atoms. An example of this is shown in figure 3.3 a) and schematically in figure 3.3 b).

A range of different types of Rydberg-Rydberg interactions occur, depending on the Rydberg states in question and the distance between the excited atoms. In the remainder of this thesis, our focus will be on Rydberg excitations to single S-states in dilute atomic clouds without any applied electric fields. For this subset of Rydberg excitations the resulting interaction at the relevant distances is of the van der Waals type. This interaction scales with the principal quantum number as n^{11}, and it is proportional to $1/r^6$ as illustrated in figure 3.3. In this regime, one Rydberg excitation shifts the energy levels of the surrounding atoms as illustrated in figure 3.3 a) and b). This shift of energy levels leads to an exponential suppression of more excitations within a volume defined by the Rydberg blockade radius r_b around the existing excitation [126–131]. The Rydberg blockade radius is given by

$$r_b = \sqrt[6]{\frac{C_6}{2\hbar\Omega_{\text{Eff}}}},$$

(3.4)

where Ω_{Eff} is the effective Rabi frequency of equation 3.1. The Rydberg blockade is schematically shown in figure 3.3 b. It is important to notice that the Rydberg blockade may work for a specific state, but that other Rydberg states may not be blockaded at the same distances, they may even be shifted into resonance with a driving field as indicated in figure 3.3.

Further, highly excited Rydberg electron(s) that are far separated from the core can scatter with ground state atoms in the vicinity, leading to the formation of Rydberg molecules [132, 133]. For principal quantum number $n > 80$ the molecule formation leads to a red-shift and a line-broadening of the Rydberg resonance which scales with atomic density [134]. Thus, increased atomic density leads to decoherence in case of large n, even for single Rydberg excitations.

For the experiments discussed in the following, the simple single-state van der Waals blockade is sufficient. However, the Rydberg-Rydberg interaction offers a variety of further tuning options and different scalings through the choice of involved states. A very thorough introduction is given in ref. [125, 135].

The Rydberg-Rydberg interactions also modify the optical response when the driving fields not on single-photon resonance. Here, as elsewhere, the response is highly nonlinear. In the regime shown in figure 3.2 b) the propagating polaritons can experience both dissipative and attractive forces [69]. In the introduction, we discussed Rydbeg atoms for quantum nonlinear optics applications. With additional light fields, the photon-photon interactions can be tuned to yet different regimes, such as repulsive photons [136]. Other schemes have been proposed for realizing even higher control over the propagating polaritons [137, 138].

3.3 Collective Rydberg excitation

The interactions between Rydberg atoms discussed above allow the creation of collective excitations between many emitters as discussed in chapter 2. This is possible in the far-off resonance-regime where each atom in an atomic medium can be treated as a single two-level system. In this regime, an atomic ensemble is subject to the collective effects discussed in chapter 2, in particular an enhancement of coupling. Thus, a collective excitation couples with a factor $\sqrt{N}$ where N is the number of participating atoms compared to N independent atoms [126, 129–131].
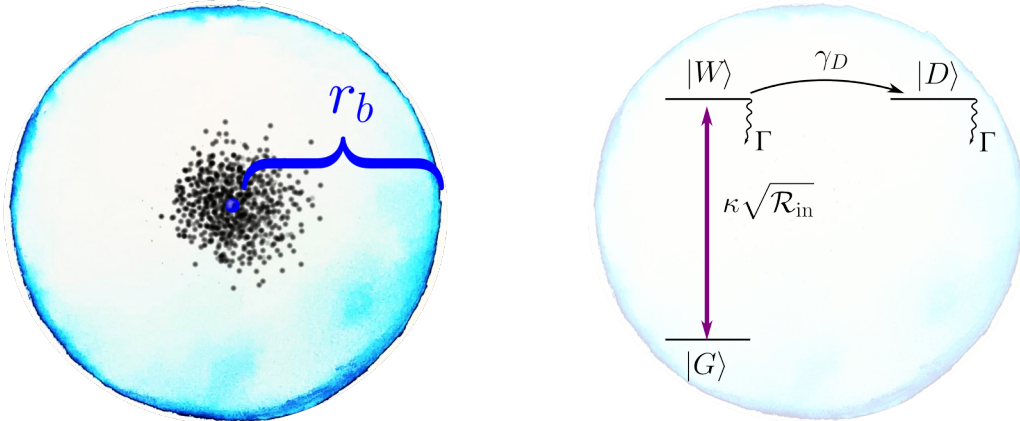
Figure 3.4: Illustration of a Rydberg superatom. N constituent atoms in a small atomic ensemble are only allowed a single shared excitation due to the Rydberg blockade with volume r_b. This allows the abstraction to the model described by equation 3.18.

In the case of excitation to a Rydberg state, the Rydberg blockade directly limits the number of additional excitations within a given volume. To be precise, the Rydberg blockade gives rise to an atom-atom potential. Here, the Hamiltonians discussed in chapter 2 are extended with a potential term related to the interaction energy of a double-excitation:

$$\frac{1}{2}\sum_{j\neq k}^{N} V_{jk}\sigma_j^\dagger\sigma_j\sigma_k^\dagger\sigma_k. \tag{3.5}$$

A similar interaction term also exists for ground state atoms, but here V_{jk} is relevant only at distances r comparable to the ground state atom size, which is much smaller than the interatomic distances considered here. However, for Rydberg atoms the long range atom-atom interaction makes this term relevant for atoms within a large volume, and every atom within in this volume can contribute to N, thus leading to $N \gg 1$.

This atom-atom potential allows to realize strong optical nonlinearities and strong couplings, even to few photon fields. In particular, a well-defined atomic ensemble smaller than the blockaded volume can host a single excitation only, while every atom in the ensemble contributes to the coupling [57, 60, 66].

Such a system is called a Rydberg superatom [59, 61–63]. The term superatom for a collective excitation is regularly used to describe a system of single collective excitations [139, 140], and indicates that in the limit where only a single excitation is allowed in the system, the system can be treated by effectively describing it as a two-level system [57]. This approach allows the treatment of such a small ensemble as a single point-like emitter without considering propagation.

3.3.1 Rydberg superatom model

Based on the discussion in chapter 2, we model the Rydberg superatom system with a collective ground state $|G\rangle$ and a collective bright state $|W\rangle$ as in equation 2.21. This state is coupled to $|G\rangle$ with a $\sqrt{N}$-enhanced coupling compared to the single atom case as shown in equation 2.18. As discussed in chapter 2 the system also features $N-1$ other states which are not

coupled to the light. These dark states can however couple to the bright state via exchange of virtual photons and through dephasing mechanisms. As argued before, the coupling via exchange of virtual photons is expected to lead into a manifold of dark states from which the probability of return to the bright state is very low. Further, various dephasing mechanisms wash out the effect of couplings between the superradiant state and the other states of the system.

Consequently, we abstract the $N-1$ other states to a single state $|D\rangle$. This is illustrated in figure 3.4. This description is also discussed in other works [57, 141, 142].

With this simple two ($|G\rangle$ and $|W\rangle$) plus one ($|D\rangle$) level model, the interaction between the Rydberg superatom and light can now be investigated. As already discussed in the previous chapter 2, the interaction of an electromagnetic field driving a single atom can be described by the Hamiltonian given in figure 2.20 of the form

$$H = H_0 + \hbar\sqrt{\kappa}(E(0,t)\sigma_{GW}^{\dagger} + c.c.). \tag{3.6}$$

To describe the Rydberg superatom it is necessary to consider a system with three states and replace the jump operator σ by the jump operator between the collective ground state and the collective bright state, $\sigma_{GW} = |G\rangle\langle W|$. It is assumed that the superatom is located at $r = 0$. The coupling strength κ is given by

$$\kappa = \frac{g_{\text{col}}^2}{4} = g_0^2 \frac{\Omega_c^2}{\Delta^2} N, \tag{3.7}$$

where g_{col} is the collective coupling strength, and g_0 is the coupling strength of a single atom.

The Hamiltonian H_0 describes the free field,

$$H_0 = \hbar c \int d\vec{k} \, \vec{k} a_{\vec{k}}^{\dagger}(t) a_{\vec{k}}(t) \tag{3.8}$$

where $a_{\vec{k}}$ is the annihilation operator of a photon in the $\vec{k}$th mode. In the case of a coherent input state the unperturbed electric field can be written by

$$E(\vec{r},t) = \frac{\sqrt{c}}{2\pi} \int_{-\infty}^{\infty} d\vec{k} \, e^{i\vec{k}\cdot\vec{r}} a_{\vec{k}}(t). \tag{3.9}$$

From this Hamiltonian the full system behavior can be described given the superatom state by integrating over the free field. Here, the field at a given position and time is described by the given input field and the atomic state.

To see how the interaction with the superatom modifies the electric field we consider the time-evolution of the field operators under eq. 3.6.

$$\partial_t a_{\vec{k}}(t) = -\frac{i}{\hbar}[H, a_{\vec{k}}] = -ic\vec{k}a_{\vec{k}}(t) - i\sqrt{\kappa}c\sigma_{GW}(t), \tag{3.10}$$

which follows from the commutation relation $[a_{\vec{k}}, a_{\vec{k}}^{\dagger}] = 1$. The field-operators and the atomic operators commute as usual.

If the system state is known at some time $t_0 = 0$, the field at some later time t is given by

$$E(\vec{r},t) = \frac{1}{2\pi} \int_{-\infty}^{\infty} d\vec{k} \, e^{-ic\vec{k}t+i\vec{k}\cdot\vec{r}} a_{\vec{k}}(0)$$

$$- i\sqrt{\kappa} \int_0^t dt' \int_{-\infty}^{\infty} d\vec{k} \, e^{-ic\vec{k}(t-t')+i\vec{k}\cdot\vec{r}} \sigma_{GW}(t') \tag{3.11}$$

Here the first term describes the incoming field, which is not changed by the superatom, and the second term describes the superatom-introduced field changes. The first term can be replaced by a non-interacting field term $\bar{E}(t)$. In the case of a coherent field the field amplitude is $\alpha(t) = \langle \bar{E} \rangle$.

The inner integral of the latter term becomes a delta function, and with the outer integral a Heaviside step function, such that the field is completely determined by $\bar{E}$ in space up to the position of the superatom at $r = 0$. Eventually, the field becomes

$$E(\vec{r}, t) = \bar{E}(t) - i\frac{\sqrt{\kappa}}{2}\sigma_{GW}(t). \tag{3.12}$$

Here it has been assumed that the superatom is a point-like object. It then follows that the expectation value of the field is

$$\langle E(\vec{r}, t) \rangle = \alpha(t) - i\frac{\sqrt{\kappa}}{2}\langle \sigma_{GW}(t) \rangle. \tag{3.13}$$

In the experiments discussed in the following sections, the outgoing intensity will be measured. The outgoing intensity is given by

$$\langle E^{\dagger}(\vec{r}, t) E(\vec{r}, t) \rangle = |\alpha(t)|^2 - i\frac{\sqrt{\kappa}}{2}\langle \sigma_{GW}^{\dagger}(t)\sigma_{GW}(t) \rangle$$
$$- i\frac{\sqrt{\kappa}}{2}\left(\alpha^*(t)\langle \sigma_{GW}(t) \rangle + c.c.\right). \tag{3.14}$$

From these equations we can predict the outgoing intensity profile when the atomic state is known, as well as the intensity correlation functions. In section 3.5, we show how the superatom affects the second and third order intensity correlation function $g^{(2)}(t_1, t_2)$ and $g^{(3)}(t_1, t_2)$.

In the above we considered how the field changes depending on the superatom dynamics measured by σ_{GW}. The actual time evolution of the superatom must be known to find the actual values of equation 3.14. This is deduced by considering the time evolution of an arbitrary operator working only on the atomic subsystem [94],

$$\partial_t A(t) = -\frac{i}{\hbar}[H, A(t)]$$
$$= -i\sqrt{\kappa}\left(\bar{E}^*(t)[A(t), \sigma_{GW}] + \bar{E}(t)[A(t), \sigma_{GW}^{\dagger}]\right)$$
$$- \frac{\kappa}{2}\left([A(t), \sigma_{GW}^{\dagger}]\sigma_{GW}(t) + [A(t), \sigma_{GW}]\sigma_{GW}^{\dagger}\right). \tag{3.15}$$

The time-evolution of A can be split in a coherent and an incoherent part. The first term describes the coherent evolution. Considering the definition of $\bar{E}(t)$ this term is readily rewritten to an effective Hamiltonian describing only the superatom state

$$H_{\text{Eff}} = \hbar\sqrt{\kappa}(\alpha^*(t)\sigma_{GW} + \alpha(t)\sigma_{GW}^{\dagger}). \tag{3.16}$$

The second part of equation 3.15 is a dissipative term. Its exact form is found by tracing over the field-part such that only the atomic system is left [57]. This dissipative term accounts for spontaneous decay of the superatom due to the field coupling.

The final master equation for the superatom state becomes

$$\partial_t \rho = -\frac{i}{\hbar}[H_{\text{Eff}}, \rho]\rho + \kappa\mathcal{D}[\sigma_{GW}]\rho. \tag{3.17}$$
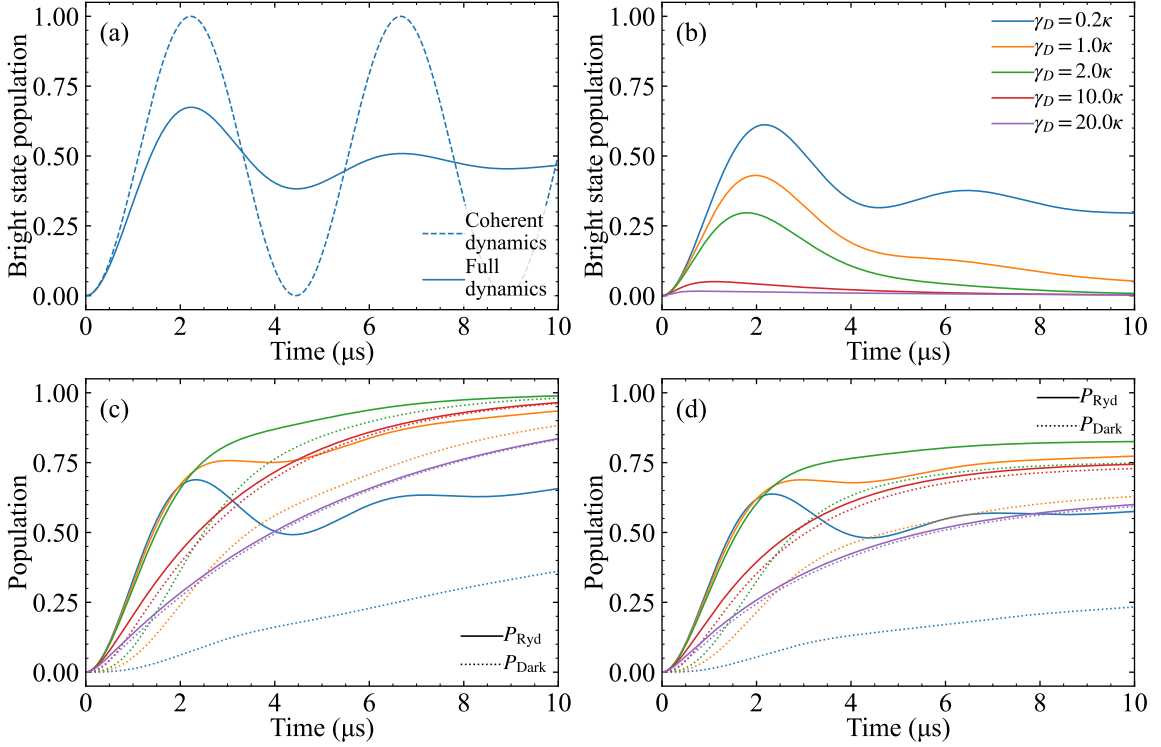
Figure 3.5: Populations calculated for $\kappa = 0.5\,\mu\text{s}^{-1}$ and input field with photon rate $\mathcal{R}_{\text{in}} = 1\,\mu\text{s}^{-1}$ for different values of γ_D and Γ. The top row shows population in the bright state only, while the bottom row shows dark state population and total Rydberg population. a) shows the population in $|W\rangle$ calculated for the pure Hamiltonian compared to the full dynamics described by equation 3.17. b) shows the population in $|W\rangle$ for different values of γ_D. c) shows the total Rydberg population and the population in $|D\rangle$ for the same values of γ_D. Solid lines are the total Rydberg population, dotted lines are the population in $|D\rangle$. d) shows what happens if $\Gamma = 0.11\,\mu\text{s}^{-1} = 0.2\,\kappa$ is introduced.

This equation highlights both how the coupling to the light with strength κ may drive coherent dynamics and also how it causes decoherence through spontaneous emission.

The master equation holds in free space, and it also holds in a waveguide, though the incoherent coupling strength depends on the type of waveguide as discussed in chapter 2. The master equation does not apply to a cavity system, however. Due to the recycling of photons in a cavity system, the incoherent loss rate and the coherent coupling strength are independent.

The above master equation does not take the dark state into account. For a full description we also need to consider that $|W\rangle$ couples to $|D\rangle$ with some dephasing rate γ_D and that the individual single atoms can decay with the Raman decay rate Γ of equation 3.3. In order to establish a master equation that takes the dark state into account, we simply include these other incoherent processes by adding them by hand. The full master equation is

$$\partial_t\rho = -\frac{i}{\hbar}\left[H_0,\rho\right]\rho + (\kappa + \Gamma)\mathcal{D}[\sigma_{GW}]\rho + \gamma_D\mathcal{D}[\sigma_{DW}]\rho + \Gamma\mathcal{D}[\sigma_{GD}]\rho. \tag{3.18}$$

This master equation can be solved numerically, yielding the dynamics of the superatom. The solution of equation 3.18 shows how the collectively excited state behaves under different conditions such as with different driving fields and different parameter-ranges.

The time evolution of the Rydberg superatom described by equation 3.18 can be described with three parameters: κ, Γ, and γ_D. Additionally, the initial state, and the driving field must be known. Some predictions based on the model given by the master equation 3.18 are illustrated in figure 3.5. The figure presents the probability of finding the system in the state in $|W\rangle$, $|D\rangle$, and in any of the two, for different parameter sets.

Figure 3.5 a) first illustrates the point stressed about equation 3.17: Coupling to the light field does not only lead to coherent interaction, but also to decoherence. This is evident when comparing the Rydberg population calculated with the Hamiltonian alone to the Rydberg population calculated with the master equation of 3.17.

Figure 3.5 b) and c) show the idealized case of no Raman decay, while figure 3.5 d) shows the dynamics as the Raman decay is introduced. Here it is clear that for $\gamma_D \gg \kappa$ the total Rydberg population is almost identical to the population in $|D\rangle$. The population does not go to unity, rather, it saturates slowly at some value < 1. This is a clear indication of the effective adiabatic elimination of $|W\rangle$: The probability of even reaching this state from which the population can be transferred to $|D\rangle$ falls off due to the strong decay channel.

The model given in equation 3.6 is not limited to making predictions; it can also be used to fit experimental results. This will be discussed in the following chapters [57, 143].

3.4 Experimental realization of Rydberg superatoms

In the previous section we saw how the Rydberg blockade allows the creation of Rydberg superatoms which couple strongly to a driving field. In this and the following sections we consider how the Rydberg superatoms are realized experimentally.

The experiments discussed in this thesis are all performed with a thermal cloud of ultracold Rb[87] atoms. The atoms are cooled in optical dipole traps that define the geometry of the atomic cloud. We eventually use two different kinds of dipole traps: An elongated ellipsoid trap, and multiple small traps, called dimple traps. These smaller dimple traps are used to prepare the Rydberg superatoms.

Our normal experimental procedure starts by first cooling and trapping ^{87}Rb atoms from a background gas in a magneto-optical trap (MOT). The atoms are transferred into one or more optical dipole traps, where they are cooled to $< 10\,\mu$K. The behavior of the ultracold atoms in these traps are characterized by means of absorption imaging, single photon detection, and ion detection. With single photon detection we measure the transmission of a few-photon probe beam through the ultracold atoms. The transmission can be controlled by a strong control field coupling the atoms to Rydberg states. We can ionize any Rydberg atoms in the samples and use ion detection of the produced Rydberg ions to measure the Rydberg population.

In the following sections, we describe the general experimental setup used in the scope of this thesis for cooling and trapping ^{87}Rb. Detailed discussion of this setup is found in previous works from this group [120, 144, 145], and this section mainly serves as an overview of the most important features of our system.

The experiments are carried out in a vacuum system with a glass cell providing sufficient optical access for the experiments. Inside the glass cell a vacuum-compatible field-control system, discussed in [146], and a multi-channel plate[3] (MCP) for ion detection are mounted. The vacuum system also contains the atom source in the form of rubidium dispensers[4].

---

[3]Hamamatsu F4655-13 MCP
[4]From SAES Getters, RB/NF/4.8/17 FT 10+10

Four sets of magnetic coils are arranged around the glass cell. One set is in anti-Helmholtz-configuration and is used to provide the magnetic fields for magneto-optical trapping of the atoms. The remaining three sets are in Helmholtz-configuration and are used for compensation of stray fields and definition of a quantization axis.

Several different laser beams are used for the cooling and trapping of the atoms. The optics around the vacuum chamber and the beams can coarsely be divided in two groups: Those used for preparation, that is cooling and trapping, and state-preparation of ^{87}Rb, and those used for measurements and system characterization, which comprising absorption imaging and few photon probing. All beams are fiber-coupled at least once before the experiment and a majority of the lasers are locked directly or indirectly to an ultra-stable reference cavity with the exception of the lasers used for Raman sideband cooling and the trapping lasers at 805 nm and 1064 nm which are not frequency stabilized.

3.4.1 Cooling and trapping of rubidium

The first step in our experimental procedure is the trapping of rubidium in a magneto-optical trap (MOT). The MOT is a three-dimensional configuration of beams overlapped at the center of a quadruplole magnetic field [2]. This stage of cooling is necessary because dipole traps are not strong enough to capture atoms directly from the background vapor.

We load the MOT for approximately one second, before the atoms are transferred into a crossed optical dipole trap [147]. The optical dipole trap is kept on while the MOT is loading, already capturing some atoms, but the main transfer happens during compression of the MOT. This compression has three components: Increasing the MOT quadrupole field, decreasing the intensity of the MOT and repumper light, and increasing the red-detuning of the MOT light.

The crossed optical dipole trap is shown in figure 3.6. It has a wavelength of 1064 nm, and the two beams of the cross intersect at an angle of 30° and are focused with $1/e^2$-waist radius of 55 µm.

This crossed dipole trap can be superimposed with additional trapping beams at 805 nm focused onto the crossed trap with waists of 10 µm along the system y-axis direction and 21 µm along the system z-direction in order to form so-called dimple traps. These dimple traps are also shown in figure 3.6 and will be discussed in more detail in section 3.5.

Once the atoms are loaded into the optical traps, multiple steps for cooling and preparation follows before the actual probing of the superatoms takes place. The optically trapped atoms are cooled with steps of combined evaporative cooling and Raman sideband cooling. The Raman sideband cooling is realized by overlapping the optical dipole trap with three Raman beams. One of the beams is retroreflected, and the resulting four beams create a three-dimensional lattice potential and provide Raman coupling. This lattice is only used for the cooling-steps and will not be further considered. The details are discussed in [120, 141]. After the cooling steps we introduce a hold-time in the dipole trap, and optically pump the atoms to the desired state, in this case the $|g\rangle = |5S_{1/2}, F = 2, m_F = 2\rangle$ state.

With these steps we have now prepared an atomic sample in an optical dipole trap. The exact characteristics of this sample are determined through absorption imaging, single photon probing and Rydberg ion measurements: After the optical pumping, the atomic ensemble is briefly released from the dipole trap and is either imaged or probed with a few-photon probe pulse.

After any measurements the atoms are released, and reference measurements without atoms are performed before the MOT phase lasers are turned back on and the cycle starts over. The experiment normally runs with a repetition rate of 0.5 Hz.
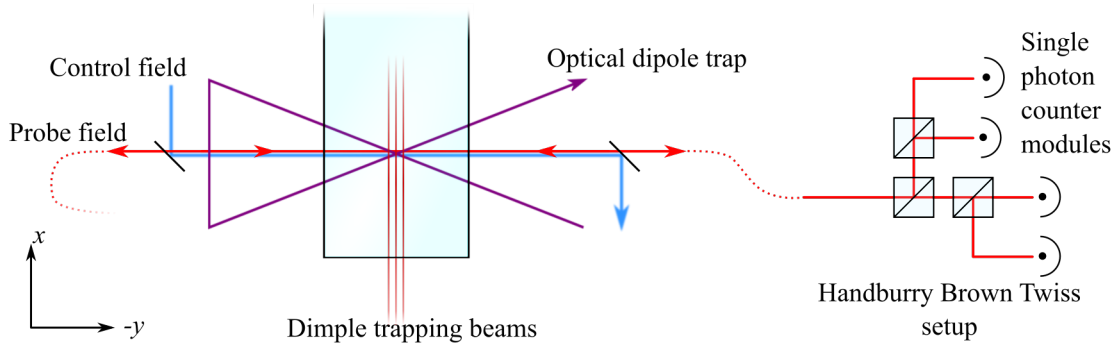
Figure 3.6: Sketch of the trap geometry in the glass cell of the vacuum chamber as seen from the top. The atoms are loaded from a MOT (not shown) into a crossed optical dipole trap forming an ellipsoid trap along the setup y-axis. The crossed dipole trap can be superimposed with the dimple traps along the x-direction. The atoms in the optical dipole traps can be addressed with a probe field. After passing through the atoms, the probe light is fiber-coupled with an optical single mode fiber. It is split onto four SPCM's in a Hanbury Brown and Twiss setup. The probe field is overlapped with a control field, which is used to address transitions to Rydberg states. The setup is implemented with two directions of probe beam such that the atoms can be probed with probe and control beams in either a co- or counterpropagating configuration.

3.4.2 Probing and detection

With the atoms prepared in the optical dipole trap we can start collecting data for characterization and measurements on the system. In particular, we use imaging, single photon detection, and ion detection.

The setup has cameras for absorption imaging installed along two axes, such that the atoms can be imaged in both the y, z- and the x, y-planes. The imaging setups are used regularly, both for alignment purposes, and for characterization of the experiment performance. In particular, we use absorption imaging to determine the number of trapped atoms, the trapping frequencies, and the atom temperature from time of flight measurements. The imaging is done on the $|5S_{1/2}, F = 2, m_F = 2\rangle \rightarrow |5P_{3/2}, F = 3, m_F = 3\rangle$ transition. Under normal circumstances, we trap on the order of 6×10^4 atoms in the dipole trap, and our cooling scheme cools the atoms to $\sim 3\,\mu K$, which we measure through absorption imaging.

Eventually, the imaging is a characterization tool, and our real experimental data consists of single photon traces from probing of the ultracold atoms. The atom ensembles are probed along the long axis of the optical dipole trap as shown in figure 3.6. The probe field is focused to a $1/e^2$-waist of $\sim 6.5\,\mu m$ and the focus is overlapped with the dipole trap. The few photon probing happens on the $|5S_{1/2}, F = 2, m_F = 2\rangle \rightarrow |5P_{3/2}, F = 3, m_F = 3\rangle$-transition. We label these states the ground state $|g\rangle = |5S_{1/2}, F = 2, m_F = 2\rangle$ and $|e\rangle = |5P_{3/2}, F = 3, m_F = 3\rangle$. By measuring the transmission across the resonance of the $|g\rangle \rightarrow |e\rangle$-transition we obtain the optical depth (OD) of the atomic ensemble. This is shown in figure 3.7. For the experiments presented in the following sections we load dipole traps with OD on the order of 40-60 as a starting point for measurements on Rydberg superatoms.

To create Rydberg excitations, we couple the atoms to the Rydberg states with a strong control field of wavelength $\sim 480\,nm$. The control laser field is overlapped with the probe
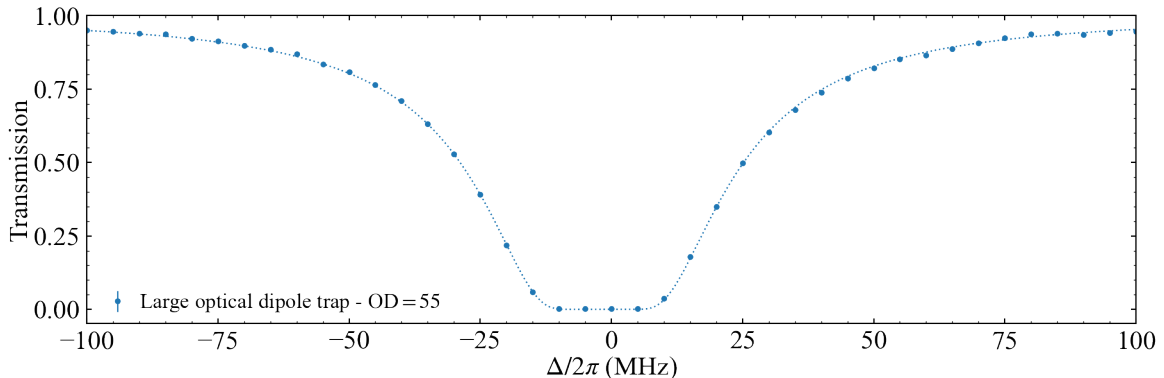
Figure 3.7: Transmission of probe beam through atoms in the crossed optical dipole trap. The points show measured values, error bars are standard error of mean. The dotted line shows the result of fitting an absorption curve to the measured transmission. The fit results yield the optical depth 55.

beam and focused to $\approx 14\,\mu m$ onto the dipole trap. The larger waist ensures that the spatial variation of the control field is comparatively small over the probe beam focus where excitations can take place. The probe and control fields are overlapped with dichroic mirrors and can be set up in either a co- or a counterpropagating configuration depending on the application of interest as illustrated in figure 3.6.

With the probe and the control fields we can drive transitions on and detuned from resonance as shown in figure 3.1 and couple via $|e\rangle$ to a Rydberg state $|r\rangle = |nS_{1/2}, J = 1/2, m_j = 1/2\rangle$. In chapter 4 we use $n = 111$, and in chapter 5 we use $n = 121$.

We turn off the dipole trap for probing, and keep it off for $14\,\mu s$. As the dipole trap turns off, we turn on the control field. The atoms are allowed $2\,\mu s$ before we define the detection window as started. In this time-window of $12\,\mu s$ the probing and detection of single photons take place.

The few-photon probe pulses are coupled back into a single mode fiber and split onto four separate single photon counter modules (SPCM's)[5] in a 'double' Hanbury Brown and Twiss (HBT) setup as illustrated on figure 3.6 [148]. The HBT setup is discussed in [144], and allows detection of photon-photon correlations, for instance stemming from Rydberg atoms [67]. The separation onto four separate counters allow for measurements of higher order photon correlations [149].

Photon- and ion detection events are both counted with a time tagger[6]. After this experiment time-window, the optical dipole trap is turned back on and kept on for $100\,\mu s$, before the probing sequence is repeated. In this $100\,\mu s$-window remaining Rydberg atoms are ionized with a strong electric field pulse. The ions are steered to and detected on a MCP [150]. The exact setup of the electric field control and the ion steering is discussed in [146]. The position of the ions in the atomic sample causes a temporal spread in ion detection time. This in effect comprises a crude form of one-dimensional ion microscopy which yields an estimate for the Rydberg population.

Since we probe with few photon pulses, and only excite single or a few Rydberg atoms in each experiment, the loss of atoms during the probing is very limited. This allows us to

---

[5]Excilitas SPCM-AQRH-23 FC
[6]Swabian Instruments Time Tagger 20

recapture the atoms in the dipole trap after one probing event, and thus we recycle the same atomic medium many times before reloading the dipole trap.

Normally, an experiment cycle consists of 1000 probing sequences. After the probings the atoms are released by turning off the dipole trap for 10 ms. Then the trap is turned back on and kept on emptily, and 1000 reference measurements without atoms in the system are performed.

3.5 Dimple traps for Rydberg superatoms

In the previous section we discussed cooling and trapping of ^{87}Rb in a crossed optical dipole trap. In this section we show how overlapping the crossed dipole trap with smaller optical dipole traps, the dimple traps, which allow us to create Rydberg superatoms. The geometry of this trapping setup is illustrated in figure 3.6. They are realized along the experimental x-axis and are created from beams with wavelength of 805 nm. We use 805 nm which is relatively close to the 780 nm imaging light. This allows us to image through the same optics as we use for the dimple trapping as discussed in ref. [142]. Further, being closer to resonance than 1064 nm allows us to use relatively low power for this trapping.

The separate dimple trapping beams are created from a single beam which is split with an acusto-optical deflector[7] (AOD) [28, 29, 151]. The exact setup is discussed in my master thesis [142]. By applying mixed RF frequencies to the AOD multiple different diffraction orders can be created. The diffraction orders are straightened relative to each other and size-adjusted with a cylindrical telescope. They are focused onto the dipole trap with an objective of effective focal length of $f = 79.5$ mm. We apply RF-frequencies in the range $84 - 120$ MHz generated by an Arduino-controlled direct-digital synthesizer board[8] (DDS). The signals are mixed with each other and amplified before the combined signal is applied to the AOD.

Using a DDS allows us to control both the frequency and the amplitude of the mixed signals individually. Hence, we can control the intensity and the position along the experimental y-axis in the individual diffraction order, and thus the position and depth of the individual traps. The changes can be implemented both between and during the experimental sequence, thus the individual traps can be deepened and moved independently during the experimental cycle. The setup used during the scope of this thesis allows loading of up to three dimple traps with up to on the order of 1×10^4 atoms.

We use this tunability for fine-tuning of the superatom positions and Rydberg resonance as we will see in the following sections. Such a fine-tuning becomes particularly important when multiple superatoms are considered. Thus, we employ tailored loading schemes for one, two or three superatoms. Generally, we are interested in creating as identical superatoms as possible, both in terms of atom-numbers, and thus coupling strength, and resonance frequency, which is determined by the differential light shift from the dimple traps. The optimal AOD parameters for dipole trap overlap, loading procedure, and final dimple intensity are determined through an a combination of imaging, probing, and ion measurements.

3.5.1 Number-specific loading schemes

In order to realize several Rydberg superatoms, we tailor the loading procedure in order to make the superatoms as identical as possible. Realizing a single atomic ensemble in a dimple

---

[7] AA Opto-Electronics model DTSX-400-800
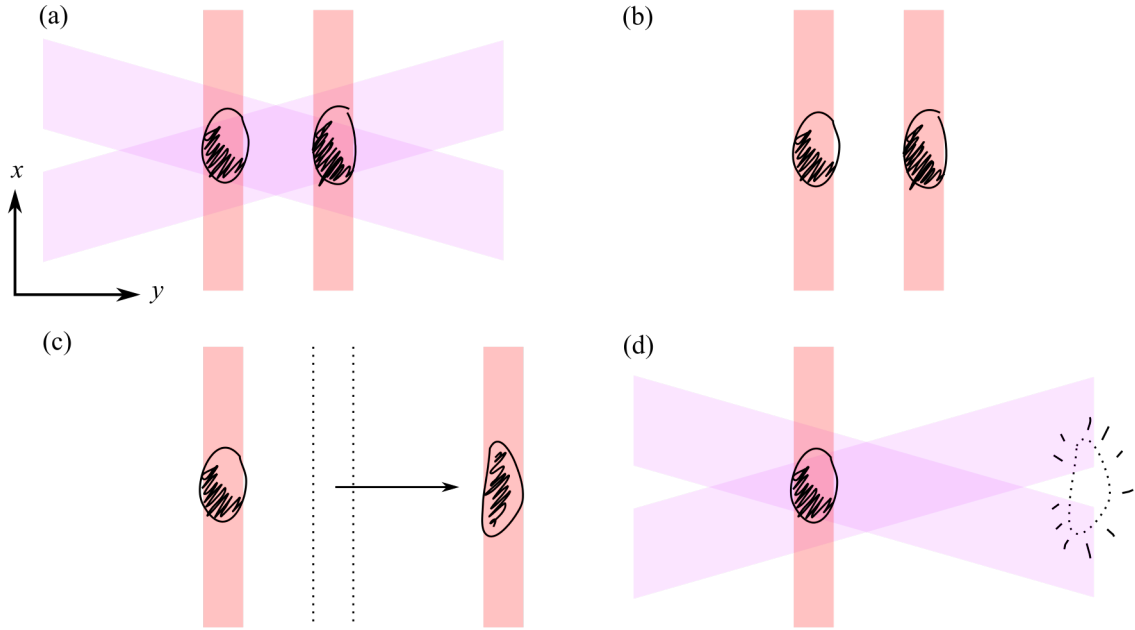[8] AD9959 DDS Evaluation board from Analog Device

Figure 3.8: Procedure for characterizing a single dimple trap when multiple dimple traps are created. The crossed optical dipole trap is shown in purple, and the dimple traps are shown in red. The atoms are shown with black. a) The loading procedure is finished, and two dimple traps have been loaded with atoms. The crossed dipole trap provides confinement along the x-axis. b) The crossed dipole trap is turned off, and the atoms are only held in the dimple traps. c) One dimple trap is moved away from the area of the crossed dipole trap. The ramp-away is done by changing one of the frequency components applied to the AOD. d) The moved dimple trapping beam intensity is turned down, releasing the atoms outside of the trapping region of the crossed dipole trap. The crossed dipole trap is turned back on to provide confinement along the x-direction for the atoms remaining dimple trap.

trap dimple and thus a single superatom is relatively straightforward: Superimposing a single dimple trapping beam with the dipole trap. Realizing more than a single atomic ensemble, however, is limited by the overlap with the dipole trap. For two ensembles, we apply the same procedure as for a single ensemble. We adjust the position of the two beams relative to the crossed optical dipole trap to get roughly the same number of atoms in the two ensembles.

Three ensembles pose another challenge, since one dimple trap has to be positioned in the center of the optical dipole trap where the atomic density is highest, while two other dimples will be loaded from a region with a lower density. Therefore, we employ a scheme of first ramping on the two dimple traps on the sides of the optical dipole trap, and then we we ramp up the intensity in the central dimple beam in a subsequent step. This way we can ensure that the number of atoms loaded into this trap is not much greater than the number of atoms in the two other traps. We adjust the steepness of the different ramps, and the relative time-onset of the ramps to realize similar atom numbers.

We use the option to change the distance between the dimple traps to characterize individual superatoms and to balance the atom numbers between the ensembles. By moving one or more dimple trapping beams away from the cross of the dipole trap and then releasing them, we are able to probe the remaining atoms and thereby any remaining superatoms. The procedure is sketched in figure 3.8.
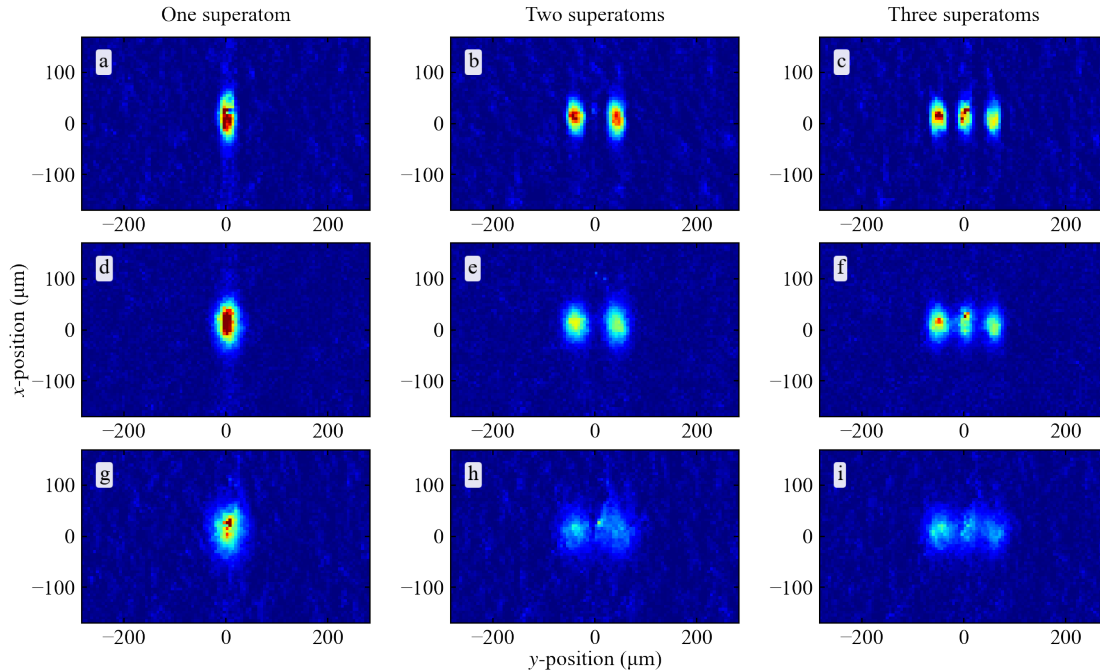
Figure 3.9: Absorption imaging of atoms in dimple traps for different time of flights. a), b), c) are for time of flight 0.12 ms, d), e), f) for 0.32 ms, and g), h), i) are for 0.52 ms.

In practice, the AOD is not perfectly linear in response to intensity, and we expect that the same is true for the mixer. As a consequence, the behavior of a superatom whose 'neighbor' has been released may not exactly reflect the true parameters of this superatom when it is probed with a neighbor. Yet, this ramp-away method is an important tool to verify that the atoms are evenly distributed between the atomic ensembles so we get comparative parameters for coupling to the probe light. Again, this will be discussed in more detail in the following chapters, in particular in chapter 5, where we will see that OD in three ensemble does not equal the sum of the three individual ensembles.

Figure 3.9 shows absorption imaging of one, two, and three atomic ensembles in the dimple traps. The absorption imaging is primarily used to provide a qualitative estimate of whether the dimple trapping beams are well overlapped with the dipole trap and the probe beam. We use the imaging to estimate the temperature through time-of-flight measurements as shown in figure 3.9. Normally, we operate the with atoms at $\approx 10\,\mu K$ In the images on figure 3.9, the relative distance between the dimples is on the order of $80\,\mu m$ for two dimples and on the order of $60\,\mu m$ between three dimples measured from dimple center to dimple center.

3.5.2 Differential AC Stark shift

In the above section we discussed how we use the dimple trapping beam positions to control the atom number in the separate ensembles. We keep the dimple traps turned on during probing, and this gives rise to a differential light shift which may be different for each atomic ensemble. Therefore, we adjust the intensity in the individual trapping beam to give the same light shift in all ensembles. When preparing Rydberg superatoms we ramp the dipole trap off and back on before the optical pumping in order to release atoms trapped outside of the dimple traps. However, by keeping the dimple traps on during probing, the differential light shift experienced
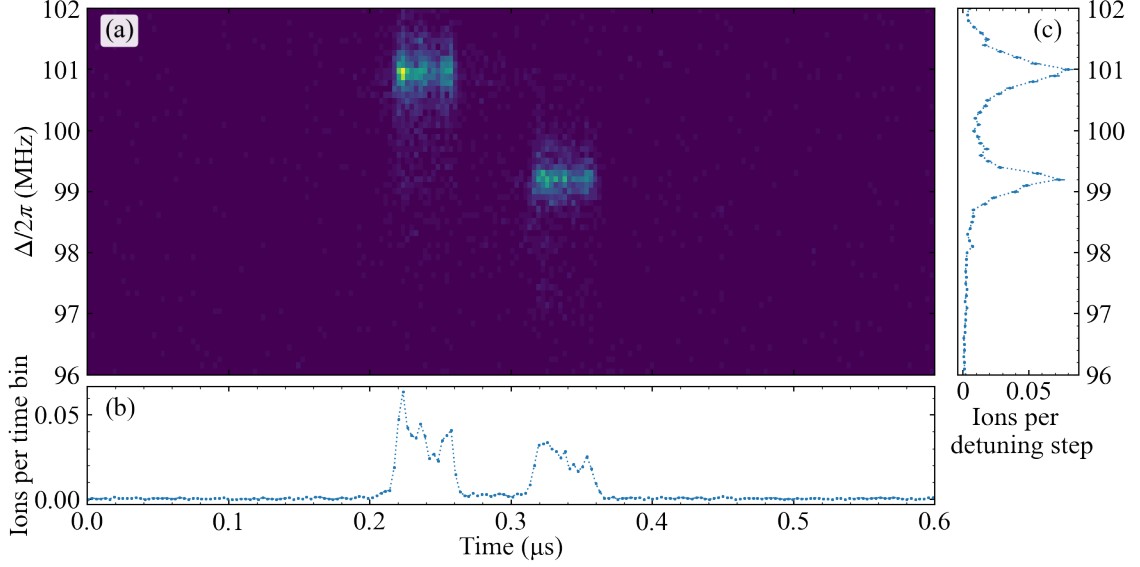
Figure 3.10: Rydberg spectroscopy on atoms in two dimple traps with unbalanced beam intensities. a) shows the number of ions detected during the ion detection window for different detunings. b) shows the sum over ions for all detunings in each ion detection window time-bin of 3.0 ns. c) shows the sum of ions over the full detection window as a function of detuning.

by the atoms in the dimple traps further allows us to distinguish atoms trapped in the dimple traps from untrapped atoms between the dimples.
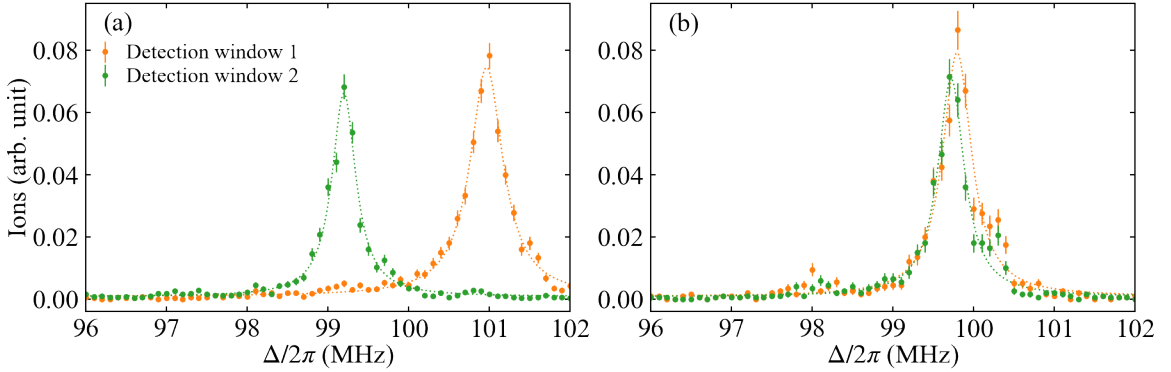

Figure 3.11: Rydberg spectroscopy for balancing the differential AC Stark shift experienced in two different dimple traps. The data has been separated by detection time. Points show measured ions, dotted lines show Lorentzian fits to the ion profiles. a) shows the unbalanced case of figure 3.10. b) shows the case where the intensities in the two beams have been adjusted accordingly. The error bars are standard error of mean.

When we are interested in identical atomic ensembles it is important that all ensembles are subject to the same differential light shift. In order to get the balance between the different trap intensities exactly correct we excite the ensembles via a two-photon process to $|r\rangle$. We then apply a strong electric field to ionize the Rydberg atoms. We detect the ions and use the ion signal to determine the two photon resonance.
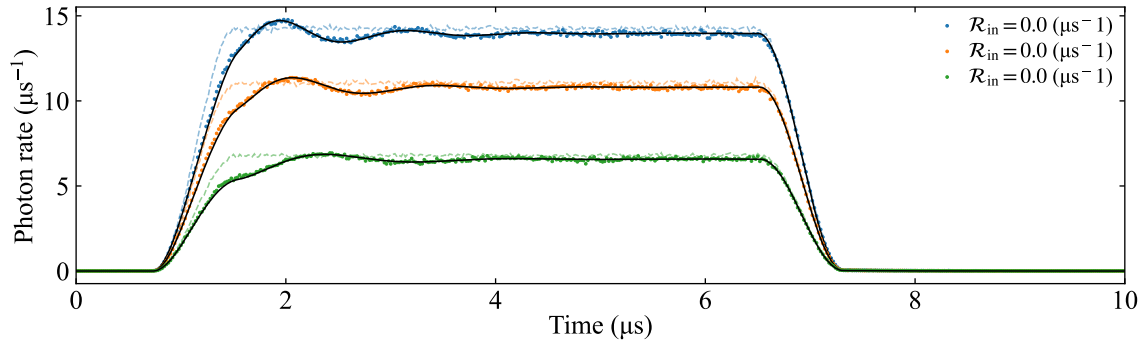
Figure 3.12: Comparison between measured transmission through a single Rydberg superatom for different photon rates. faint data points show the input field measured without atoms in the system, and darker data points show the transmission through the Rydberg superatom. The solid, black lines show the model of equation 3.18 fitted to the experimental data.

Due to the spatial dependency of the ion arrival time it is possible to determine in which atomic ensemble an ion is created. This is illustrated for two dimple traps in figure 3.10. This figure shows the number of detected ions in the detection time-window as a function of probe detuning. Figure 3.10 b) shows the sum of ions for all detunings as a function of time in the detection window. Figure 3.10 c) shows the number of detected ions as a function of detuning with a significant shift between the two photon resonance frequencies of the two ensembles. Figure 3.10 shows a case where the two dimple traps are imbalanced. Based on the measured ion-signals, we adjust the trapping intensities. This is shown in figure 3.11. Figure 3.11 a) shows the detected ions in the two time-windows which can be identified in figure 3.10 b). This is the same signal as is shown in figure 3.10 c). Figure 3.11 b) shows the detected ions after adjustment of the intensity in the two dimples.

It is important to notice that even though the superatoms are created with the same intensity in the dimple trapping beams, they are not necessarily identical in atom number or coupling strength. As discussed in section 3.3 we expect each ensemble to host only a single excitation, independent of the coupling parameters.

Hence, both probing and ion detection are crucial to characterize and adjust the superatom system: Probing gives us information of atom numbers, and the system parameters, and ion detection gives us information about the resonance frequency. Figure 3.12 shows fits of the parameters discussed in section 3.3 for different input photon rates.

3.6   Single Rydberg superatom

As discussed in section 3.3, an ensemble of atoms which can be collectively excited to a Rydberg state via a two-photon process is expected to be coupled to the driving field with a strongly enhanced coupling strength, which allows even reaching of single photon regime.

Thus, when driving a single superatom, w observes single photon Rabi oscillations - imprinted in the light detected on the single photon counter modules. Such a few-photon Rabi oscillation is shown in figure 3.12, which shows the transmitted light through a Rydberg superatom. The input pulse is Tukey-shaped as a compromise between a flat-topped pulse, which gives constant Rabi frequency during the pulse, and a Gaussian shape pulse which is narrow in frequency.
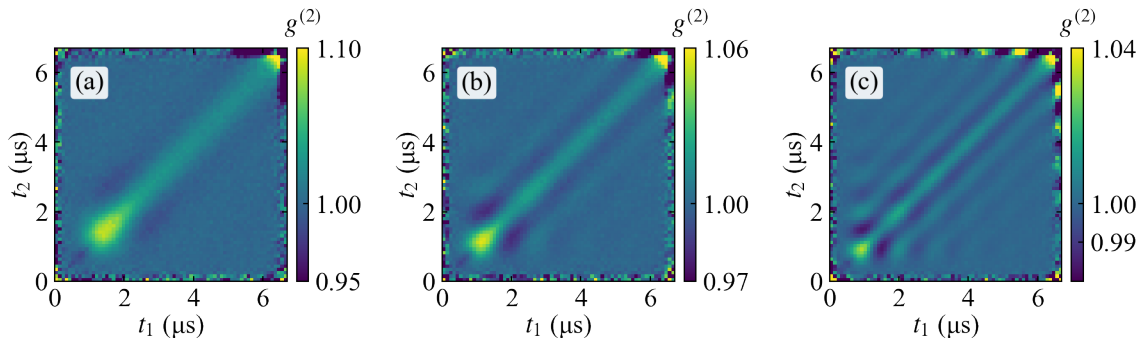
Figure 3.13: Second order intensity correlation function for three different photon rates. The correlation functions show clear stripes of photon bunching and photon anti-bunching. a) is for photon rate $\mathcal{R}_{\mathrm{in}} = 3.4\,\mu\mathrm{s}^{-1}$, b) is for $\mathcal{R}_{\mathrm{in}} = 6.7\,\mu\mathrm{s}^{-1}$, and c) is $\mathcal{R}_{\mathrm{in}} = 15.2\,\mu\mathrm{s}^{-1}$.

A Tukey-pulse starting at time $t = 0$ is defined as

$$\frac{f(t, t_{\mathrm{rise}}, t_{\mathrm{up}})}{\mathcal{R}_{\mathrm{in}}} = \begin{cases} \frac{1}{2}\left\{1 + \cos\left(\pi\left[\frac{t + t_{\mathrm{rise}} + \frac{t_{\mathrm{up}}}{2}}{t_{\mathrm{rise}}} - 1\right]\right)\right\} & \text{if } -t_{\mathrm{rise}} - \frac{t_{\mathrm{up}}}{2} \leq t < -\frac{t_{\mathrm{up}}}{2} \\ 1 & \text{if } -\frac{t_{\mathrm{up}}}{2} \leq t < \frac{t_{\mathrm{up}}}{2} \\ \frac{1}{2}\left\{1 + \cos\left(\pi\frac{t + \frac{t_{\mathrm{up}}}{2}}{t_{\mathrm{rise}}}\right)\right\} & \text{if } \frac{t_{\mathrm{up}}}{2} \leq t < t_{\mathrm{rise}} + \frac{t_{\mathrm{up}}}{2} \\ 0 & \text{otherwise.} \end{cases} \quad (3.19)$$

where t_{rise} is the rise time, defining the duration of the cosine-shaped rise and fall of the pulse, and t_{up} is the up-time giving the duration of the flat top of the pulse.

In figure 3.12 the measured transmission is shown together with model predictions from the superatom model presented in section 3.3. In addition to the intensity modulations we can look for correlations between photons in the outgoing light. This is possible with the HBT-setup shown in figure 3.6. We consider the second order correlation function $g^{(2)}(t_1, t_2)$ which is defined as

$$g^{(2)}(t_1, t_2) = \frac{\langle n_1(t_1) n_2(t_2) \rangle}{\langle n_1(t_1) \rangle \langle n_2(t_2) \rangle}. \quad (3.20)$$

Note that we consider here the two-time correlation function, instead of the common $g^{(2)}(t_2 - t_1)$, which is only applicable in a time-invariant situation. Here, instead, we are observing the transient dynamics of the superatom during a short (compared to the time to reach steady state) driving pulse. A comparison between the theoretically predicted correlation function and the correlation function extracted from measurements is shown in figure 3.13. This figure shows two-photon bunching along the $t_1 = t_2$-diagonal, and then lines of antibunching off the diagonal. This shows how the coherent dynamics reorder the photons within the few-photon pulse.

While figure 3.13 shows correlations between two-photon detection events it is also possible to study higher-order correlations, as demonstrated in [143] where we measured third order correlations between photons were measured. Three-photon correlations have also been observed in cavity systems and other Rydberg systems [149, 152]. Here we briefly revisit the results of ref [143] for completeness. A lengthier discussion is presented in ref. [142].

In this case the third-order correlation function of the intensity at three different times, t_1, t_2, and t_3, was measured. The third order correlation is given by

$$g^{(3)}(t_1, t_2, t_3) = \frac{\langle E^\dagger(t_1)E^\dagger(t_2)E^\dagger(t_3)E(t_3)E(t_2)E(t_1)\rangle}{\langle E^\dagger(t_1)E(t_1)\rangle \langle E^\dagger(t_2)E(t_2)\rangle \langle E^\dagger(t_3)E(t_3)\rangle}. \tag{3.21}$$

which is readily available from the experiment where the few-photon pulses are split onto four different detectors in the HBT setup.

While $g^{(3)}(t_1, t_2, t_3)$ contains information about the correlations between three detectors for time t_1, t_2, and t_3, it is important to note that this also counts two correlated photons and a third 'spectator' photon. Therefore, it is meaningful to introduce the connected third order correlation function, $g^{(3)}_{\mathrm{conn}}(t_1, t_2, t_3)$, where contributions from $g^{(2)}(t_1, t_2)$, $g^{(2)}(t_2, t_3)$, and $g^{(2)}(t_1, t_3)$ are subtracted,

$$g^{(3)}_{\mathrm{conn}}(t_1, t_2, t_3) = g^{(3)}(t_1, t_2, t_3) - \sum_{i<j} g^{(2)}(t_i, t_j) + 2. \tag{3.22}$$

$g^{(3)}_{\mathrm{conn}}(t_1, t_2, t_3) = 0$ in the case of no three-photon correlations. Values above 0 indicates three photon bunching, while values below 0 indicates antibunching.

Since $g^{(3)}_{\mathrm{conn}}(t_1, t_2, t_3)$ depends on three time-coordinates, and thus is a three-dimensional data-structure, it is instructive to do a coordinate transformation into two-dimensional coordinates. Sometimes τ, which is a time-difference coordinate is used together with one time-coordinate [152]. Alternatively, one can use Jacobi coordinates, R, η, and ζ, which describe different planes in the three-dimensional space by the three time-coordinates: $R = (t_1 + t_2 + t_3)/\sqrt{3}$, $\eta = (t_1 - t_2)/\sqrt{2}$, and $\zeta = (t_1 + t_2)/\sqrt{6} - \sqrt{2}\,t_3/\sqrt{3}$.

The experiment discussed in [143] and [142] were done with a single Rydberg superatom of OD approximately 9, and temperature $\sim 9\,\mu$K, and fit-parameters deduced from single photon Rabi oscillations as shown in figure 3.12 $\kappa = 0.55\,\mu\text{s}^{-1}$, $\Gamma = 0.14\,\mu\text{s}^{-1}$, $\gamma_d D = 1.49\,\mu\text{s}^{-1}$.

The measurements were done for three different photon rates, namely $\mathcal{R}_{\mathrm{in}} = 3.4\,\mu\text{s}^{-1}$, $\mathcal{R}_{\mathrm{in}} = 6.7\,\mu\text{s}^{-1}$, and $\mathcal{R}_{\mathrm{in}} = 15.2\,\mu\text{s}^{-1}$. The resulting photon traces were used to calculate the correlation function which was investigated for different values of the Jacobi coordinate R. Figure 3.14 shows $g^{(3)}_{\mathrm{conn}}(t_1, t_2, t_3)$ from the experimental data and from the theory. The data have been averaged over a window of R in order to reduce noise and is plotted from the middle of the pulse.

The signal from pure third-order correlations is small compared to that from two-photon correlations, and the experimentally measured correlation function is small relative to the theoretically predicted correlation function from the model. However, the main features of oscillating three photon bunching and anti-bunching are clearly seen in particular for high photon rates.

It is instructive to compare the performance of the superatom to that of a perfect two-level system. In particular it is possible to consider the interactions with different photon-number-state components of the driving field as discussed in [153]. The analytically calculated $g^{(3)}(t_1, t_2, t_3)$ and $g^{(3)}_{\mathrm{conn}}(t_1, t_2, t_3)$ of such a perfect two-level system are shown in figure 3.15. $g^{(3)}_{\mathrm{conn}}(t_1, t_2, t_3)$ shows the nontrivial contributions from three-photon correlations. The central bunching feature is of particular interest since this is also observed for the superatom, and in the idealized system this stems from a three photon bound state.

These previous results highlight that Rydberg superatoms have the capacity of manipulation and creation of nonclassical photonic states.
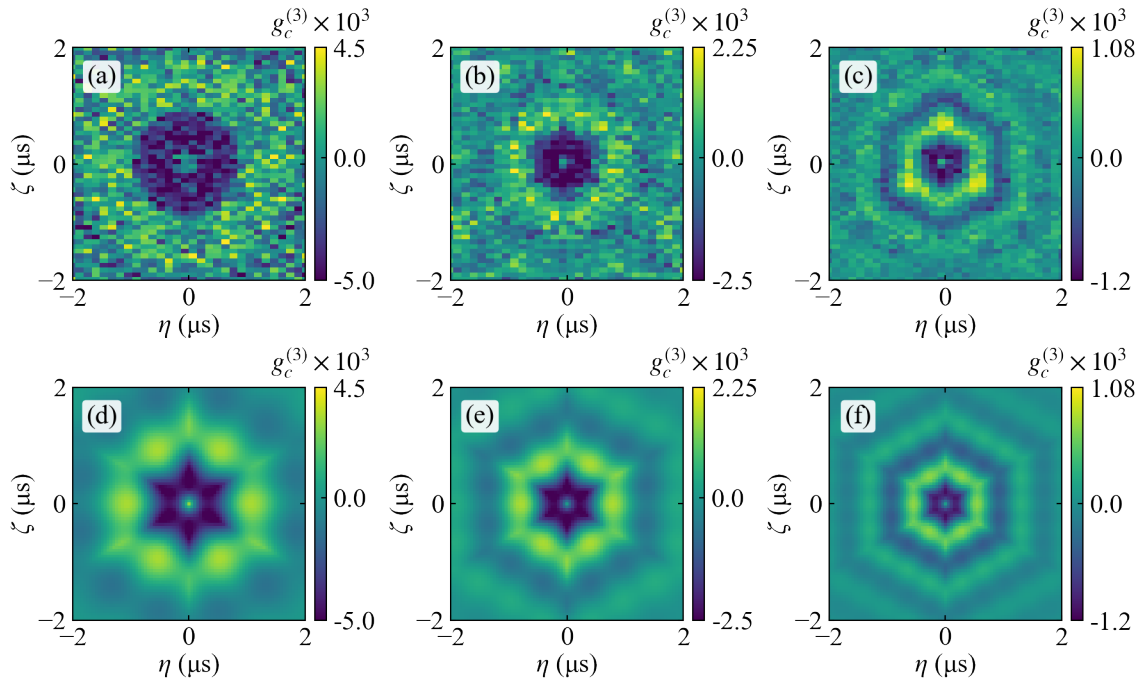
Figure 3.14: Third order connected correlation function measured in a single superatom and compared with model calculations. a), b), and c) show experimental data. d), e), and f) show model predictions. a) and d) shows correlations for $\mathcal{R}_{\text{in}} = 3.4\,\mu\text{s}^{-1}$, b) and e) are for $\mathcal{R}_{\text{in}} = 6.7\,\mu\text{s}^{-1}$, and c) and f) are for $\mathcal{R}_{\text{in}} = 15.2\,\mu\text{s}^{-1}$.

3.6.1 Rydberg superatoms as waveguide QED system

In the previous section we have seen that due to the collective nature of the Rydberg excitation, the superatom couples strongly to a single driving mode, and emits back into this mode with a strong directionality. The strong coupling has allowed observations of absorption and reemission of single photons from back into the driving pulse as shown in figure 3.12, and allowed measurement of second and third order single photon correlation functions.

Hence, a Rydberg superatom strongly resembles an emitter coupled to a chiral waveguide. To put it differently, the superatoms are effectively creating a waveguide due to the collective nature of the Rydberg excitation. A superatom itself couples strongly to 'its' waveguide, whereas the individual constituent atoms are not coupled to this system mode. More complicated dynamics can be imagined if both the superatoms and the constituent atoms are coupled to an actual waveguide [105].

Staying in the picture of the single waveguide prepared by the superatom, the superatom can be characterized by the same set of parameters as any ordinary waveguide. The relative coupling strength was given in equation 2.29:

$$\beta = \frac{\kappa}{\kappa + \Gamma}. \tag{3.23}$$

Unlike the situation for atoms in free space, where the maximum coupling to a single mode equals the linewidth Γ_0 in case of perfect mode matching [154], the coupling of a superatom can be scaled by changing the number of contributing atoms N. With the definition of κ and
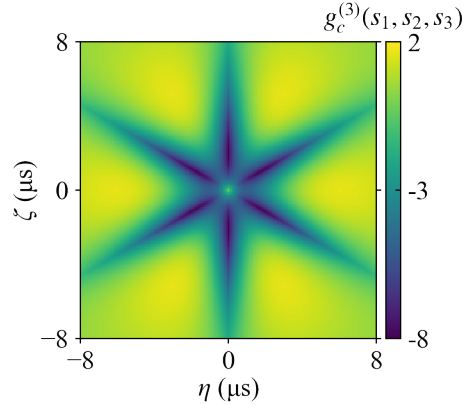
Figure 3.15: Third order connected correlation function calculated for a perfect two-level system.

Γ,

$$\kappa = g_0^2 \frac{\Omega_c^2}{\Delta^2} N \qquad \Gamma = \frac{\Omega_c^2}{4\Delta^2}\Gamma_0, \tag{3.24}$$

it follows that

$$\beta \propto \frac{N}{N + \frac{\Gamma_0}{4g_0^2}}. \tag{3.25}$$

As N increases, the relative coupling is in principle expected to get increasingly stronger, leading to the limit of $\beta \to 1$. However, β considers only the rate of forward emission relative to the total emission rate, but does not take decoherence into account. Another coupling parameter can be defined as

$$\beta_{\mathrm{coherent}} = \frac{\kappa}{\kappa + \Gamma + \gamma_D}, \tag{3.26}$$

where $\beta_{\mathrm{coherent}}$ describes the coherent emission relative to total emission and loss of coherence. At first glance it would appear that increasing N could also improve $\beta_{\mathrm{coherent}}$. However, indefinite increase of N is not an option for the Rydberg system. The N constituent atoms have to be within the blockade volume in order to share the single excitation. As already mentioned higher density also increases the probability of the Rydberg blockade failing and the creation of Rydberg molecules [134]. The Rydberg state can also not be increased indefinitely in order to increase the blockade volume, because it becomes more fragile and susceptible to dephasing due to external fields.

Independently of selection of β or $\beta_{\mathrm{coherent}}$ the strength of an N emitter-system sharing a single, coherent excitation is apparent. The collective nature of such an excitation allows for strong and directional coupling, reaching even single photon level. In the following sections, we will discuss how such a system is realized experimentally.

In the previous section we found parameters for a superatom in free space emitting into a single probe mode on the order of $\kappa = 0.5\,\mu s^{-1}$, $\Gamma = 0.15\,\mu s^{-1}$, and $\gamma_D = 1.4\,\mu s^{-1}$, yielding $\beta \simeq 0.75$, and $\beta_{\mathrm{coherent}} \simeq 0.25$. In [57], the found parameters were $\kappa = 0.428\,\mu s^{-1}$, $\Gamma = 0.069\,\mu s^{-1}$, and $\gamma_D = 1.397\,\mu s^{-1}$. With these parameters, one finds $\beta = 0.86$ and $\beta_{\mathrm{coherent}} \sim 0.23$. Despite the lack of an actual waveguide, these parameters are competetive or even exceeding many other systems. For a recent review of other waveguide-coupled systems, we refer to ref. [112].

3.7 Cascaded Rydberg superatoms

We have shown that a single Rydberg superatom is a model system for manipulating light on single photon level, and we have discussed how the single superatom resembles a waveguide-coupled emitter. The next step to consider is a cascaded system of Rydberg superatoms. This is possible to realize with the dimple trapping geometry shown in figure 3.6, and three superatoms in a chain as shown in figure 3.9. In this section we consider how such a coupling would manifest itself, and consider the relevant parameters for such measurements.

To model the cascaded system of superatoms, we use the same modelling as discussed in section 3.3, but we extend this model to take the interaction between the superatoms into account. This interaction is expected to be mediated by the unidirectional superatom emission as discussed in section 2.3.1. To take the inter-super-atomic interactions into account we describe the full system as a $n^m \times n^m$ density matrix, where n is the number of levels considered in each superatom, and m is the number of superatoms.

The calculations in this section are done with the QuTiP library for Python [155].

3.7.1 Two two-level atoms with decay out of a waveguide

The simplest case, two two-level atoms, is discussed in figure 2.3.1, and leads to a 4×4 density matrix described by the optical Bloch equations of eq. 2.12 to 2.15, and including the coherent coupling of equation 2.31.

In this section we consider two two-level atoms coupled to a chiral waveguide. The emission from two atoms coupled to a chiral waveguide starting in the fully inverted system was already shown in figure 2.6. In this figure we assumed perfect two-level atoms. As discussed in section 3.3 the interaction between a two level atom and a light-field necessarily causes some decoherence with rate κ. In the case of the Rydberg superatom, κ describes the superatom coupling, but the individual atoms also have a finite probability of decaying with rate Γ into 4π. For two-level atoms coupled to a waveguide, this would correspond to decay without emission into the waveguide mode. In order to include Γ, we use the master equation for the Rydberg superatom, equation 3.18 with $\gamma_D = 0$.

Figure 3.16 shows the cost of including decay out of the waveguide. Panels a) and b) show the evolution of a system starting in the fully inverted system $|ee\rangle$. The inclusion of single atom-decay Γ does not alter the dynamics significantly for low values of Γ as in the experiments, but for higher values of Γ the dip caused by the directional coupling washes out. The washing out is caused by the bright state decaying to the ground state before population is transferred to the dark state. The collective dark state is also decaying with rate Γ rather than coupling coherently back into the bright forward state. Therefore, the addition of decay out of the waveguide speeds up the observed emission rate, and leads to a steeper emission slope, corresponding to a smaller fraction of the excitation being emitted into the waveguide system. Panels c) and d) show a system prepared in the waveguide bright state. Here we also see the speed-up of decay as in panels a) and b), yet the emission from the bright state maintains the full drop to zero at $t = 2\kappa$.

So far, we have shown the ideal situation of the two-atom system prepared in a well-known excited state. An experimentally more relevant situation is the system starting in the ground state and being driven to some excited state with a field pulse. This situation is shown in figure 3.17, where we have set $\kappa = 0.5\,\mu\text{s}^{-1}$, and $\Gamma = 0$. We vary the length of the pulse to demonstrate how the two waveguide-coupled atoms are prepared in different collective states depending on the driving. We will return to this point in chapter 4. The increase in emission
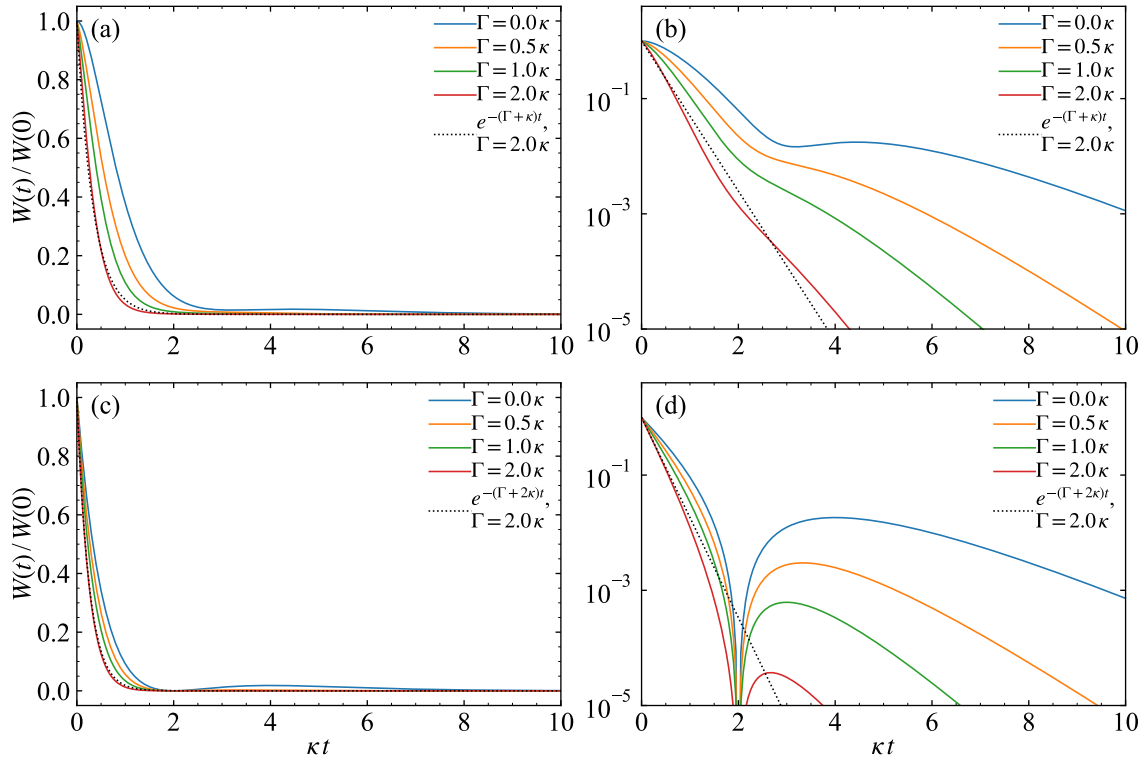
Figure 3.16: Decay of two two-level atoms coupled to a chiral waveguide with coupling strength κ for different value of the decay Γ out of the waveguide and for different initial states. a) and b) show the system starting in the fully inverted state, $|ee\rangle$. a) shows the emission on a linear scale, b) shows a semi-logarithmic scale. c) and d) are calculated for the two two-level atoms starting in the collective bright state $|W\rangle$. c) is plotted with a linear scale, and d) is plotted with a semi-logarithmic scale.

after the end of the pulse is caused by extinguishing the probe field faster than the lifetime of the excited state [95, 96].

The transmission of a probe pulse shown in panels a) and c) does not differ significantly for sets of two atoms coupled and not coupled to a chiral waveguide. However, the emission after the end of the pulse shows different behavior for the two cases. The difference is in particular notable when the emission is shown in a logarithmic scale as on panels b) and d). The emission after the end of the pulse features a dip in emission, similar to what was seen in figure 3.16. As discussed already in section 2.3.1, a system of two atoms coupled to a chiral waveguide is expected to feature a shelving of excited population into the dark state. Panels b) and c) shows how the depth and steepness of the dip depend on the driving pulse. This is caused by loss of coherence between the bright state and the dark state due to stimulated emission with rate κ.

3.7.2 Two-plus-one level superatom

In the previous section we considered what happens when two perfect two-level atoms are coupled to a waveguide and are allowed to decay with Γ out of the waveguide. In order to introduce waveguide-coupled Rydberg superatoms, the next step is the consideration of decay
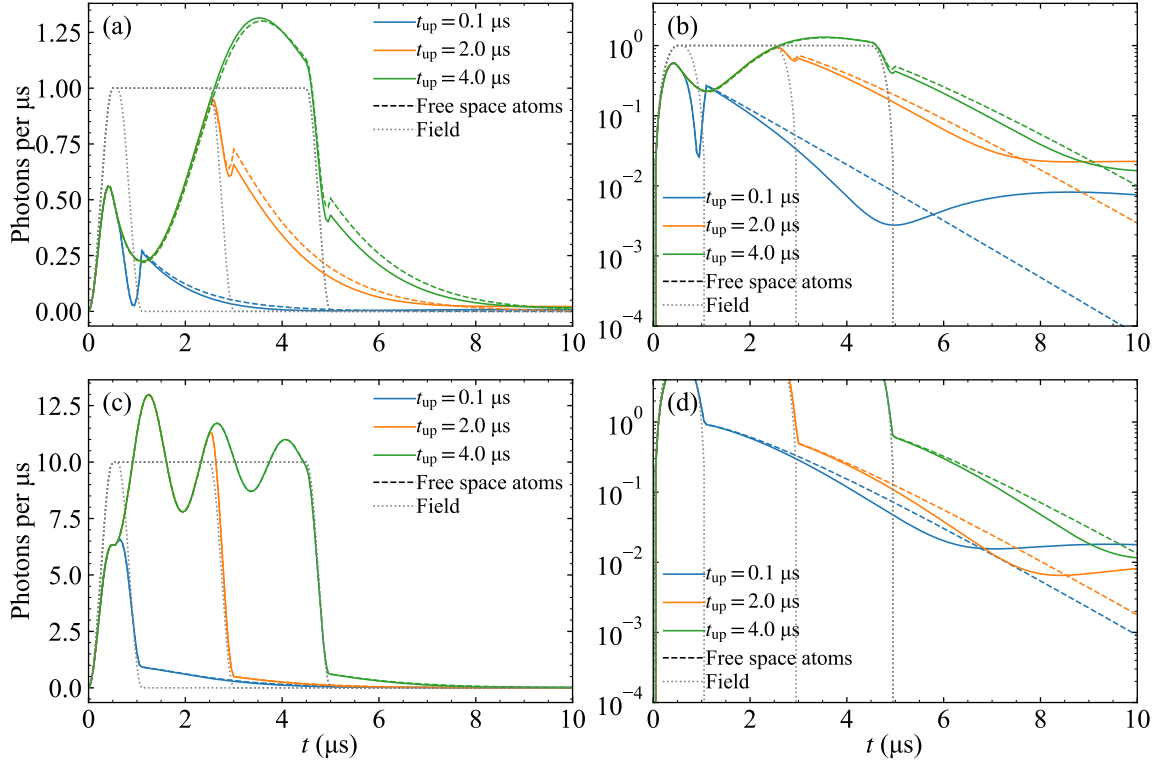
Figure 3.17: Transmission through and emission from two atoms coupled to a chiral waveguide driven with different fields. The atoms both start in the ground state. The atoms are coupled with $\kappa = 0.5\,\mu s^{-1}$ to the waveguide. The dotted line shows the driving field, and the colors show the atom response for different pulse lengths. The dashed lines show the response from two atoms in free space. a) and b) show the outgoing field from the system when it is driven with photon rate $\mathcal{R}_{in} = 1\,\mu s^{-1}$ plotted on a linear and a semi-logarithmic scale respectively. c) and d) show the outgoing field from the system when it is driven with photon rate $\mathcal{R}_{in} = 10\,\mu s^{-1}$ plotted on a linear and a semi-logarithmic scale respectively.
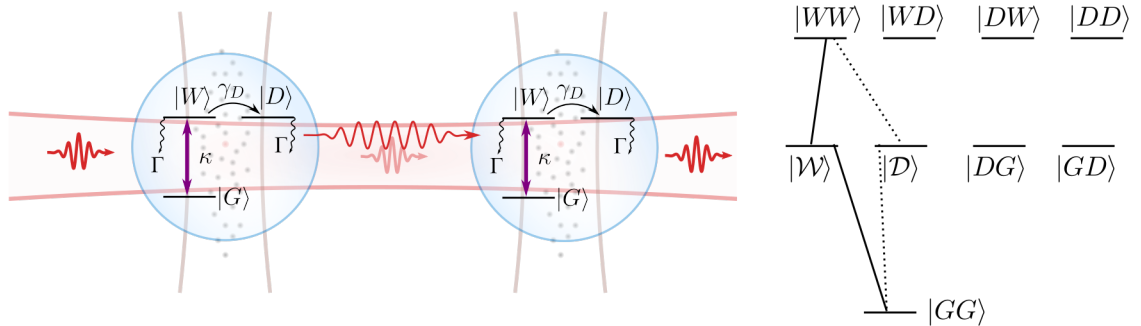

Figure 3.18: Sketch of the level scheme for two superatoms coupled to a chiral wavguide. In the level scheme we highlight the levels present for two two-level systems.
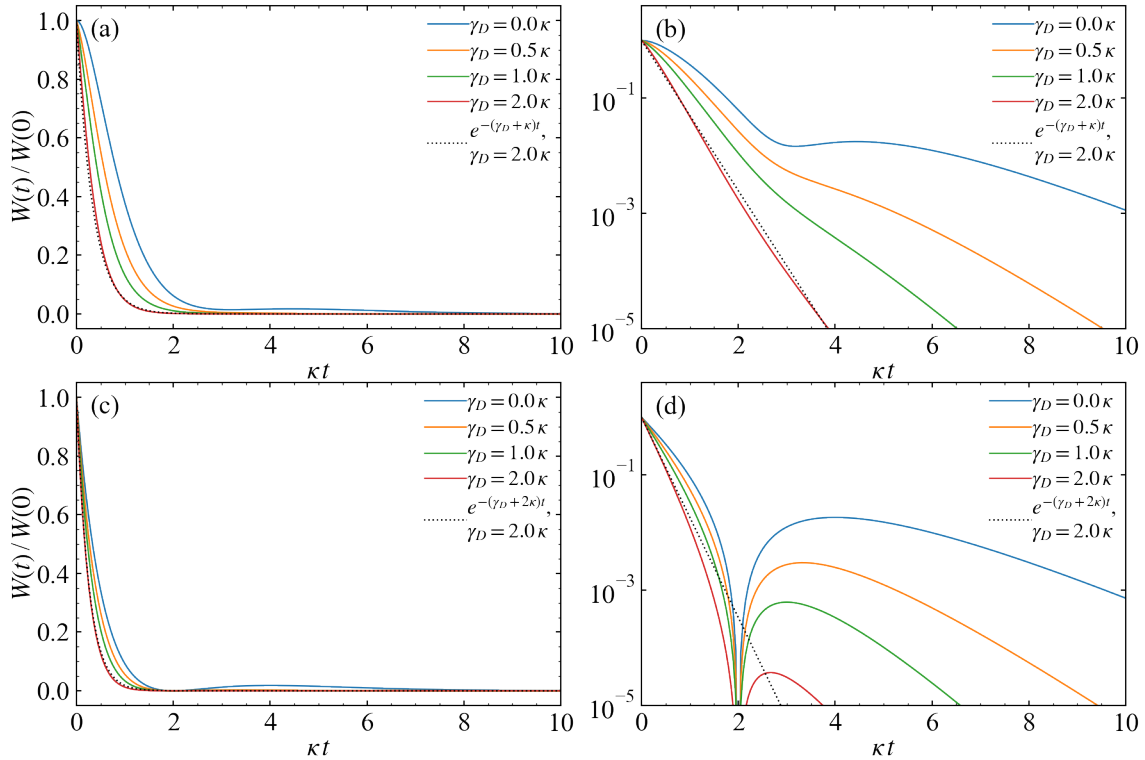
45

Figure 3.19: Decay of two superatoms for different dephasing rates γ_D. The system starts in the fully inverted state in a) and b), and in the collective bright state $|W\rangle$ in c) and d). a) and c) show the emission on a linear scale, b) and d) are in a semi-logarithmic scale.

to an internal dark state in each superatom. To describe two two-plus-one-level superatoms, we consider a 9×9 density matrix. This system is sketched in figure 3.18. The level scheme shows the nine different levels: A ground state with both superatoms unexcited $|GG\rangle$, four levels with one excitations, two of them with one superatom in the superatom bright state and the other in the ground state, $|GW\rangle, |WG\rangle$, and two others with one superatom in the superatom dark state and the other superatom in the ground state $|GD\rangle, |DG\rangle$. Finally, four levels with both superatoms excited: Both in the superatom bright state, $|WW\rangle$, both in the superatom dark state, $|DD\rangle$, and two states with one superatom in the bright state and one in the dark state, $|WD\rangle, |DW\rangle$.

Here, it is important to consider the language used: We have so far used the bright state $|W\rangle$ for any collective bright state, independently of whether it was the bright state of N superatom-constituent atoms or two waveguide-coupled atoms. Therefore, we introduce the waveguide bright (dark) state $|\mathcal{W}\rangle$ ($|\mathcal{D}\rangle$) corresponding to the symmetric (antisymmetric) state of one superatom in the superatom bright state and one in the ground state:

$$|\mathcal{W}\rangle = \frac{|WG\rangle + |GW\rangle}{\sqrt{2}}, \qquad |\mathcal{D}\rangle = \frac{|WG\rangle - |GW\rangle}{\sqrt{2}}. \qquad (3.27)$$

It is not necessary to consider any collective states in the waveguide containing the superatom dark states. A superatom dephased into $|D\rangle$ is effectively invisible to the waveguide.

Introducing a dark state to each atom does not change the emission out of a two-superatom system prepared in the $|\mathcal{W}\rangle$-state. Thus, the decay out of $|\mathcal{W}\rangle$ which is shown in figure 3.19
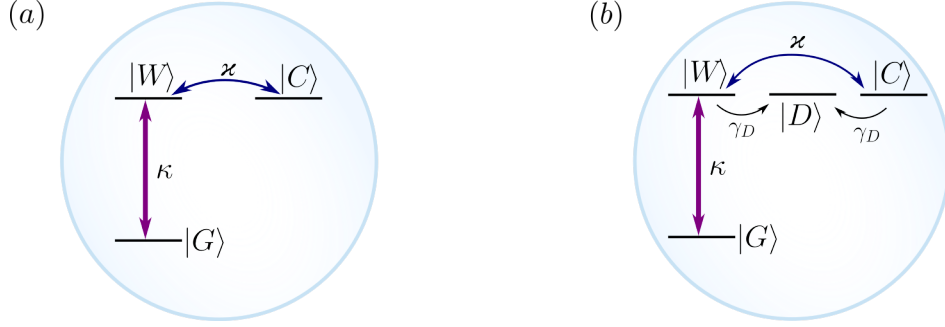
Figure 3.20: Single superatom model with modification. a) The model is modified to include a coherent coupling between the dark states and the bright state with coupling strength $\varkappa$ rather than the irreversible dephasing with rate γ_D. b) Splitting the dark state into coherently coupled dark states and dark states with irreversible dephasing with rate γ_D.

panels c) and d) is the same as what is shown in figure 3.16 panels c) and d), showing that the emission from the state $|\text{W}\rangle$ is affected in the same way by decay with Γ and γ_D.

In the case of the system starting in the fully inverted system, however, γ_D and Γ do not lead to the same emission. This is shown in figure 3.19 a) and b) and should be compared to figure 3.16 panels a) and b). The decay is still sped-up, but flatter. This can be understood as the doubly-excited state being able to decay to both $|\mathcal{W}\rangle$ but also to the other states with two excitations: $|WD\rangle, |DW\rangle$, and $|DD\rangle$. These other states are shown in figure 3.18.

Yet, both of these decay mechanisms cause a washing-out of the inter-superatomic coupling, since they lead to a loss of coherence between the superatoms.

3.7.3 Emitters with internal couplings

In the figures shown above, it is clear that the directional coupling between emitters gives rise to a shelving of excitations in the waveguide dark state $|\mathcal{D}\rangle$. This discussion of two coupled emitters and their dynamics between dark and bright pair states should also apply to N atoms inside one ensemble as discussed in section 2.2. In the Rydberg superatoms the individual atoms are not coupled to a waveguide, but we still expect a dipole-dipole coupling. As a consequence we expect a certain degree of coupling between a bright state and the single system-dark states.

We include such a coupling by extending the superatom-model with a dark state $|C\rangle$ coherently coupled to $|W\rangle$ with coupling-strength $\varkappa$. We revisit this approach again in chapter 4. This is illustrated in figure 3.20 a). The behavior of a system with internal coherent dynamics will be discussed in greater detail in chapter 4.

In figure 3.21, we show the emission from a system of two superatoms without coupling to a chiral waveguide for different values of the coherent coupling strength $\varkappa$. We compare this to a system with chiral coupling with $\varkappa = 0$. Indeed, a system with internal dynamics gives rise to dynamics effects similar as the chiral waveguide-coupling. Panels a) and b) show the system starting in the collective bright state, and it is apparent that a perfect system with coherent coupling always features a full drop of emission when initialized in the bright state. This highlights how the coherently coupled system resembles two idealized waveguide-coupled two-level atoms. In particular in panel b) it is seen how $\varkappa = \kappa/2$ (we plot $\varkappa = 0.51\,\kappa$ for visual clarity) has perfect overlap with the curve for two two-level atoms coupled to a chiral waveguide. The overlap for $\varkappa = \kappa/2$ can be understood from equation 2.33 where $J_{12} \propto \kappa/2$.
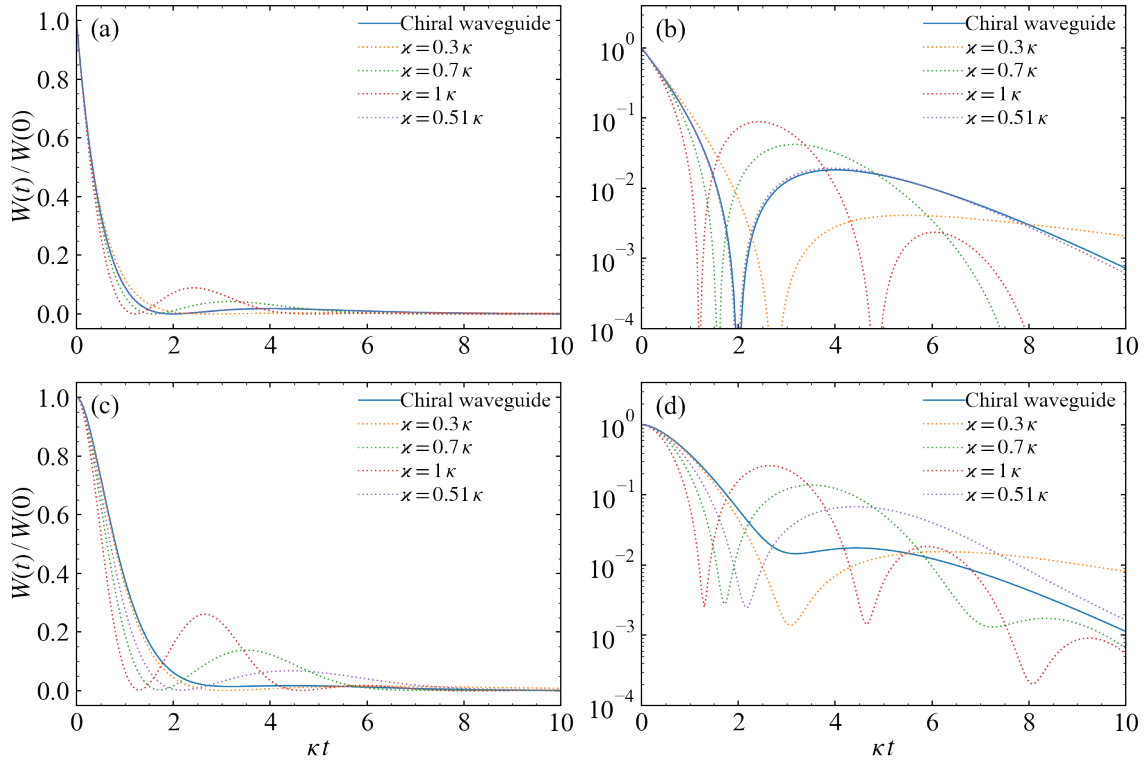
Figure 3.21: Emission from a system of two superatoms in free space with internal coherent coupling compared to two two-level atoms coupled to a chiral waveguide. Both systems emit only into the waveguide mode, $\gamma_D, \Gamma = 0$. a) and b) shows the systems starting in the collective bright state $|\mathcal{W}\rangle$ on a linear and a logarithmic scale respectively. c) and d) shows the systems starting in the doubly excited system $|WW\rangle$.

In equations 4.1 and 4.2 the $\varkappa$-term has exactly the same effect as J_{12} in equation 2.31.

Panels c) and d) show the corresponding situation for the two systems starting in the fully inverted state. In this case there is no perfect overlap for $\varkappa = \kappa/2$. Further, the emission from two atoms coupled to a chiral waveguide does not drop as far as the system of two superatoms in free space both with coherent coupling to some internal dark state. This is attributed to the chiral nature of the waveguide-coupling.

From the above discussion, it is clear that two superatoms with coherently coupled bright and dark states can be tailored to mimic the dynamics of a chiral waveguide. However, the introduction of such an internal coherent coupling is merely an abstraction to describe the expected coupling between the different collectively excitede single excitation states of an N-atom system. We will return to this point in chapter 4. Yet, from figure 3.21 b) and d) we already conclude that the internal dynamics of the collectively coupled superatom ensembles can overshadow effects stemming from the directionality of the superatoms.

3.7.4 Realistic parameters and driving pulse

The introduction of internal superatom dynamics leads us to the final step of this analysis, where we consider a system of two superatoms driven with an incoming pulse with experimentally relevant parameters. We use the model shown in figure 3.20 b), keeping two dark states,
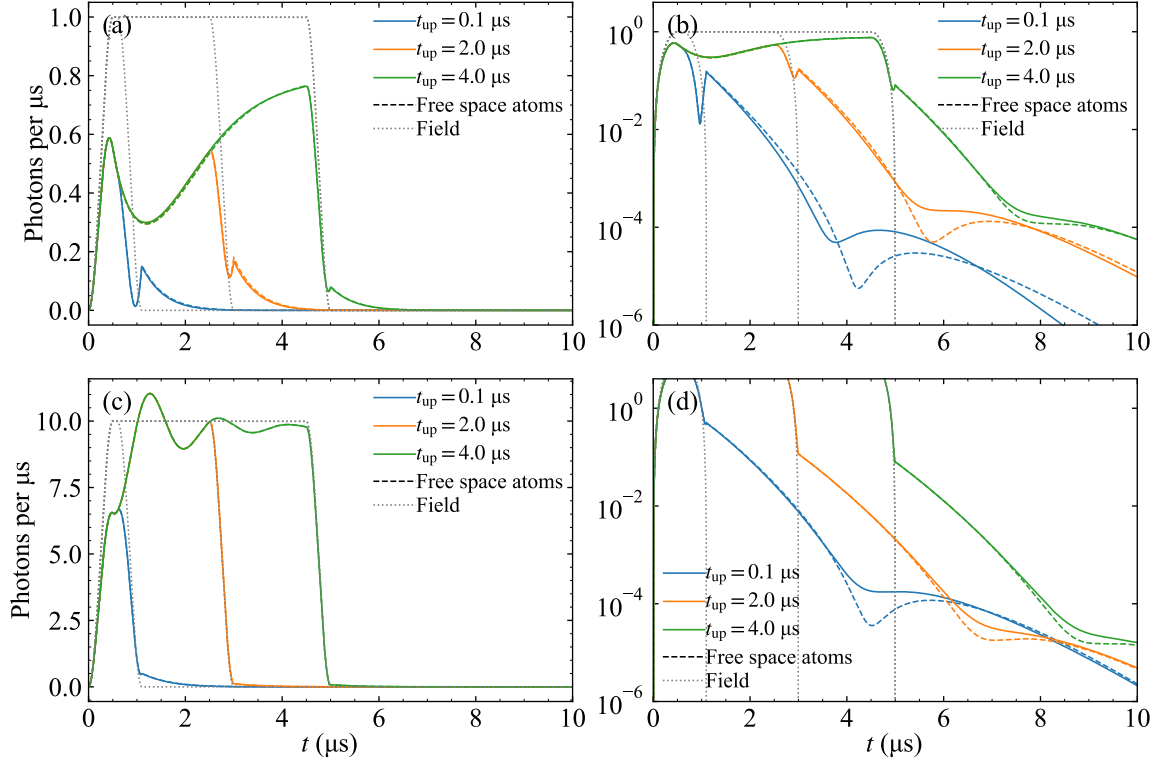
Figure 3.22: Model calculations for two superatoms coupled to a chiral waveguide with $\kappa = 0.5\,\mu\text{s}^{-1}$, $\Gamma = 0.1\,\mu\text{s}^{-1}$, $\gamma_D = 1\,\mu\text{s}^{-1}$, and $\varkappa = 0.3\,\mu\text{s}^{-1}$ driven with different fields. The dotted line shows the driving field, and the colors show the atom response for different pulse lengths. The dashed lines show the response from two superatoms in free space. a) and b) show the calculations for $\mathcal{R}_{\text{in}} = 1\,\mu\text{s}^{-1}$ on a linear and a semi-logarithmic scale respectively. c) and d) show the calculations for $\mathcal{R}_{\text{in}} = 10\,\mu\text{s}^{-1}$ on a linear and a semi-logarithmic scale respectively.

$|D\rangle$ and $|C\rangle$. The dephased dark state $|D\rangle$ is populated via irreversible dephasing from $|W\rangle$ and $|C\rangle$ with rate γ_D, while $|C\rangle$ couples coherent to $|W\rangle$ with coupling strength $\varkappa$, but does not itself couple directly to $|G\rangle$. This model will be discussed in detail in chapter 4.

Figure 3.22 shows the model predictions for driving two two-plus-two-level superatoms coupled to a chiral waveguide. The figure also includes as dashed lines the predictions for the free-space situation. The parameters chosen are $\kappa = 0.5\,\mu\text{s}^{-1}$, $\Gamma = 0.1\,\mu\text{s}^{-1}$, $\gamma_D = 1\,\mu\text{s}^{-1}$, and $\varkappa = 0.3\,\mu\text{s}^{-1}$. The choice of $\varkappa$ will be discussed in chapter 4. These figures again show how the internal couplings determine the decay rate. It also shows that we do expect to observe a difference in emission from chirally coupled atoms compared to atoms which are not subject to chiral coupling, but the difference occurs in the weak emission long after the driving pulse.

Figure 3.23 show the same as figures 3.22, but with $\kappa = 1\,\mu\text{s}^{-1}$. The other parameters are left unchanged. From these figures it is clear that as the coupling is increased the dynamics become more different between the chirally coupled and not chirally coupled system. In particular the larger difference between $\varkappa$ and κ gives rise to different timescales of emission drop-offs.
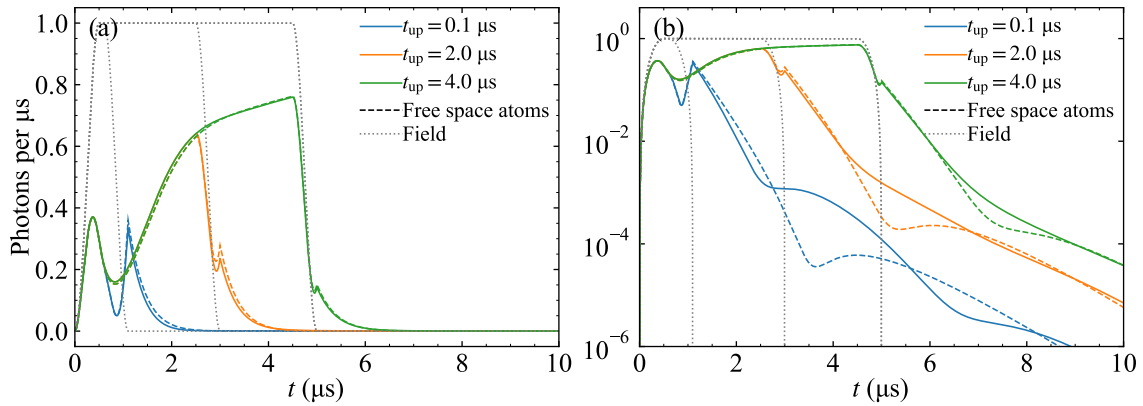
Figure 3.23: Model calculations for two superatoms coupled to a chiral waveguide with $\kappa = 1.0\,\mu\text{s}^{-1}$, $\Gamma = 0.1\,\mu\text{s}^{-1}$, $\gamma_D = 1\,\mu\text{s}^{-1}$, and $\varkappa = 0.3\,\mu\text{s}^{-1}$ driven with a field of $\mathcal{R}_{\text{in}} = 1\,\mu\text{s}^{-1}$. The dotted line shows the driving field, and the colors show the atom response for different pulse lengths. The dashed lines show the response from two atoms in free space. a) and b) shows the calculations on a linear and a semi-logarithmic scale respectively.

3.7.5   Measuring waveguide coupling

Finally, we can consider our options for measuring the waveguide-mediated coupling discussed in this chapter. Figure 3.23 indicates that a waveguide-mediated effect could be observed for Rydberg superatoms, but it is important to recognize that the experimental setup discussed in this thesis does not allow for reference measurements as the ones plotted with dashed lines in figures 3.23. Also, the current implementation of dimple traps allows us to investigate individual superatoms, but the sub-systems do not sum perfectly to the combined system due to imperfect superatom loading. Hence, characterizing the sub-systems precisely is also a remaining challenge. Without a clear comparison system, it is necessary to identify some figure of merit of waveguide-mediated coupling in order to claim observation of superatom-superatom interaction. The observation of such a fingerprint can be obscured by any internal coherent dynamics in the superatoms.

It is also relevant to note that the discussion given here relies on the superatoms coupling perfectly to each other through the waveguide, that is, we assume that $J_{12} = J_{12,\text{max}}$ and neglect phase acquired by the light travelling between the emitters. This assumption, however, is not necessarily justified given the definition of J_{12}, see eq. 2.33. In the following chapter, we return to the consideration of internal coherent coupling within a single Rydberg superatom.

Chapter 4

Internal dynamics of a single Rydberg superatom

In the previous chapter we introduced Rydberg superatoms consisting of N atoms as effective two-level systems. We described how they are formed experimentally with Rydberg excitations in small ensembles of ultracold atoms, and we reviewed the previously obtained results where the influence of a single Rydberg superatom on a driving field was measured. Finally, we considered the cascaded decay of an excited chain of superatoms described as a system of waveguide-coupled emitters.

The superatom itself with its N constituent atoms is also expected to exhibit dynamics similar to what is found for a chain of waveguide-coupled two-level systems. In chapter 2 we outlined how there are N different collective states of a single excitation shared between N emitters, of which only one couples strongly to the driving field. However, some coupling between the different excited states is expected [84].

In this chapter we probe a single Rydberg superatom with a pulse of varying length. This prepares different internal states of the superatom. We then measure the emission after extinguishing the driving pulse. We find that the emission rate from the superatom depends on the length of the driving pulse and thus on the collective internal superatom state. We assume that this finding can be attributed to coherent internal dynamics and test this assumption by comparing the experimental findings to a model which includes internal coherent coupling. This is an extension of the simple model described in section 3.3, and similar to the model discussed in section 3.7.

The results discussed in this section are the outcome of the first project within the scope of this thesis. They were published in Physical Review Research in 2020 [156]. Additional theoretical description of the waveguide system was published in Physical Review A [116].

4.1   Measuring internal dynamics

To investigate the internal dynamics of a single Rydberg superatom we prepare the superatom following the procedure lined out in section 3.5. In the experiment discussed here, the Rydberg superatoms were formed by roughly 2×10^4 atoms, yielding an OD on the single photon transition of ~ 10 with temperature $\approx 9\,\mu\mathrm{K}$. A sketch of the experimental setup is shown in figure 4.1. The probe and control-beams are counterpropagating through the superatom. We couple to the $|111S, J = 1/2, m_j = 1/2\rangle$-state with control Rabi frequency $2\pi \times 13\,\mathrm{MHz}$ measured on EIT resonance. We work far-detuned from single photon resonance but on two
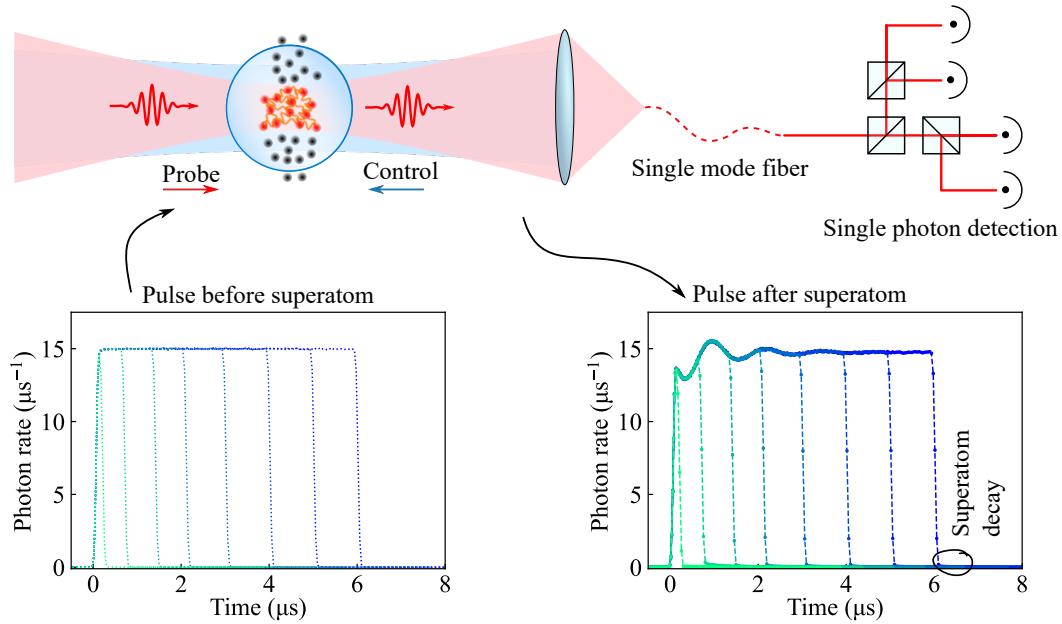
Figure 4.1: Illustration of the experimental setup and procedure discussed in this chapter. A single Rydberg supearatom is probed with few-photon probe pulses of varying pulse length. The probe light is coupled into a single mode fiber and detected with single photon counters. In the detected pulses we observe the coherent dynamics of the superatom interacting with the light. We study the decay of the superatom after the extinguishing of the probe pulse, by considering the emission after the driving pulse is over.

photon resonance as discussed in section 3.1, with $\Delta \geq 2\pi \times 100$MHz. We verify that we are working on the resonance by doing Rydberg spectroscopy based on ion detection as discussed in section 3.5.

To investigate the internal dynamics, we probe the superatoms with few-photon probe pulses of varying length. We use Tukey-shaped probe pulses with very short risetimes, on the order of $0.13\,\mu$s. We vary the pulse lengths between $0.3\,\mu$s and $6.10\,\mu$s. The probe light is coupled into a single mode fiber and distributed on four SPCM's in a Hanbury-Brown and Twiss-setup as discussed in section 3.4. By coupling the probe light into a single mode fiber, we ensure that we measure only transmission throuh and emission from the superatom into the probe mode. The probability that non-directional emission from the superatom is coupled into the fiber is negligible.

A few examples of the transmitted probe pulses are shown in figure 4.2 a). We observe oscillations in the transmitted intensity which reflect the superatom Rabi oscillations corresponding to the absorption and reemission of a single photon as discussed in section 3.5.2. As the driving pulses end at different times in the oscillatory dynamics, we can explore the decay of the excitation as a function of the internal superatom state. This approach of changing the pulse length to prepare the system in a different internal state is also used in for instance ref. [157]. In principle, the superatom state should also affect the actual pulse shape [158]. In figure 4.1 and figure 4.2 a) the rising edges of the pulses have all been adjusted for visual clarity such that they coincide with the origin of the time axis. In practice, we fix the pulses such that they all end at the same time.
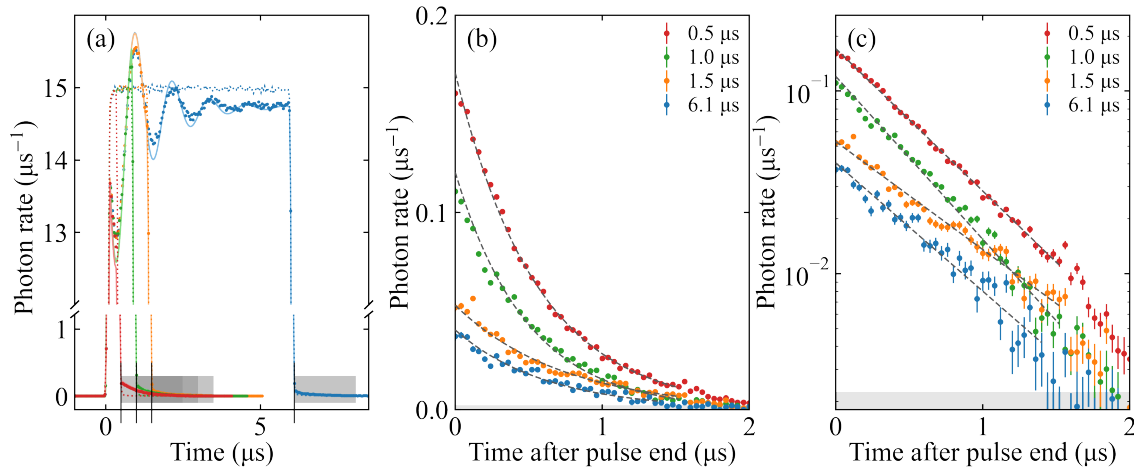
Figure 4.2: Selected pulses of different length and resulting emission after the end of the driving pulse. a) A selection of pulses. Experimental measurements are shown as points, the dashed lines show reference measurements. Solid lines show model predictions based on fits to the experimental data and calculated for the input Tukey-pulses. Notice the break in the y-axis. The grey rectangles mark the tails which are the basis of the subsequent analysis. b) The tails of the pulses shown in a). Different pulse lengths yield different reemission of light after the end of the driving pulse. It is clearly seen that the photon flux depends on the oscillations of the superatom. Experimental data is shown as points, and dashed lines show the results of linear fits to the logarithm of the data shown here. c) shows the same as b) on a logarithmic scale. On this scale it is clear that different pulse lengths also yield different rates of decay. In particular, we observe a speeding up of the decay rate as the system is going through different internal states. For the very short pulses we observe a slow decay, while we reach much faster decay-rates for 1.0 μs pulses. Dashed lines show linear fits to the shown data as discussed in the main text. Parts of this figure are originally published in [156].

In the following, we investigate the emission from the superatoms after the end of the driving pulse. The time-windows in which we investigate the emission are highlighted in figure 4.2 a) as grey areas and shown in figure 4.2 b) on a linear scale and again in c) on a semi-logarithmic scale. The data in panels b) and c) have been corrected for leaking probe light due to imperfect extinction by subtracting the reference pulses from the measurements with atoms. Since the measurements presented in this chapter rely on emission of single photons, we verify that only single photons are emitted after the end of the pulse by measuring the second order correlation function, $g^{(2)}(\tau = 0)$, which we find to be < 0.1 consistent with single photon emission.

Figure 4.2 b) shows how the photon flux at the end of the driving pulse depends on the state of the superatom. This is intuitive: The amplitude of reemission into the forward mode depends on the probability of the superatom being excited.

From the slopes of the photon flux in the logarithmic plot in figure 4.2 c), it becomes clear that not only the initial photon flux after the pulse, but also the rate of emission depend on the length of the driving pulse. The different slopes indicate that the superatom is prepared in states with different decay rates.

To extract estimates for these two characteristic values we assume that the superatom excitation decays approximately exponentially and apply a linear fit to the logarithm of the
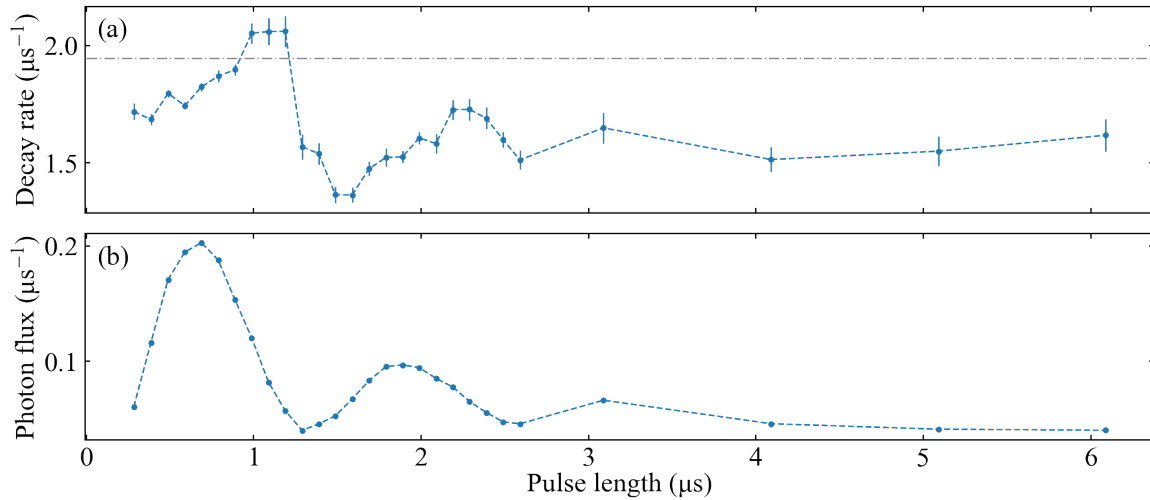
Figure 4.3: The results of exponential fits to decay of superatom as shown in figure 4.2. The points are fit results. The dashed line serves as a guide to the eye and connects neighbouring points. a) decay rate. The dot-dashed line shows $\kappa + \Gamma + \gamma_D$ extracted from the two-plus-one-level model discussed in section 3.3. b) photon flux at the end of the pulse.

tail shown in figure 4.2 c). We only include data points where the number of photons in each time-bin of 20 ns is significantly larger than the dark count rate. Thus, we define a threshold where no less than 50 counts have been detected in each time-bin. This threshold is shown in figure 4.2 c) as a grey area.

The results are shown in fig 4.3. Figure 4.3 a) shows the initial emission rate, and figure 4.3 b) shows the photon flux. Both exhibit oscillatory behavior as a function of pulse length. The variation in initial photon flux as shown in figure 4.3 b) is expected as a result of the Rabi oscillations of the superatom and is also captured by the two-plus-one level model discussed in section 3.3. The change of decay rate, however, is not captured by the model, which predicts that the emission decays exponentially with a constant rate given by $\kappa + \Gamma + \gamma_D$ [1]. These values can be extracted from the fits to the output signal for a given input signal as discussed in chapter 3.4. The constant decay rate is shown in figure 4.3 a) as a dash-dotted line.

Consequently, the experimentally observed decay rates indicate the presence of dynamics not captured by the model: The presence of an additional coherent process, not between the ground state and the excited state of the superatom, but in the manifold of excited states as discussed in section 2.2. We investigate whether this observation is also present for different coupling strengths of the superatom to the driving field. Equation 3.7 shows that the coupling strength of the superatom to the driving field depends on the detuning Δ from single photon resonance as $\kappa \propto \Delta^{-2}$. Therefore, we repeat the measurements shown in figure 4.2 for different values of Δ and for different and driving field strengths. The different parameters are summarized in table 4.1. The decay rates and photon fluxes extracted from these measurements are shown in figure 4.4.

Comparing the curves in figure 4.4 a) and c) we see that an increase in Δ and thus a decrease

---

[1]It may seem counter-intuitive that Γ and γ_D, which are not related to the coupling to the driving field and thus emission into the forward mode, appears in the decay rate. However, the superatom emission depends on the population in the bright state, and this population decays as a function of both κ, Γ and γ_D. Thus, while κ determines the amplitude of the emitted light, Γ and γ_D contribute to the rate of decay from the bright state.
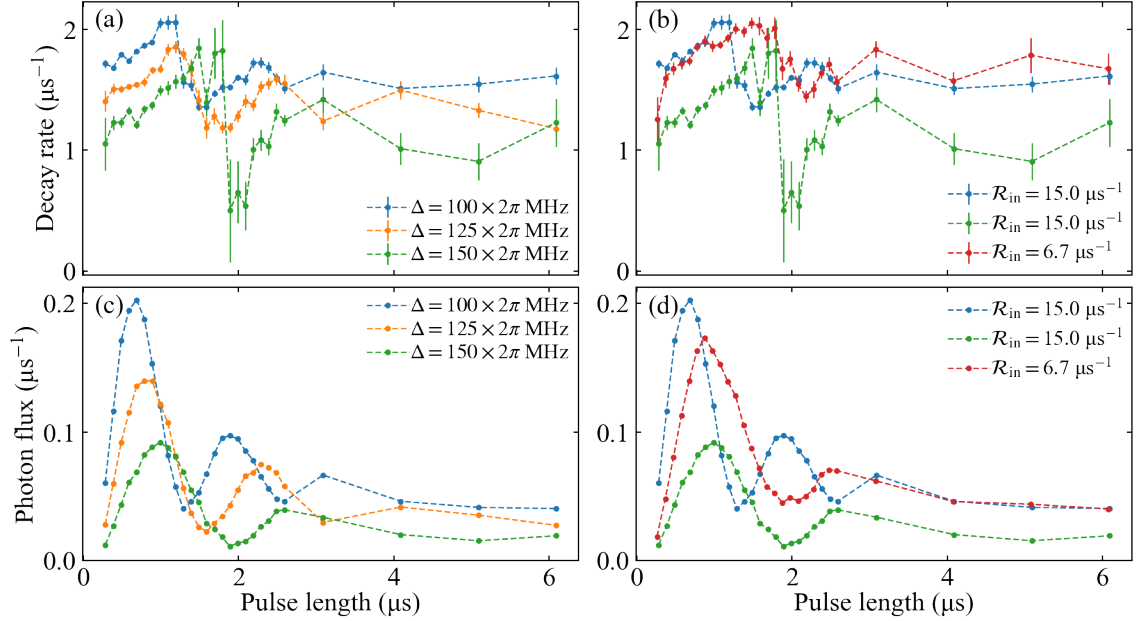
Figure 4.4: Decay rates and initial photon fluxes for different values of detuning Δ and input photon rate $\mathcal{R}_{\mathrm{in}}$. Note that the results from the same datasets are plotted in multiple figures. The colors indicate the same sets. a) and b) show the fitted decay rate and c) and d) show the photon flux. a) and c) show results for datasets with $\Delta = 2\pi \times 100\,\mathrm{MHz}$, $2\pi \times 125\,\mathrm{MHz}$, and $\Delta = 2\pi \times 150\,\mathrm{MHz}$. One sees how the resulting variation of coupling strength is reflected in the decay rate and the oscillatory dynamics. b) and d) show the decay rate and initial photon flux for $\Delta = 2\pi \times 100\,\mathrm{MHz}$ and $\Delta = 2\pi \times 125\,\mathrm{MHz}$. For $\Delta = 2\pi \times 100\,\mathrm{MHZ}$ the data shows two different values of $\mathcal{R}_{\mathrm{in}}$, $\mathcal{R}_{\mathrm{in}} = 6.7\,\mathrm{\mu s}^{-1}$ and $\mathcal{R}_{\mathrm{in}} = 15.0\,\mathrm{\mu s}^{-1}$ respectively. One notices that some datapoints have very large error bars. These points correspond to fits with very low photon rates, which is also seen in the photon flux.

of κ leads to a slower oscillation in both decay rate and initial photon flux. This reflects the corresponding change in Rabi frequency of the driving of the superatom. For increasing Δ we observe a lower decay rate, which corresponds to expectations since increasing Δ leads to a lower Raman decay rate Γ, and a lower forward emission rate, given by κ.

In figure 4.4 b) and d) we investigate the effect of changing the input photon rate $\mathcal{R}_{\mathrm{in}}$. We observe a slower oscillation in both the initial photon flux and the decay rate for a lower driving field. However, the decay rates shown in panel b) has the same magnitude for the same value of Δ. Changing the input photon rate determines the effective Rabi frequency of the superatom, but it does not change the coupling strength κ. Thus, by varying Δ and $\mathcal{R}_{\mathrm{in}}$ we explore whether the observed changes in decay rate are related to the coupling strength or the driving field. We find no clear dependency on either of the varied parameters: The oscillations persist and maintain their qualitative shape throughout the parameter variation.

To obtain a better understanding of the observations in figure 4.4 we compare these observations to a model which includes an additional internal coherent coupling between excited states of the superatom.

Table 4.1: Parameters for two-plus-one-level system as discussed in the main text.

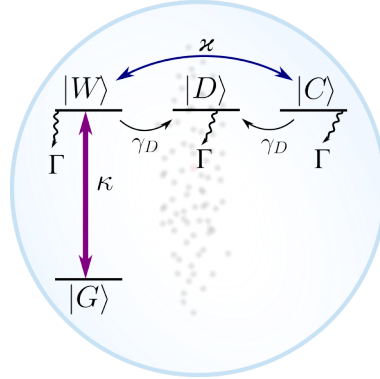| $\Delta/2\pi$ (1/µs)	$\mathcal{R}$ (1/µs)	No. Measurements
100	15.0	$1111 \cdot 10^3$
125	15.0	$621 \cdot 10^3$
150	15.0	$467 \cdot 10^3$
100	6.7	$377 \cdot 10^3$

Figure 4.5: Sketch of the extended model which now features a dark state $|C\rangle$ which couples coherently to the bright state with coupling strength $\varkappa$. $|C\rangle$ simulates the subset of other singly excited collective states which can couple to $|W\rangle$. This model has already been discussed in figure 3.20.

4.2 Extended model including internal dynamics

The superatom is an ensemble of N atoms sharing a collective excitation. Thus, for a full microscopic description it is necessary to take into account all the possible collective states of the N-emitter system and the couplings between them, as discussed in chapter 2. Previously, we have considered a two-plus-one-level model shown in figure 3.4 to describe the superatom dynamics based on the assumption that coherent coupling between the excited states is weak compared to superatom dephasing such that the coherence can be neglected. In particular, it is assumed in this model that only $|W\rangle$ couples to the light, and that $|W\rangle$ only couples incoherently to the dark states [159]. These dark states have previously all been abstracted into a single dark state $|D\rangle$ except briefly in section 3.7. This model introduced in section 3.3 provides a good description of the superatom interacting with a driving field as shown in section 3.4. However, the oscillations in the superatom emission rates after the driving pulse observed in our experiment are not reproduced. This suggests that the assumption that coherent coupling between excited states can be neglected is not valid.

In principle, all N excited states and their mutual couplings would need to be considered to model the system dynamics. As this is computationally demanding, we take a similar approach as for the two-plus-one-level model and extend this model with a single additional dark state $|C\rangle$, which is coherently coupled at rate $\varkappa$ to the bright state $|W\rangle$ as shown in figure 4.5. The resulting system Hamiltonian is given by

$$H_0(t) = 2\hbar\sqrt{\kappa\mathcal{R}_{\text{in}}}\sigma_{\text{GW}}^{\dagger} + \hbar\varkappa\sigma_{\text{CW}}^{\dagger} + \text{h.c.}. \tag{4.1}$$

This two-plus-two-level model was briefly considered in section 3.7. The state $|C\rangle$ is subject to dephasing into the dark state $|D\rangle$ with rate γ_D and single-atom decay back to the ground
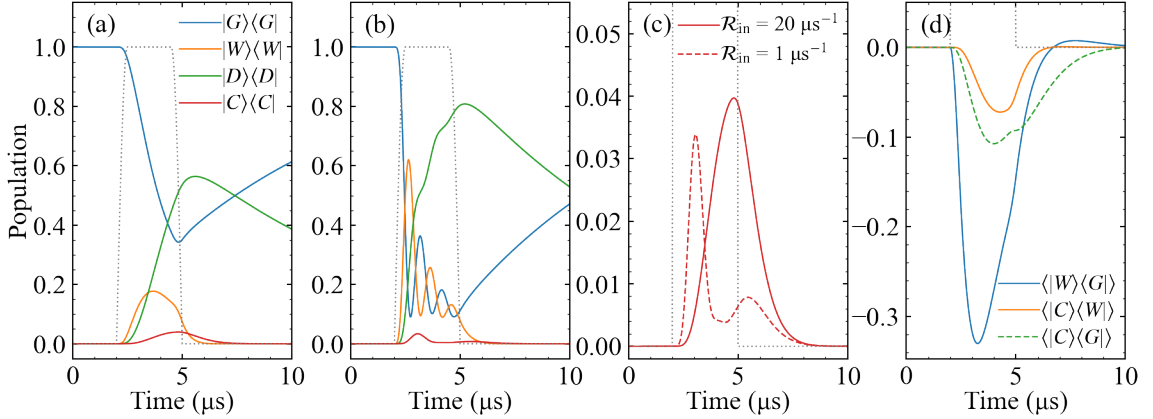
Figure 4.6: Populations and coherences in a Rydberg superatom with internal dynamics driven with a field of varying strength. The parameters are $\kappa = 0.5\,\mu s^{-1}$, $\Gamma = 0.1\,\mu s^{-1}$, $\gamma_D = 1.5\,\mu s^{-1}$, and $\varkappa = \kappa$. a) and b) show all populations for driving pulse with rate $\mathcal{R}_{in} = 1\,\mu s^{-1}$ and $\mathcal{R}_{in} = 20\,\mu s^{-1}$ respectively. c) shows only the population in $|C\rangle$ for the two different photon rates. d) shows the coherences. For visual clarity, only the coherences for $\mathcal{R}_{in} = 1.0\,\mu s$ are shown. Solid lines indicate imaginary values, the dashed line indicates a real-valued coherence between $|W\rangle$ and $|C\rangle$. The grey, dotted line shows the driving pulses normalized to one.

state $|G\rangle$ with rate Γ. There is no emission into the forward mode from $|C\rangle$.

The time-evolution is described by the master equation

$$\partial_t \rho(t) = -\frac{i}{\hbar}\left[H_0(t), \rho(t)\right] + (\kappa + \Gamma)\mathcal{D}[\sigma_{GW}]\rho(t) + \gamma_D \mathcal{D}[\sigma_{DW}]\rho(t) + \Gamma\mathcal{D}[\sigma_{GD}]\rho(t)$$
$$+ \gamma_D \mathcal{D}[\sigma_{DC}]\rho(t) + \Gamma\mathcal{D}[\sigma_{GC}]\rho(t). \tag{4.2}$$

As in equation 3.18 we define $\sigma_{\mu\nu} = |\mu\rangle\langle\nu|$, and $\mathcal{D}[\sigma] = \sigma\rho\sigma^\dagger - (\sigma^\dagger\sigma\rho + \rho\sigma^\dagger\sigma)/2$ is the Lindblad dissipator. The last two terms in equation 4.2 capture the decay of $|C\rangle$ into $|G\rangle$ and $|D\rangle$.

We introduce a new state $|C\rangle$ rather than a weak coherent coupling between $|W\rangle$ and $|D\rangle$ based on the expectation that the coherent coupling predominantly occurs to a small subset of dark states which we condense into $|C\rangle$. Dephasing with rate γ_D also populates dark states with much weaker coherent coupling to $|W\rangle$. Therefore it is very unlikely that population once transferred into one of these states will ever return to $|W\rangle$, and we continue to treat these states separately as $|D\rangle$.

In figure 4.6 we show how the populations in the different superatom states evolve under driving for $\kappa = 0.5\,\mu s^{-1}$, $\Gamma = 0.1\,\mu s^{-1}$, $\gamma_D = 1.5\,\mu s^{-1}$, and $\varkappa = \kappa$. In panel a) the system is weakly driven with rate $\mathcal{R}_{in} = 1\,\mu s^{-1}$. We see how only a small population builds up in $|W\rangle$ during the pulse, because of the fast decay into $|D\rangle$. In panel b), where $\mathcal{R}_{in} = 20\,\mu s^{-1}$ the coherent dynamics between $|W\rangle$ and $|G\rangle$ are faster than γ_D, and the model predicts visible Rabi oscillations between $|W\rangle$ and $|G\rangle$. Meanwhile, the population of $|C\rangle$ is weak due to the comparatively weak coupling $\varkappa$. Panel c) shows a zoom-in on the populations of $|C\rangle$ for both photon rates. For $\mathcal{R}_{in} = 20\,\mu s^{-1}$, this population undergoes an oscillation correlated with the coherent return to $|G\rangle$ from $|W\rangle$ and the population of $|D\rangle$.

In figure 4.6 d) we show the coherences between $|W\rangle$ and $|G\rangle$, $|W\rangle$ and $|C\rangle$, and $|C\rangle$ and $|G\rangle$ under weak driving. The strong drive is excluded for visual clarity. The figure shows a build-up of coherence between the $|W\rangle$ and $|C\rangle$, and also a real-valued coherence between $|C\rangle$ and $|G\rangle$ which is mediated by the coupling between $|C\rangle$ and $|G\rangle$, similar to an EIT system
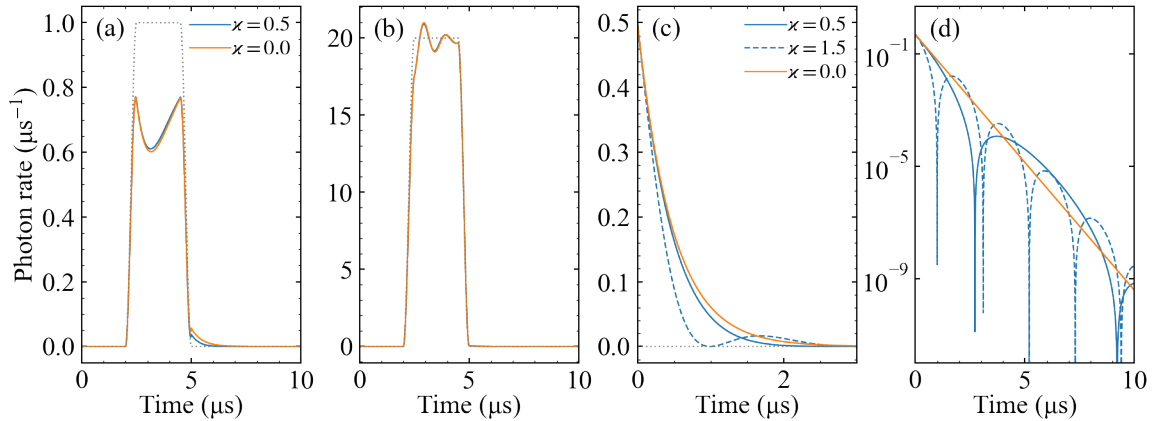
Figure 4.7: Transmission of a driving pulse through the superatom with and without coherent internal coupling for different driving fields, and emission from the system prepared fully in the bright state. The parameters are $\kappa = 0.5\,\mu\mathrm{s}^{-1}$, $\Gamma = 0.1\,\mu\mathrm{s}^{-1}$, $\gamma_D = 1.5\,\mu\mathrm{s}^{-1}$, and $\varkappa = \kappa$. In c) and d) we also shown the situation of $\varkappa = 3\kappa$. a) and b) show the transmission of the pulses shown in figure 4.6 a) and b). c) The emission from the system starting in the bright state. d) Same as c) but on a semi-logarithmic plot. The fact that the emitted light does not go to zero in the emission-dips is due to the coarseness of the calculation.

as discussed in section 3.1. When the system is prepared in $|W\rangle$ and no field is applied, this coherence does not build up.

As with the two-plus-one-level model, we can now predict the transmission and emission of light into the forward direction based on the populations and coherences of the superatom. Figure 4.7 is calculated for the same parameters as figure 4.6. Panels a) and b) show the intensity under driving with the same pulses as in figure 4.6, calculated with the two-plus-one-level model ($\varkappa = 0$), and with the two-plus-two-level model ($\varkappa = 0.5\,\mu\mathrm{s}^{-1}$). The panels show that the two models predict slightly different behavior during the drive, but the difference is minimal.

In panels c) and d), we consider the decay from a superatom prepared in $|W\rangle$, also showing in addition the behavior for $\varkappa = 1.5\,\mu\mathrm{s}^{-1}$ and observe that the presence of coherent coupling leads to a non-exponential decay. In particular, the semi-logarithmic plot in panel d) highlights that the additional coherently coupled dark state $|C\rangle$ allows for population transfer in and out of the emitting bright state. This transfer gives rise to oscillatory dynamics on a timescale determined by $\varkappa$.

4.2.1 Comparison of waveguide-coupled emitters and model

To benchmark how well the simplified two-plus-two-level model captures the coherent dynamics of a many-emitter system, we compare it to the behavior of 1000 two-level atoms arbitrarily distributed along a one-dimensional, chiral waveguide, as discussed in chapter 2. We consider all 1000 collectively singly excited states.

Figures 4.8 a) and b) show the predicted emission out of the waveguide-system for driving pulses of varying lengths for $\kappa = 0.45\,\mu\mathrm{s}^{-1}$ and $\kappa = 1\,\mu\mathrm{s}^{-1}$, respectively. We assume perfect waveguide coupling ($\Gamma = 0$). The coupling between the different excited states follows from κ as discussed in chapter 2. The simulations of 1000 atoms coupled to a chiral waveguide shows non-exponential emission into the waveguide after the end of the driving pulse. For
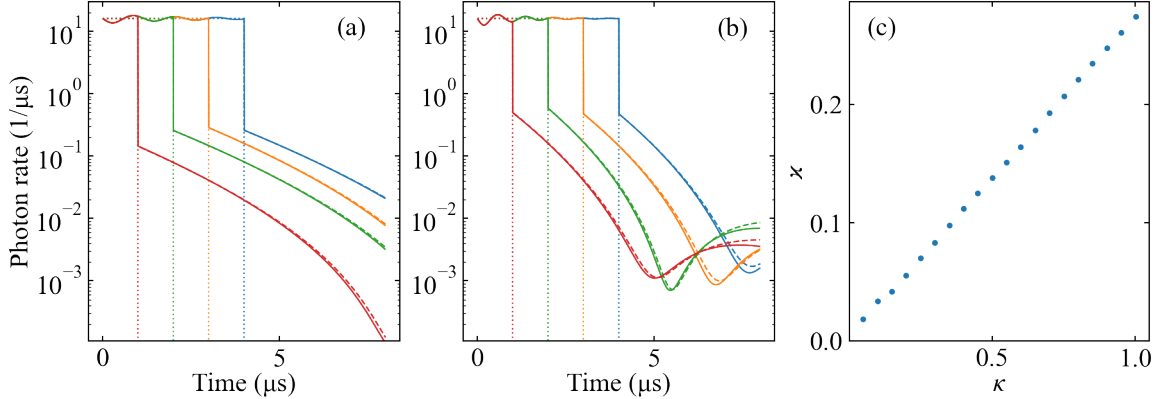
Figure 4.8: Comparison between the numerical solution of N stationary emitters coupled to a waveguide and the two-plus-two-level model. The waveguide is driven with a square pulse, and the pulse length is varied as in the experiments. a) and b) show fits of the two-plus-two-level model for two different values of waveguide coupling. a) shows $\kappa = 0.45\,\mu s^{-1}$, b) shows $\kappa = 1\,\mu s^{-1}$. Solid lines are results from the numerical solution of N stationary emitters collectively coupled to a waveguide, and the dashed lines show the two-plus-two-level model fitted to the waveguide emission. c) shows the relation between the fit-parameters for κ and the coherent coupling strength $\varkappa$. For a one-dimensional waveguide the relation between κ and $\varkappa$ appears to be linear. This figure originally appeared in [156].

$\kappa = 1\,\mu s^{-1}$ the first drop and revival of emission after the pulse happens within the simulated time window.

We fit the two-plus-two-level model to the forward emission calculated for the full waveguide model. The results are also shown in figure 4.8 a) and b). They demonstrate excellent qualitative agreement. The models start to deviate at large times after the end of the pulse, where the signal is far weaker than the experimentally observable level. Finally, as shown in figure 4.8 we find a linear relation between the fit-results for κ and $\varkappa$ when the two-plus-two-level model is fitted to the calculated emission in 1D. This is expected from the discussion in section 2.3.1, and in particular from equation 2.33.

4.3 Application of the model to the experimental data

After we have established that the two-plus-two-level model captures the coherent dynamics of N atoms coupled to a waveguide, we apply the model to our experimental data to investigate whether the observed change of emission rates can be caused by coherent internal coupling between collectively excited states.

To obtain the model parameters, we fit the transmission of the probe pulse through the superatom. The fitting procedure has the following steps: We fix Γ to the predicted value given by the natural decay rate of the excited state, Γ_e the control Rabi frequency, measured on EIT resonance, and the detuning Δ,

$$\Gamma = \Gamma_e \frac{\Omega_c^2}{2\Delta^2}. \tag{4.3}$$

Then we fit the two-plus-one-level model to the transmission to obtain κ. Next we fit the two-plus-two-level model with $\varkappa$ and γ_D as free parameters.

Table 4.2: Parameter sets for model fits to experimental data.

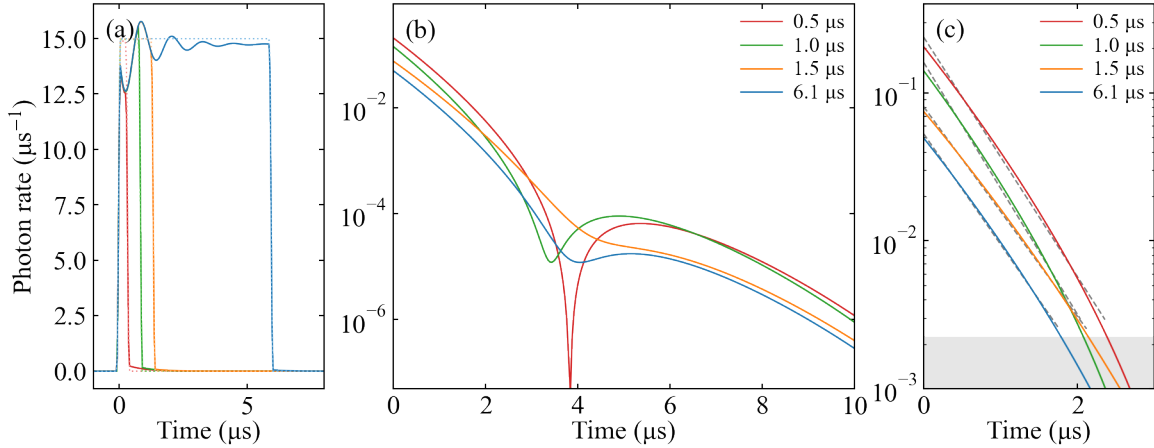| $\mathcal{R}$ (μs^{-1})	$\Delta/2\pi$ (μs^{-1})	κ (μs^{-1})	Γ (μs^{-1})	γ_D (μs^{-1})	$\varkappa$ (μs^{-1})
15.0	100	0.46	0.15	0.85	0.31
15.0	125	0.32	0.10	0.85	0.32
15.0	150	0.21	0.064	0.85	0.31
6.7	100	0.47	0.15	0.85	0.34

Figure 4.9: Model prediction for superatom behavior for the parameters obtained by fitting the data shown in figure 4.2. a) Full pulses. The dotted lines show the input pulses which are found by fitting Tukey-pulses to the experimental reference measurements. c) The long-time behavior of the system shows how the emission into the probe mode vanishes completely for short pulses. b) a zoom in on the logarithm of the tails. The dashed lines show linear fits to the tails. The gray area indicates where the fits end. For consistency the same number of points have been used as in the experiment.

The parameters obtained this way capture the dynamics during the pulse well, but we find that $\gamma_D \approx 1\,\mu s^{-1}$ predicts too fast decay after the end of the pulse.

We attribute this overestimation of γ_D to decoherence channels which are not described by the model, such as finite laser linewidth, which is only present during the driving. Therefore we adjust the value of γ_D to a value which captures the decay rate after the pulses are over. Since the suspected decoherence channels are independent of driving field strength and detuning, we chose the same value $\gamma_D = 0.85\,\mu s^{-1}$ for all datasets. This adjustment of γ_D does not lead to a significant modification of the dynamics during the pulse. The fits are performed for the four data sets listed in table 4.1, and the resulting parameters are summarized in table 4.2. As can be seen in figure 4.2 a) where the model prediction is plotted together with experimental data the dynamics of the superatom-light interaction during the driving pulse are well captured.

Reviewing the parameters in table 4.2 we note that the value of κ scales with $\sim 1/\Delta^2$ as expected. In figure 4.8 c), we found that $\varkappa$ scales linearly with κ for N emitters coupled to a one-dimensional waveguide. However, this tendency is not reflected in the fit results. Instead, we obtain similar values of $\varkappa$ for all values of κ. We attribute this deviation to the three-dimensionality of our system and the limited range of the fits. As opposed to the waveguide case, the individual atoms in the superatom are not restricted in their re-emission direction. In addition, the fits to the one-dimensional waveguide are reaching far into the experimentally

inaccessible intensity regime.

In figure 4.9 a) we show the fit results to the data shown in figure 4.2 a). As can be seen in panel b), the model predicts non-exponential decays i.e. a drop and revival of emission long after the end of the pulse. The drop becomes less pronounced for longer pulses as the system is subject to decoherence. This behavior only becomes discernible for very low intensities, as shown in panel b). To compare the model to the experimental data, we apply the same approach as for the experimental data to extract initial photon flux and decay rate: A linear function is fitted to the logarithm of the flux after the extinguishing of the driving pulse as shown in figure 4.9 c). The linear fit is only an approximation, and the dashed lines shown in panel c) clearly deviates from the model predictions. However, we employ the linear fits to treat model predictions and experiment in a similar way.

4.3.1 Comparison of decay rates

Figure 4.10 compares the decay rates and initial photon fluxes extracted from the fits to the model to the experimental data shown in figure 4.3. Notably, the two-plus-two-level model predicts similar oscillations in decay rates as seen in the experimental data. The good qualitative agreement between the model and the experimental data shown in figure 4.3 suggests that the oscillations of decay rates are indeed an indication of internal coherent coupling between the collective superatom states.

There are however deviations between the model predictions and the observed decay rates. The experimental data further exhibit larger changes of the decay rates than what is found by fitting a linear slope to the model predictions, as seen in figure 4.3 a), b, e), and f). In contrast, the fits to the model yield too high initial photon flux compared to the experimental results, see figure 4.3 c), d), g), and h). The deviations indicate that extraction of decay rates through linear fits is already too coarse in the intensity regime we consider. Further, the predictions are based on a highly simplified model that does not take individual collective states and coupling rates into account. Also, the model does not distinguish between different dephasing mechanisms, such as laser line-widths, spatially varying control intensity and AC Stark shifts for the atoms.

In this chapter we have studied the observation of internal dynamics of a Rydberg superatom containing a single excitation. The internal dynamics manifest itself in the emission of single photons after the end of a driving pulse. The observations presented here highlight how a Rydberg superatom, consisting of N emitters collectively sharing a single excitation is a platform for investigation of collective many-emitter-interactions.

The internal dynamics observed here are not only relevant for Rydberg superatoms, but for all systems where many emitters share excitations. The collective effects are often not included in the treatment of many-emitter systems which are otherwise suggested as promising for quantum computation and other applications [108]. Our experimental results indicate that the collective effects cannot be neglected in all cases, in particular not on the single photon level.

While the internal dynamics may pose a challenge, it has also been proposed to use collective effects as a way of processing and storing quantum information [38], and this approach is actively pursued and has recently led to the demonstration of retrieval of subradiantly stored excitations [160]. Here we consider a disordered ensemble, but platforms such as structured atom-arrays allow tailored light-emitter interactions [32, 35, 36]. This has recently been demonstrated with a subradiant mirror [39]. Similar applications have been suggested with Rydberg atoms [110, 111].
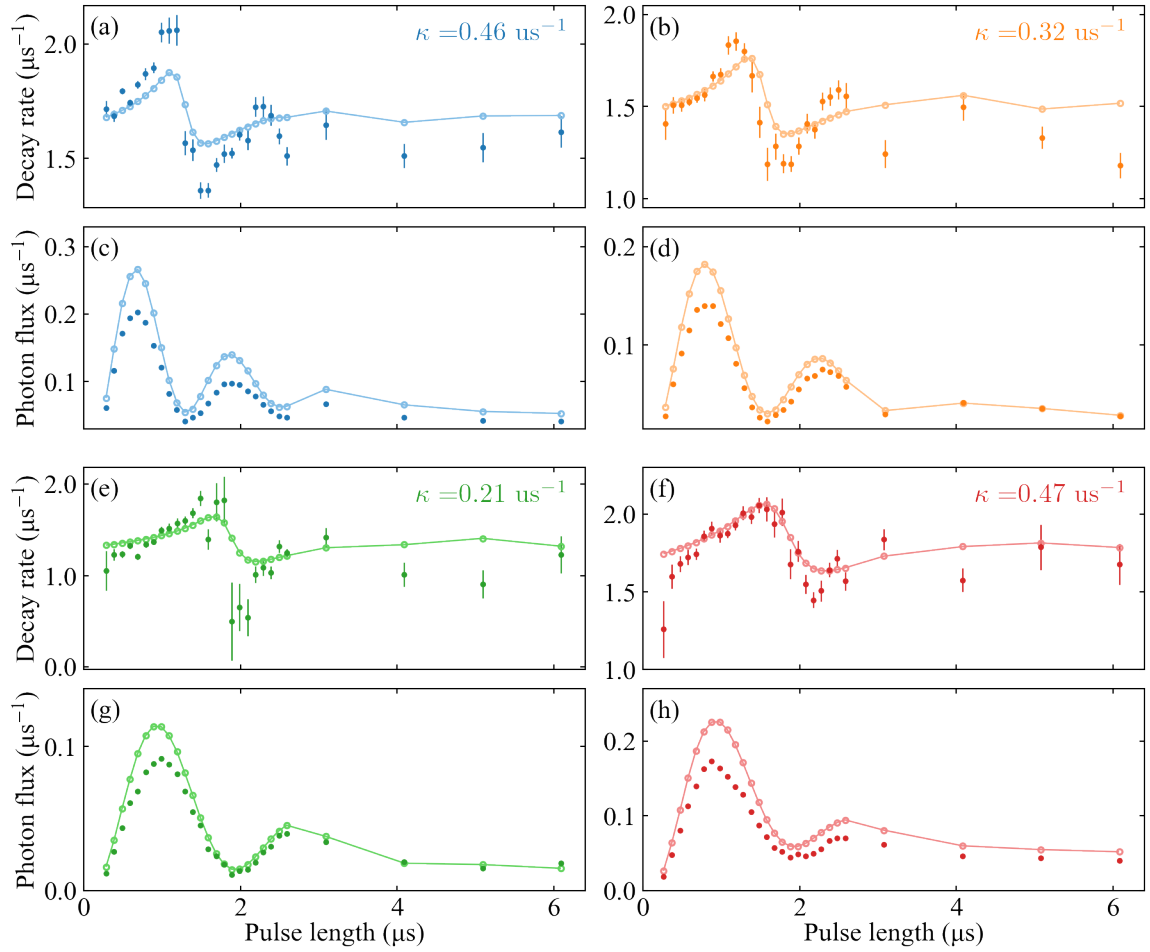
Figure 4.10: Comparison between experimental and model results of fitting a linear function to the tail after ended pulse. Solid points show fits to experimental data while open points show fits to the tails predicted by the two-plus-one-level model. a), b), e), and f) show the decay rate for different values of κ and $\mathcal{R}_{\text{in}}$, and c), d), g), and h) show the decay rate and initial photon flux for the same values. f) and h) are for $\mathcal{R}_{\text{in}} = 6.7\,\mu\text{s}^{-1}$. All other panels are for $\mathcal{R}_{\text{in}} = 15.0\,\mu\text{s}^{-1}$.

Chapter 5

Few-photon subtraction with Rydberg superatoms

While the previous chapter considered the internal dynamics of a single Rydberg superatom this chapter will look at a chain of multiple Rydberg superatoms. We demonstrate a the possibility of applying Rydberg superatoms for technical applications, specifically we show how to realize exact multi-photon subtraction. Reliable subtraction of photons has interesting applications in quantum optics: as a mean of creating non-classical states of light [161], to produce and process quantum information [162–164], and for enhanced sensing in quantum metrology [165].

We realize photon subtraction of up to $n_{\mathrm{sub}} = 3$ photons, using n_{sub} Rydberg superatoms as saturable single photon absorbers. This approach was first suggested in Ref. [159], and realized for $n_{\mathrm{sub}} = 1$ with a single Rydberg superatom in 2015 [78, 120]. Besides the extension to multiple absorbers, this chapter also presents an analysis of fundamental performance limitations and the potential for scaling beyond $n_{\mathrm{sub}} = 3$.

The approach of storing an absorbed photon in a third, dark state, has also been suggested for different systems [166–168], and implemented with a microsphere resonator [169].

This chapter begins with a discussion of how a Rydberg superatom is tuned to act as a single photon absorber, in particular by ensuring a high dephasing rate into the dark state. We then present the procedure to prepare n_{sub} identical superatoms and demonstrate multi-photon subtraction. The performance of the multi-photon subtraction depends on the parameters of the superatoms and the incoming probe pulse, and we identify the regimes where our scheme works reliably. Finally, this chapter presents a theoretical analysis of the fundamental limits of our scheme on the photon subtraction.

The results presented here are the outcome of the second project within the scope of this thesis. They were published in Nature Communications in 2021 [170].

5.1   Single photon absorption through dephasing

Figure 5.1 shows a sketch of the multi-photon subtraction scheme. To subtract n_{sub} photons from some input pulse, we create a system of n_{sub} cascaded Rydberg superatoms. Each superatom can to a good approximation be described by the two-plus-one-level system shown in figure 5.1: A collective ground state $|G\rangle$ is coupled to the forward-emitting state $|W\rangle$ with coupling strength κ. The bright state $|W\rangle$ contains a single Rydberg excitation shared between N constituent atoms.
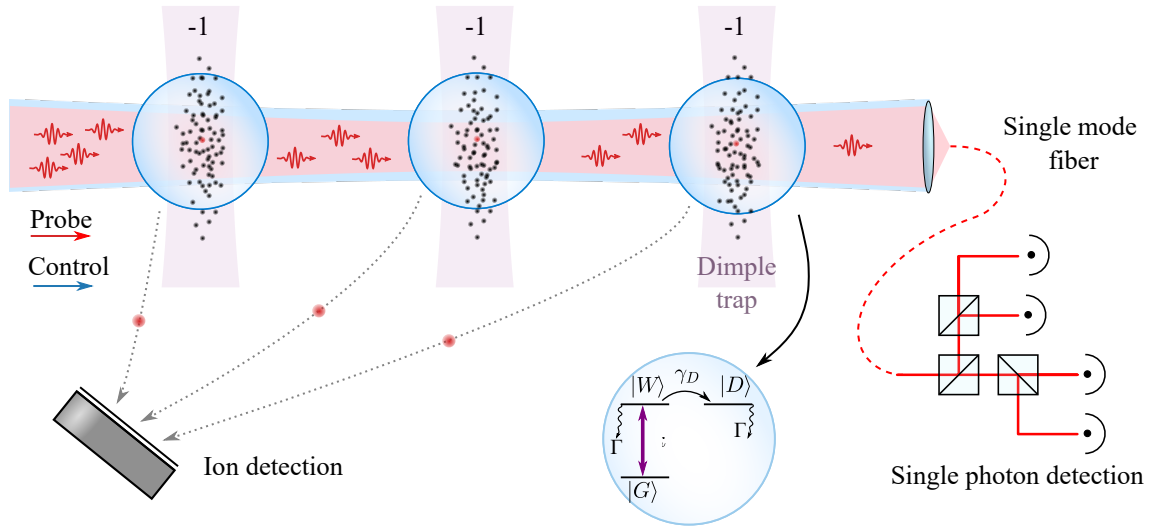
Figure 5.1: Experimental setup for realizing multi-photon subtractor. Up to three Rydberg superatoms are realized in dimple traps and probed with few-photon pulses. The transmitted light is coupled into a single mode fiber and detected on SPCMs in an HBT setup. After each experiment, any remaining Rydberg excitations are ionized and the ions are detected on an MCP. The superatoms are described by the two-plus-one-level model introduced in section 3.3.

In this simple model discussed in chapter 3, the bright state $|W\rangle$ dephases into $N-1$ dark states which do not emit into the forward direction. These states are still excited to a Rydberg state, and therefore they are long-lived with a lifetime determined by the Raman decay rate Γ. We treat these dark states as a single dark state $|D\rangle$, and we describe the coupling from $|W\rangle$ to $|D\rangle$ as an irreversible decay with rate γ_D.

It is typically a goal in experiments in quantum physics to maximize coherence and minimize dephasing. This is for instance the case for the experiments described in chapter 4 and in previous publications [57, 143]. In contrast, the single photon subtractor suggested in Ref. [159] and realized here relies on the dephasing of a collective excitation shared between many emitters to a collective state which decays only slowly, and which is not coupled to the mode of interest of the system.

Therefore, we aim for maximizing the dephasing rate γ_D from $|W\rangle$ to $|D\rangle$. The dephasing is caused by many processes, such as atomic motion, stray fields across the atomic ensembles, varying trapping depth, and scattering of the Rydberg electron with ground state atoms [66, 171, 172].

The dominant source of dephasing becomes apparent from the definition of the bright collective state of N identical emitters, given by equation 2.21,

$$|W\rangle = \frac{1}{\sqrt{N}} \sum_{j=1}^{N} e^{i\vec{k}\cdot\vec{r}_j} |g_1 g_2 \cdots r_j \cdots g_N\rangle, \tag{5.1}$$

where r_j is the position of the jth atom and $\vec{k}$ is the wavevector of the spinwave in the system. As discussed previously, the phase factors containing this wavevector are essential for the enhanced coupling to the probe mode, and for the directional re-emission into this mode. The phase information of this state is lost with atomic motion, and the magnitude of the dephasing is determined by the length of $\vec{k}$. In our system, $\vec{k}$ is given by the sum of wave-vectors of the

probe and control fields as described in equation 3.2, and motional dephasing becomes maximal when the fields are copropagating.

In our theoretical description we treat these effects as homogeneous dephasing sources. As already discussed in section 3.3, we introduce them in the master equation as a single dephasing term γ_D. This simplified approach is considered reasonable as a consequence of the large number N of constituent atoms in each superatom, which leads to a large number of states orthogonal to the timed Dicke-state $|W\rangle$. Since the number of orthogonal states is large, it is very unlikely that the collective excitation will return and become in-phase with the driving field.

While we have seen in chapter 4 that this approximation is not valid in all situations, it is justified in this case where the dephasing processes are sped up in the copropagating probing scheme. Consequently, we neglect the coherent internal dynamics within the superatoms, which occur on a time-scale much slower than the dephasing.

In the following, we consider a chained system which iteratively takes the output pulse shape from one superatom and feeds it to the next superatom. In section 3.7 we discussed how this chained system would look in the case of interactions between the superatoms, and in particular we concluded that effects of such coupling vanish for large dephasing. Therefore, we neglect such interactions.

5.2 Preparation of cascaded single photon absorbers

Figure 5.1 shows the experimental setup used to realize multi-photon subtraction. The super-atoms are created as discussed in chapter 3.4, and the system allows up to three superatoms in series. We probe the multi-photon absorption with few-photon pulses and use field-ionization to ionize any remaining Rydberg excitations after the probing. The ions are detected as described in section 3.4.

For the experiments discussed here we use atomic ensembles with on the order of 10,000 atoms in the excitation volume. The exact number of atoms depends on the number of traps applied, as shown in figure 3.9. We carry out the experiments at a temperature of around 9 μK. To realize the actual superatoms, we couple the atoms to the $|r\rangle = |121S, J = 1/2, m_j = 1/2\rangle$-state with control Rabi frequency of $13 \times 2\pi$ MHz and Raman detuning $\Delta = 2\pi \times 100$ MHz.

In this section we discuss how we prepare the Rydberg superatoms to realize the setup sketched in figure 5.1. Most details are already covered in section 3.5. Here we focus on the different loading procedure applied to load different numbers of superatoms, and how we ensure that the superatoms are as identical as possible.

5.2.1 Superatom loading procedure

The dimple traps are loaded from atoms trapped in a crossed optical dipole trap, which also provides radial confinement for the atomic ensembles in the dimple traps. Hence, the geometry of the trap and the distribution of atoms in the dipole trap set a limit on the number of well separated dimple traps and thereby a limit on the number of superatoms. This follows from the simple fact that the superatoms need to be separated by distances $\gg r_B$, and that the filling of the dimple traps relies on the overlap with the optical dipole trap as discussed in the previous chapter.

We adapt a tailored loading procedure depending on the number of ensembles. The details are outlined in section 3.4. In the case of one or two atomic ensembles, we simply turn up the intensity of the dimple beams gradually. For three ensembles, we first ramp up the two
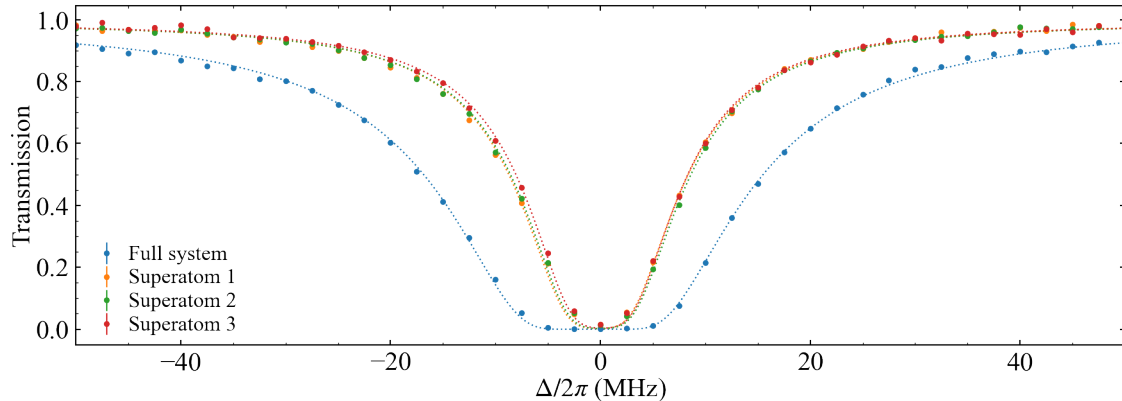
Figure 5.2: Probe transmission through three atomic ensembles across resonance in the absence of a control field. For the full system with three ensembles simultaneously, and with the three ensembles probed individually as discussed in the main text. Fitting the transmission and extracting the optical depth yields 20.1 for the entire system, and 6.1,5.2, and 5.6 for the individual ensembles respectively. The dashed lines show the fits. The error bars show one standard error of mean. Each data point is a result of on the order of 2000 measurements.

Number of absorbers	Optical depth	Transmission
3	20	0.9846
2	16	0.9867
1	11	0.9899

Table 5.1: Parameters different numbers of atomic ensembles. The optical depth on probe transmission and transmission at $\Delta = 2\pi \times 100\,\mathrm{MHz}$ in absence of control field scales as expected with the number of ensembles.

traps on the sides and then adjust the ramping time of the third trap in the middle to get similar atom numbers in each of the three ensembles. During a final step we turn off the crossed optical dipole trap to allow atoms trapped outside the dimples to escape. We then ramp up the dipole trap once more to provide radial confinement. Absorption images of the three ensembles are shown in figure 3.9.

5.2.2 Identical superatoms

To ensure that all three ensembles contain similar atom numbers, we adapt the trap intensities and positions to arrive at similar optical depth. Figure 5.2 shows the probe transmission for $n_{\mathrm{sub}} = 3$ as well as for the individual ensembles. To obtain values for the individual ensembles, we move the traps for two out of three ensembles aside and then turn them off as shown in figure 3.8. We optimize the loading procedure to get similar optical depth for the three individual ensembles.

The dimple trapping beams are kept on during probing as discussed in section 3.5.2, and give rise to a differential light shift. The intensity in each dimple trapping beam determines the shift experienced by each atomic ensemble, and thus the exact two-photon resonance frequency. To ensure that all three superatoms have the same resonance frequency, we employ Rydberg spectroscopy combined with site-resolved ion detection to determine the resonance frequency of each superatom as discussed in section 3.5.2 and shown in figure 5.3. The intensity changes
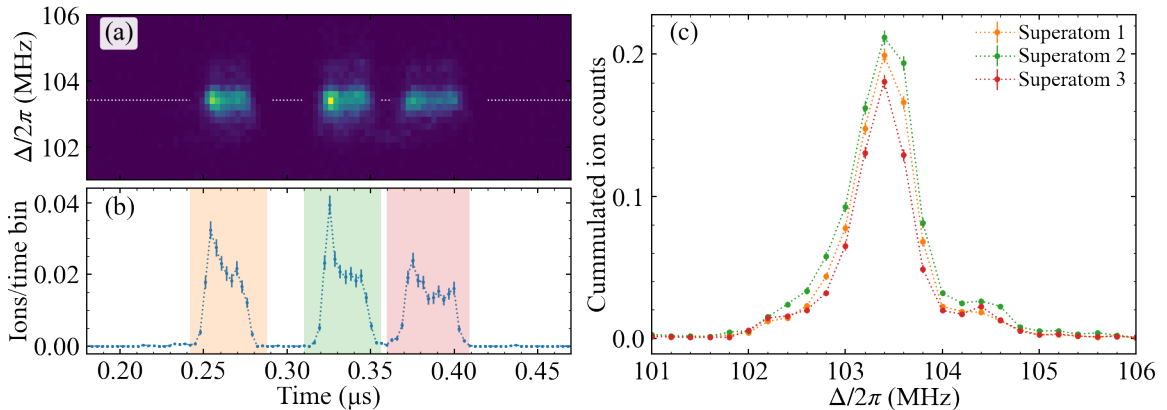
Figure 5.3: Detection time of ions at Rydberg resonance as in figure 3.10. a) shows the timing of ion detection as a function of the probe detuning. The x-axis shows the detection time. Each slice corresponds to a different detuning. b) shows the time trace for the slice of a) marked with a dotted line. The colored areas indicate the regions which are summed to give the ion count in each of the superatoms. The width of the peaks is due to fluctuations in detection time caused by temporal fluctuations in a high-voltage switch. c) ions from each of the three detection windows as a function of detuning. Error bars are standard error of mean.

that are required to tune the superatoms into resonance are so small that they do not affect the optical depth.

5.2.3 Residual probe absorption

While we work far-detuned from the probe transition with $\Delta = 2\pi \times 100\,\text{MHz}$, there is still a small amount of off-resonant scattering on the probe transition. Therefore, we measure the transmission through the ensembles at $\Delta = 2\pi \times 100\,\text{MHz}$ in absence of the control field. Table 5.1 shows the OD on probe resonance and transmission at $\Delta = 2\pi \times 100\,\text{MHz}$ for $n_{\text{sub}} = 1, 2, 3$ respectively. The data presented in the following sections have been corrected for this.

5.3 Multi-photon subtraction

With $n_{\text{sub}} = 1, 2,$ or 3 identical superatoms prepared as discussed above we can now investigate and characterize the absorption of individual photons by probing the chain of superatoms with few-photon probe pulses. We probe the n_{sub} ensembles with coherent Tukey-shaped few-photon pulses as defined in equation 3.19. We use pulses with up-time $t_{\text{up}} = 1.5\,\mu\text{s}$ and rise- and fall-time $t_{\text{rise}} = 1.0\,\mu\text{s}$. We vary the pulse amplitude, keeping < 40 photons per pulse. The few-photon pulses are detected as discussed in section 3.4.

Figure 5.4 shows the temporal transmission profile for selected input photon rates for $n_{\text{sub}} = 1, 2, 3$. As expected, the absorption increases for larger n_{sub}. The measured output profile shows how the superatoms go through different regimes as predicted by the theory: For low input photon numbers the superatom is barely excited, but for higher photon numbers the expected oscillatory dynamics set in.

For low input photon rates the missing photons are observed as relatively large changes to the pulse. The output pulses never rise to the same level as the input pulse, and even on the falling edge of the input pulse the absorbers are still absorbing photons. As the number
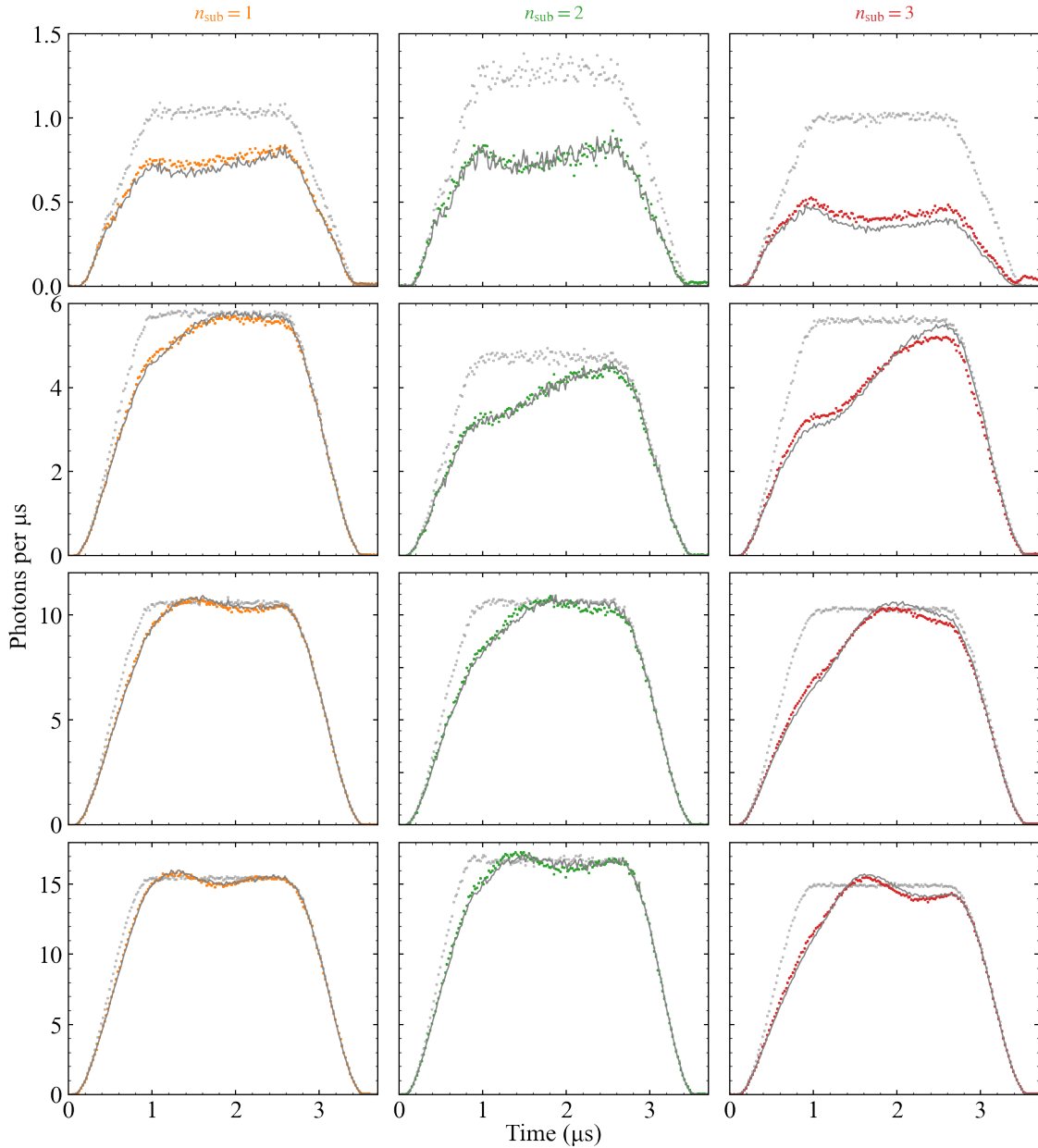
Figure 5.4: Probe pulse transmission for different n_{sub} and different incoming photon rate $\mathcal{R}_{\text{in}}$. Colored points show experimentally measured transmission through the superatoms, gray points show the reference pulses. Solid, gray lines show model predictions. The model predictions are calculated from the reference pulses.

of input photons increases, the absorption becomes relatively less prominent as expected due to the saturability of the absorbers. For $\mathcal{R}_{\text{in}} \approx 5$ we see a clear sign of saturation when the output pulse reaches the same level as the input pulse.

In the case of $\mathcal{R}_{\text{in}} \approx 10$ one clearly sees the coherent dynamics as stimulated emission. Absorbed photons which are subsequently reemitted into the forward mode do not contribute to the number of absorbed photons. Similarly, we observe a small after-pulse for low input rate for $n_{\text{sub}} = 3$. Though these photons have been redistributed within the pulse by the coherent

68

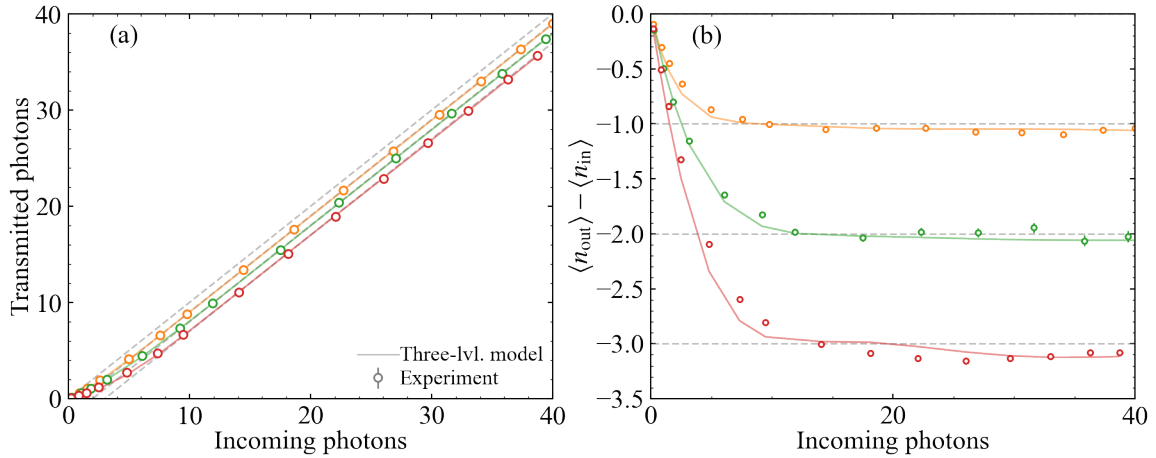Figure 5.5: Single photon subtraction from one, two or three superatoms. a) shows transmitted photons as a function of incoming photons. The expected slope shown as dashed grey lines show $\langle n \rangle_{\mathrm{in}} - 1, 2, 3$ respectively. The data have been corrected with the ground state scattering as discussed in the main text. b) shows the same data as a) but adjusted with input photons. This shows that for increasing n_{sub} the probability of absorbing too many photons increases. We also observe that some of the Rabi dynamics survive in the absorbed photons, indicating that the subtractors are not fully dephased.

dynamics, they are not lost from the forward mode of the system.

5.3.1 Subtraction performance

To obtain the number of absorbed photons, we compare the total photon number over the entire pulse length with and without absorbers in the path. Figure 5.5 a) shows the number of transmitted photons n_{out} as a function of input photon number n_{in} for $n_{\mathrm{sub}} = 1, 2, 3$. The dashed lines show the incoming number of photons minus one, two, and three photons respectively and are included as guides to the eye. These lines have been corrected for the residual absorption as discussed above. Figure 5.5 b) shows the difference $\langle n_{\mathrm{out}} \rangle - \langle n_{\mathrm{in}} \rangle$. As observed in figure 5.4 the full absorption of n_{sub} photons is not reached for very low input photon numbers. This is due to the fact that the pulse area $\sqrt{\kappa \mathcal{R}_{\mathrm{in}}} \tau < \pi$ is insufficient to fully drive the superatom to the excited state. As n_{sub} is increased, this effect becomes more prominent: While a single absorber works reliably from $n_{\mathrm{in}} \approx 5$ the $n_{\mathrm{sub}} = 3$ system requires $n_{\mathrm{in}} > 10$ for reliable absorption of three photons, since the second absorber will experience weaker driving than the first, and so on.

Figure 5.5 shows that subtraction of one, two, and three photons works reliably in the range between 10 and 40 input photons. For high input photon numbers, figure 5.5 b) shows that there is a small amount of excess absorption.

Based on the transmission profiles presented in figure 5.4 it is possible to apply the two-plus-one-level model introduced in section 3.3 to the data. Table 5.2 lists parameters yielding good agreement with both the profiles shown in figure 5.4 and the number of absorbed photons shown in figure 5.5. Comparing the parameters shown in table 5.2 to the parameters presented in table 4.2 of the previous chapter we clearly see the enhanced dephasing due to the copropagating probe- and control beams.

Number of absorbers	κ (μs^{-1})	Γ (μs^{-1})	γ_D (μs)
1	0.494	0.045	2.329
2	0.330	0.020	3.215
3	0.350	0.040	2.393

Table 5.2: Parameters yielding good model agreements with experimental data.

The excess absorption $\langle n_{\text{in}} \rangle - \langle n_{\text{out}} \rangle > n_{\text{sub}}$ that is observed for the experimental data in figure 5.5 is predicted by the model for Raman decay with rate $\Gamma > 0$, indicating that the presence of Raman decay affects the fidelity of the absorber.

5.3.2 Rydberg populations

Deterministic n_{sub} photon absorption implies that each superatom absorbs not only a single photon on average but exactly one photon every time. To verify that our superatoms do not absorb multiple photons at a time we consider the system Rydberg population after the end of the pulse. As discussed in chapter 3.4 and previously in this chapter, the experimental setup allows spatial resolved ion detection of Rydberg excitations for the individual superatoms.

Figure 5.6 a) shows the mean number of ions as a function of incoming photons for the datasets shown in figure 5.5. The figure also shows predicted Rydberg population predicted by the from the two-plus-one-level model with the parameters given in table 5.2 scaled with the detection efficiency for each ion detection window. The scaling is slightly different for the different windows.

Both model and experimental data show the predicted saturation of the Rydberg population at high photon numbers, indicating that only one excitation can be present at any time in each ensemble. The slight variation of the Rydberg population in the saturated regime can be explained by the timescale of dephasing relative to the superatom Rabi oscillation.

From the detected ions we calculate the Mandel Q-parameter. The Mandel Q-parameter quantifies how similar a given probability distribution is to a Poissonian [173]. It is defined as

$$Q = \frac{\langle n_{\text{ion}}^2 \rangle - \langle n_{\text{ion}} \rangle^2}{\langle n_{\text{ion}} \rangle} = \frac{\text{var}(n_{\text{ion}})}{\langle n_{\text{ion}} \rangle} - 1. \tag{5.2}$$

For a Poissonian distribution with $\langle n_{\text{ion}} \rangle = \text{var}(n_{\text{ion}})$, $Q = 0$. For a sub-Poissonian distribution, $Q < 0$. In the case of a perfect system where a single ion is detected in each experiment, $Q = -1$.

For a non-perfect experimental system it is necessary to take the detection efficiency and the ion production probability into account. For this purpose, the ion detection process can be described as the number of successes in a number of Bernoulli trials. Assuming that the probability of success is p, the mean number of successes for such trials is $\langle n_{\text{ion}} \rangle = p$, and the variance is given by $\text{var}(n_{\text{ion}}) = p(1-p)$. Therefore,

$$Q = \frac{p(1-p)}{p} - 1 = -p = -\langle n_{\text{ion}} \rangle. \tag{5.3}$$

Thus, if the detection efficiency η is finite, then $Q \leq -\eta$. In the experiments presented here, the ion-production probability and the detection efficiency depends on the superatom location and can be inferred from the saturation level seen in figure 5.6 a). Figure 5.6 b) shows Q calculated for both experimental data and the results of the model.
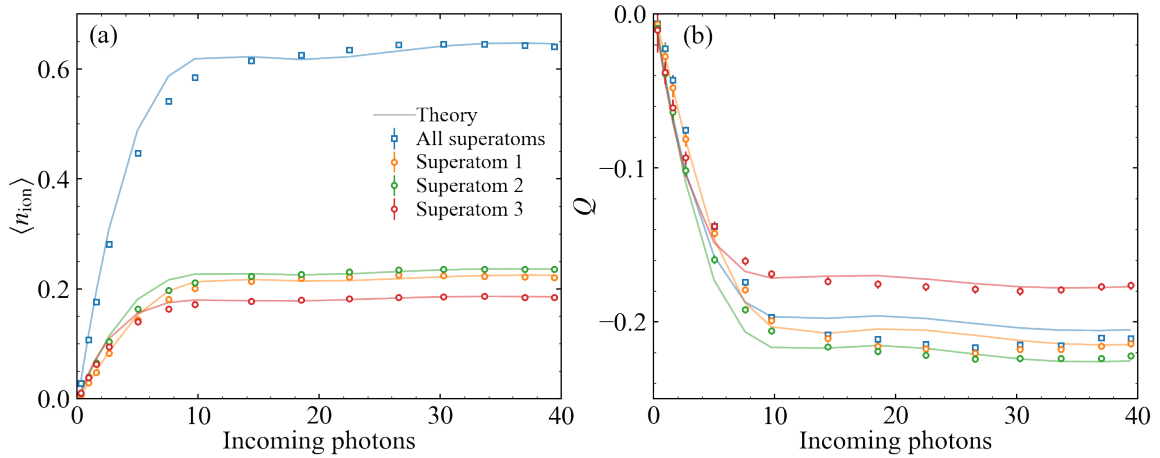
Figure 5.6: Ion statistics for $n_{\text{sub}} = 3$ compared with theoretical predictions from the model presented in section 3.3. The ion windows are also shown in figure 5.3. a) Mean number of ions from each of the three absorbers and the total mean ion count. The detection probability is lower for 'superatom 3', but this superatom is actually probed first, and thus it is expected to experience a higher number of photons. Consequently it rises faster than superatom 1, but saturates to a lower value. b) Calculated Mande Q-parameter for each of the three superatoms and the total system.

While the values $Q < 0$ indicate subpoissonian excitation statistics, double-excitations can only be ruled out by comparing Q to n_{ion} since $\eta < 1$. If the ion detection events follow a binomial distribution, which indicates that each absorber never produces more than a single excitation, we expect

$$\frac{Q}{\langle n_{\text{ion}} \rangle} = -\frac{\langle n_{\text{ion}} \rangle}{\langle n_{\text{ion}} \rangle} = -1. \tag{5.4}$$

Figure 5.7 shows $Q/\langle n_{\text{ion}} \rangle$ for the three individual absorbers for $n_{\text{sub}} = 3$. For low incoming photon numbers, dark counts dominate the signal and lead to $Q > -1$, but for larger values $Q/\langle n_{\text{ion}} \rangle$ is close to -1, the value that is expected for a binomial distribution. This show superatom saturation at a single excitation. The slight deviation observed as the number of incoming photons increases indicates that the superatoms occasionally contain more than a single Rydberg excitation.

Secondary Rydberg excitations can have different causes, such as incomplete blockade, antiblockade [174, 175], facilitated excitations [176], and cross detection of ions between the different ion windows.

To account for double Rydberg excitation in the model, we introduce a probability to create a second excitation, $p_2 \langle n_{\text{in}} \rangle$, which scales linearly with input photon rate. Further, we introduce a dark-count probability which is independent of input photons and is based on the ion dark counts measured in the experiments of $9\,\text{kHz}$. For the data shown in figures 5.5 and 5.6 we find good agreement with the experimental data for $p_2 = 3.5$, 6.5, and 5.0×10^{-4} for the first, second and third absorber in the $n_{\text{sub}} = 3$-system, respectively. The lower probability for a second excitation in the first superatom may be attributed to the fact that the ion detection window for this superatom is further separated in time than the other two, as seen in figure 5.7. This temporal separation makes cross detection less likely. Also, we need to introduce
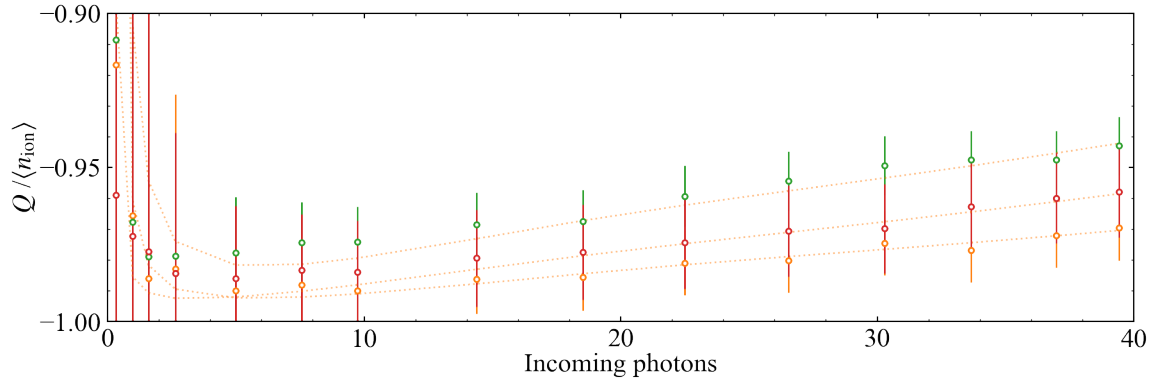
71

Figure 5.7: Q-over-mean for detected ions produced in a system of $n_{\text{sub}} = 3$ Rydberg super-atoms as a function of photons in the driving pulse. The colors correspond to the colors of figure 5.6. The dotted lines are predicted values.

five times as much noise for the second absorber as we would expect from the dark counts. We attribute this to the higher probability of detecting ions generated in the neighbouring absorbers within the ion window of this absorber.

5.3.3 Photon correlations

Finally, we show that the multi-photon absorber can be used to manipulate the quantum state of the light in the probe pulses. This was seen for a single Rydberg superatom in section 3.5.2.

For this purpose, we analyse the time-dependent intensity correlation function from the detection events on two detectors

$$g^{(2)}(t_1, t_2) = \frac{\langle n_1(t_1) n_2(t_2) \rangle}{\langle n_1(t_1) \rangle \langle n_2(t_2) \rangle}. \tag{5.5}$$

Figure 5.8 shows the measured correlation function for $n_{\text{sub}} = 3$ for two different $\mathcal{R}_{\text{in}}$ compared with corresponding model-predictions. For zero time-delay $t_1 = t_2$, the correlation function shows an initial anti-bunching feature where $g^{(2)}(t_2 - t_1 = 0) < 1$ and then photon bunching, $g^{(2)}(t_2 - t_1 = 0) > 1$.

The bunching and antibunching for zero time-delay stems from photon absorption and the coherent dynamics of the superatoms interacting with the probe pulse, which leads to a reordering of photons within the pulse.

The deviation from Poissonian photon statistics also highlights that the n_{sub}-photon sub-traction demonstrated here is fundamentally different from the application of the annihilation operator. The n_{sub}-photon subtraction reduces the mean number of photons in a coherent pulse by n_{sub} without changing the photon number uncertainty. In contrast, the annihilation operator does not affect the photon statistics of the coherent light pulse by definition as the coherent states are eigenstates of the annihilation operator.

5.4 Performance limitations

In the previous section we have demonstrated multi-photon subtraction realized with a chain of Rydberg superatoms. The subtraction works reliably for a wide range of input photon rates, but in figure 5.5 we have observed a small amount of excess absorption, which is primarily
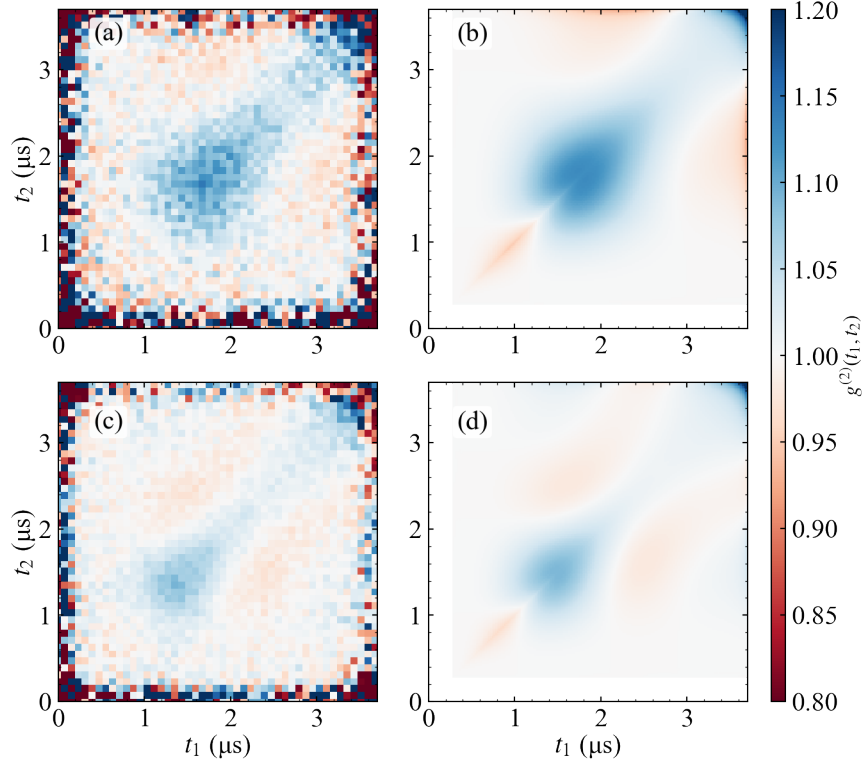
Figure 5.8: Photon correlation functions for $n_{\mathrm{sub}} = 3$ for two different photon rates. a) and b) show experimental results and theoretical prediction respectively for an input pulse of $\mathcal{R}_{\mathrm{in}} \simeq 5.5\,\mu\mathrm{s}^{-1}$. c) and d) show the same for $\mathcal{R}_{\mathrm{in}} \simeq 10\,\mu\mathrm{s}^{-1}$.

caused by spontaneous Raman decay determined with rate Γ. Though the time-scale of this decay is much slower than the other time scales of the system $0 < \Gamma < \kappa, \gamma_D$, even a small probability that the absorber returns to the ground state without reemission into the forward mode allows for subtraction of more than one photon by each absorber.

The consequence of Raman decay becomes even more apparent for longer pulse lengths. Figure 5.9 a) shows three examples of the input and output photon profiles for pulses with $t_{\mathrm{up}} = 3.0\,\mu\mathrm{s}$. Panel b) shows the number of subtracted photons, which clearly exceeds $n_{\mathrm{sub}} = 3$ for sufficiently many input photons.

In contrast, figure 5.10 a) and b) show data for short pulses with $t_{\mathrm{up}} = 0.5\,\mu\mathrm{s}$. Here the number of subtracted photons is lower than $n_{\mathrm{sub}} = 3$. In this case, the dephasing with rate γ_D of the system will not be fast enough to bring the bright state population into a dark state before the driving pulse is over. Therefore, there is a finite probability to reemit absorbed photons into the forward mode.

From these observations, we conclude that the multi-photon subtraction shown in figure 5.5 cannot be achieved for arbitrary pulse lengths, since the absorption mechanism relies on the characteristic time-scale of the dephasing relative to the other time-scales of the system. Hence, depending on the pulse length the system parameters must be adapted for best performance.

For a single absorber, the mean number of lost photons due to Raman decay is given by

$$\langle N_{\mathrm{Raman}}(t) \rangle = \Gamma \int_{t_0}^{t} \mathrm{d}t' P_{\mathrm{Ryd}}(t'), \tag{5.6}$$
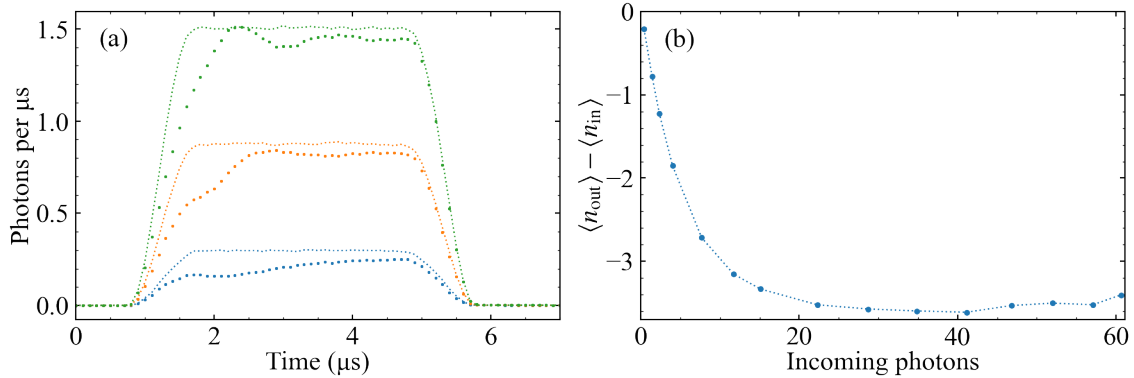
Figure 5.9: Photon subtraction in superatom chain with $n_{\text{sub}} = 3$ for driving pulses with $t_{\text{up}} = 3.0\,\mu\text{s}$. a) temporal transmission profile for three different input photon rates. Points show transmission, and dashed lines show driving field. b) photon subtraction. Points show data, and connecting lines serve as a guide for the eye. Standard error of mean error bars are too small to resolve.

where P_{Ryd} is the probability of finding the system in a Rydberg state. Figure 5.11 a) shows the sum of Rydberg population in $|W\rangle$ and $|D\rangle$ and $\langle N_{\text{Raman}}(t)\rangle$, which reflects the number of absorbed photons, for $\Gamma = 0, 0.004$, and $0.04\,\mu\text{s}^{-1}$ for a single absorber under constant driving. The shaded areas show one standard deviation $\sqrt{\text{Var}(N_{\text{Raman}}(t))}$. We calculate the standard deviation by considering an additional, virtual spin chain, which is populated via Raman decay. This approach allows us to count the number of lost photons. While the mean number of subtracted photons only deviates slightly with Γ, the standard deviation increases with both time and Γ. The increasing standard deviation highlights how the system starts to deviate from deterministic behavior and reverts to a classical attenuator.

Even for $\Gamma = 0$, the subtractor works best in a specific range of parameters if the time-scales of pulse length, κ, and γ_D are matched. Figure 5.11 b) shows the population in $|D\rangle$ for a superatom with $\Gamma = 0$ and $\kappa = 0.35\,\mu\text{s}^{-1}$ driven for $3\,\mu\text{s}$ as a function of γ_D and R_{in}. A large regime exists where the system is almost fully in $|D\rangle$, which is bounded by different processes: The photon rate $\sqrt{\kappa R_{\text{in}}}$ needs to be sufficient to ensure excitation from $|G\rangle$ to $|W\rangle$. Furthermore, the dephasing γ_D needs to be sufficiently high to ensure transfer from $|W\rangle$ to $|D\rangle$ within the length of the pulse. It is thus required that both $\sqrt{\kappa R_{\text{in}}}\tau$ and $\gamma_D\tau \gg 1$.

Finally, when γ_D becomes too large, the system enters an overdamped regime: As γ_D increases, the probability to excite the superatom within the time set by the pulse length is reduced. This is due to the presence of a strong decay channel to $|D\rangle$, which effectively corresponds to adiabatic elimination of $|W\rangle$. This is seen in figure 3.5. This again sets a γ_D-dependent lower limit for R_{in}.

A further limitation on the pulse lengths and incoming photon rate is the probability that a second photon is absorbed due to breakdown of the Rydberg blockade. This is relevant for short pulses and strong driving fields, which give rise to Fourier and power broadening respectively.

5.4.1 Scaling to many absorbers

After considering the limitations of a single absorber, we finally consider how the limitations, i.e. Raman decay, affect the scalability to many absorbers. In figure 5.12 we show the total
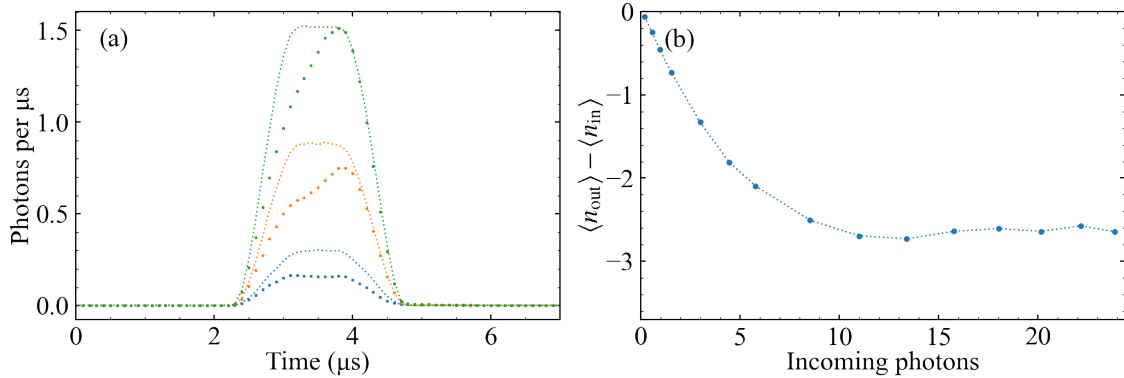
Figure 5.10: Photon subtraction in superatom chain with $n_{\mathrm{sub}} = 3$ for driving pulses with $t_{\mathrm{up}} = 1.5\,\mu\mathrm{s}$. a) temporal transmission profile for three different input photon rates. Points show transmission, and dashed lines show driving field. b) photon subtraction. Points show data, and connecting lines serve as a guide for the eye. Standard error of mean error bars are too small to resolve.

dark state population for a chain of up to $n_{\mathrm{sub}} = 8$ absorbers as a function of γ_D. We compare the performance for $\Gamma = 0$ to the case of a weak Raman decay, $\Gamma = 0.04\,\mu\mathrm{s}^{-1}$. As n_{sub} increases, the probability of finding the system with all absorbers in the dark state decreases. Even for $\Gamma = 0$, a chain of $n_{\mathrm{sub}} = 8$ will not reach perfect absorption any γ_D for the pulse used here, because the driving of the later absorbers becomes too weak. For finite Γ the chain is even further away from full saturation. This is not to be confused with too little absorption of photons. As we have seen in figure 5.11, presence of Raman decay leads to excess absorption, which is reflected in the lack of saturation.

The fundamental limitations discussed above are not unique to our scheme based on Rydberg superatoms [177]. For example, the finite lifetime of the excited state will affect any scheme which relies on excitation storage in an uncoupled excited state and any scheme involving coherent absorption will require a minimum driving strength.

In addition to the limitations discussed above, there are also technical limitations. First of all, the amount of photons scattered on the probe transition increases with the number of absorbers and the resulting increase in overall optical depth as seen in table 5.1. This can be limited by increasing Δ but cannot be fully suppressed.

The geometry of the setup also imposes limitations. It is a crucial prerequisite that the spot size of the probe beam is smaller than the range of the Rydberg blockade. In the current implementation, the probe beam is focused to a $1/e^2$-waist radius $6.5\,\mu\mathrm{m}$, yielding a Rayleigh-length of $150\,\mu\mathrm{m}$. This limits the length over which absorbers can be placed.

Additionally, this length is also limited by the crossing region of the crossed optical dipole trap which is required for radial confinement of the atoms in the dimple traps. This limitation can however be overcome relatively easily by adding an optical trapping beam along the probe axis.

In this chapter we have demonstrated how a system of up to three cascaded superatoms can be applied to manipulate pulses of light photon by photon via subtraction of exact photon numbers. The system discussed here could for instance also be employed for number resolved photon detection. This would require $n_{\mathrm{sub}} \gg$ the mean number of photons in the pulses of interest, such that all photons are absorbed and can be read out. In the current setup, the detection of the absorber states through field ionization is a limiting factor due to the finite
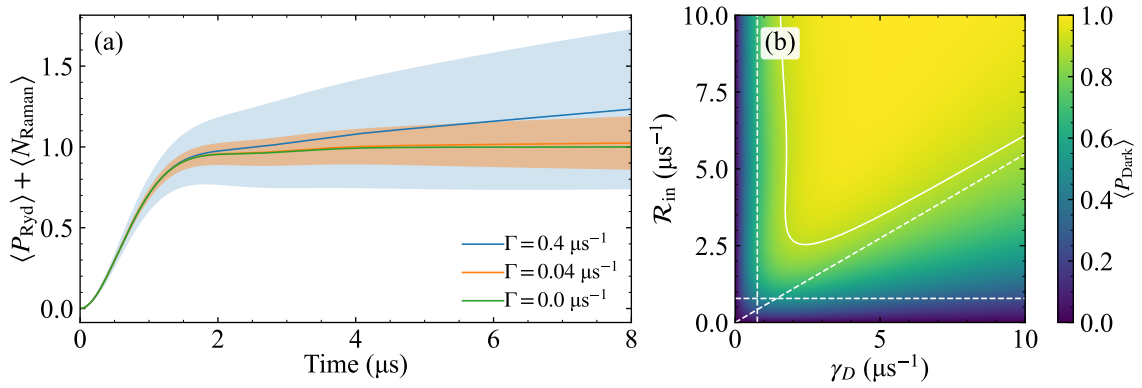
Figure 5.11: Theoretical analysis of superatom performance. a) Rydberg population plus lost photons from inclusion of Raman Decay Γ. Shaded area shows uncertainty in number of lost photons. Calculated for $\gamma_D = 2.4\,\mu s^{-1}$ and $\mathcal{R}_{in} = 5\,\mu s^{-1}$. b) Dark state population depending on γ_D and $\mathcal{R}_{in}$. Dashed lines show different bounds on absorption: $\sqrt{\kappa \mathcal{R}_{in}\tau} = \pi/2$, $\exp(-\gamma_D\tau) = 0.1$, and $\exp(-4\kappa\mathcal{R}_{in}\tau/\gamma_D)$. Solid line shows the 90 % contour.

Figure 5.12: The dark state population for $n_{sub} = 1, 2, 4$, and 8 for $\mathcal{R}_{in} = 5\,\mu s^{-1}$ and pulse of length of $4\,\mu s$. Solid lines show the dark state population for $\Gamma = 0$, and dashed lines are for $\Gamma = 0.04\,\mu s^{-1}$.

ion detection efficiency of $\approx 20\%$. This could be improved by chosing a different detection scheme, for example optical detection [178–180].

Chapter 6

Conclusion and outlook

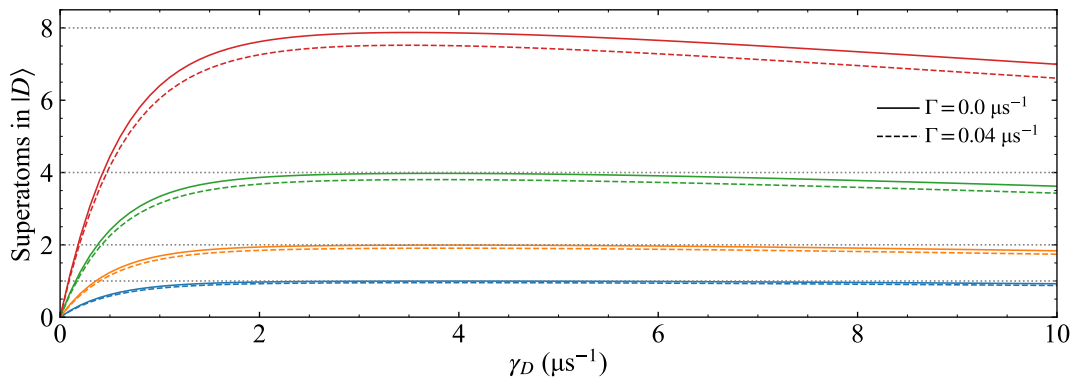In the previous chapters, we have discussed the concept of a Rydberg superatom: A small ensemble of ultracold atoms coupled to a Rydberg state. The atoms are addressed on a Raman transition, and due to the Rydberg blockade effect the entire ensemble is limited to a single excitation. Therefore, the superatom effectively acts in most aspects as a two-level emitter. Due to the collective nature of the Rydberg excitation the superatom couples strongly to driving fields, and because of the phase information imprinted by this field in the excitation, the superatom primarily emits spontaneously back into the exciting mode.

This thesis is an extension of previous work [57, 78, 143], which focused on the interaction of a single Rydberg superatom with a probe field. Due to the directionality of superatom emission, the superatom is a promising candidate to realize one-dimensional cascaded quantum systems.

However, the excited state of the superatom, which forms the upper state of the idealized two-level system, is only one of many possible singly excited collectively states. In this work we have explored the couplings within this set of states with a single collective excitation, and in particular excitation transfer between different collective states. We investigated this transfer experimentally through the emission into the forward mode after driving the superatom with pulses of varying duration to prepare different internal superatom states.

For the rate of the emission, we observed an oscillation depending on pulse length, which we attribute to coherent coupling between the different internal states of the atoms. The ability to observe and quantify the emission of less than a single photon per pulse is a result of the strong directionality of superatom emission.

As a first realization of a cascaded quantum system of Rydberg superatoms we have realized a saturable multi-photon subtractor building on the previous realization of single photon subtraction with a single Rydberg superatom [78]. We demonstrated multi-photon subtraction by sending coherent few-photon pulses through a chain of one, two, or three Rydberg superatoms and have observed how the subtraction leads to a modification of the quantum state of the light pulses. We analyzed the limitations of the subtraction protocol, also in the context of scalability to $n_{\mathrm{sub}} > 3$ and concluded that the fidelity is primarily limited by the limited excited state lifetime due to Raman decay, which causes excess loss of photons.

6.1   Future Perspectives

To demonstrate multi-photon subtraction, we have used rapid dephasing of the superatom bright state into excited but nonradiating collective states as a mean to remove single photons
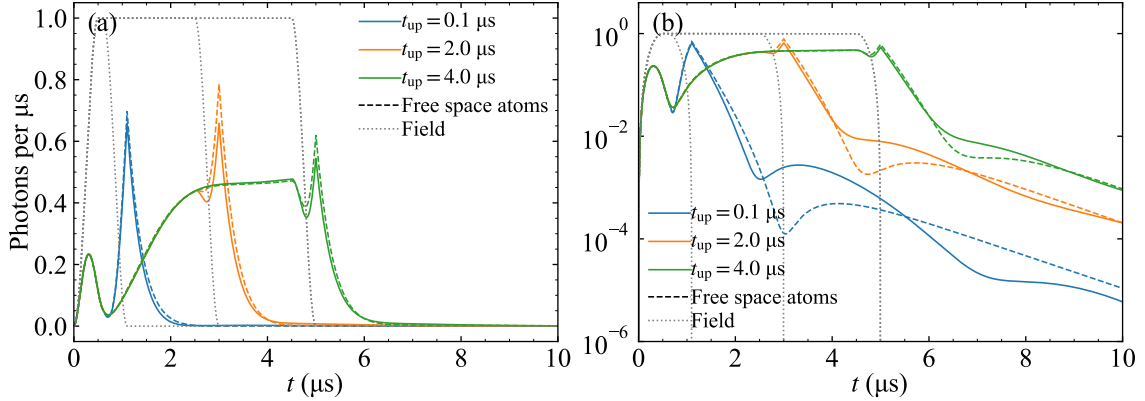
Figure 6.1: The calculated transmission of a probe field through and emission from a system of three (3) chained Rydberg superatoms coupled to a chiral waveguide. The superatoms are modelled with internal coherent dynamics for parameters $\kappa = 10.3\,\mu\mathrm{s}^{-1}$, and $\gamma_D = \Gamma = \varkappa = 0.3\,\mu\mathrm{s}^{-1}$. The driving field has photon rate $\mathcal{R}_{\mathrm{in}} = 1\,\mu\mathrm{s}^{-1}$. The solid lines show the response from the waveguide-coupled superatoms, while the dashed lines show the same calculated for superatoms in free space. a) and b) show the transmission in a linear and a logarithmic scale respectively.

from a probe pulse. However, in order to observe interactions between superatoms mediated by the directional photon exchange along the probe mode dephasing must be minimized. This is anlogue to the interaction between emitters coupled to a chiral waveguide as discussed in section 3.7. Our analysis in section 3.7 concluded that it can be a challenge to distinguish effects that result from photon exchange between the superatoms and coherent exchange interactions within the individual superatoms as observed in chapter 4.

To observe and quantify the effect of interactions between superatoms, the coupling and decay rates of the individual superatoms must be optimized such that the coupling to the probe mode is the dominant contribution to the system dynamics.

This could be achieved by increasing the number of atoms in each superatom or increasing the control Rabi frequency. Both approaches have their limitations, however, since increasing the atom number and density may cause additional dephasing through inhomogeneous broadening [134], while an increased control Rabi frequency leads to an increase in Raman decay rate as seen in equation 3.3.

The ratio of the coherent coupling relative to dephasing rate can also be improved by introducing a magic wavelength lattice trap that limits atomic motion along the probe mode [181]. The introduction of a magic wavelength trap would lead to a faster single atom decay due to the admixture of additional decay channels. However, in the current setup, where $\gamma_D \simeq 15\Gamma$, we would still expect a significant overall improvement. The implementation of such a trap is currently underway.

Other ways of improving the coupling-to-dephasing ratio would be to cool the atoms to lower temperatures or to use a different atomic species with a smaller difference in probe and control wavelength, such as ytterbium with 399 and 395 nm respectively.

Figure 6.1 revisits the simulations presented in section 3.7 for three superatoms with improved parameters, i.e. $\kappa = 1\,\mu\mathrm{s}^{-1}$, and $\gamma_D = \Gamma = \varkappa = 0.3\,\mu\mathrm{s}^{-1}$, and compares the probe light transmission and emission with and without coupling along the waveguide.

On the logarithmic plot in panel b), we observe that the waveguide-mediated superatom-

superatom coupling alters the timescale of the non-exponential decay. This implies that in an ideal system with point-like superatoms and κ defining the dominant time-scale of the system, signatures of the waveguide-mediated interaction should be observable.

The experiments discussed here differ from other waveguide-coupled emitters since the superatoms enable directional coupling in a single optical mode purely based on their collective nature, without a physical waveguide. Moreover, constituent atoms are not coupled to this superatom-defined waveguide. One can also consider systems where the superatoms are coupled to a physical waveguide [105], such as an integrated optical waveguide on a chip, or a tapered optical nano-fiber. The prospect of mediating interactions between Rydberg superatoms through optical photons falls in line with recent efforts into using collectively encoded Rydberg qubits for quantum simulations and information processing [62, 182–185].

Bibliography

[1]   T. H. Maiman. "Stimulated Optical Radiation in Ruby". *Nature* 187 (1960), pp. 493–494.

[2]   E. L. Raab, M. Prentiss, Alex Cable, Steven Chu, and D. E. Pritchard. "Trapping of Neutral Sodium Atoms with Radiation Pressure". *Phys. Rev. Lett.* 59 (1987), pp. 2631–2634.

[3]   Steven Chu, J. E. Bjorkholm, A. Ashkin, and A. Cable. "Experimental Observation of Optically Trapped Atoms". *Phys. Rev. Lett.* 57 (1986), pp. 314–317.

[4]   M. H. Anderson, J. R. Ensher, M. R. Matthews, C. E. Wieman, and E. A. Cornell. "Observation of Bose-Einstein Condensation in a Dilute Atomic Vapor". *Science* 269 (1995), pp. 198–201.

[5]   K. B. Davis, M. -O. Mewes, M. R. Andrews, N. J. van Druten, D. S. Durfee, D. M. Kurn, and W. Ketterle. "Bose-Einstein Condensation in a Gas of Sodium Atoms". *Phys. Rev. Lett.* 75 (1995), pp. 3969–3973.

[6]   D. Frese, B. Ueberholz, S. Kuhr, W. Alt, D. Schrader, V. Gomer, and D. Meschede. "Single Atoms in an Optical Dipole Trap: Towards a Deterministic Source of Cold Atoms". *Phys. Rev. Lett.* 85 (2000), pp. 3777–3780.

[7]   Nicolas Schlosser, Georges Reymond, Igor Protsenko, and Philippe Grangier. "Sub-poissonian loading of single atoms in a microscopic dipole trap". *Nature* 411 (2001), pp. 1024–1027.

[8]   W. Guerin, M.T. Rouabah, and R. Kaiser. "Light interacting with atomic ensembles: collective, cooperative and mesoscopic effects". *J. Mod. Opt.* 64 (2016), pp. 895–907.

[9]   Robert H Dicke. "Coherence in spontaneous radiation processes". *Phys. Rev.* 93 (1954), p. 99.

[10] N. Skribanowitz, I. P. Herman, J. C. MacGillivray, and M. S. Feld. "Observation of Dicke Superradiance in Optically Pumped HF Gas". *Phys. Rev. Lett.* 30 (1973), pp. 309–312.

[11] Anatolii V Andreev, Vladimir I Emel'yanov, and Yu A Il'inskiĭ. "Collective spontaneous emission (Dicke superradiance)". *Sov. Phys. Uspekhi* 23 (1980), pp. 493–514.

[12] Michel Gross and Serge Haroche. "Superradiance: An essay on the theory of collective spontaneous emission". *Phys. Rep.* 93 (1982), pp. 301–396.

[13] D. Pavolini, A. Crubellier, P. Pillet, L. Cabaret, and S. Liberman. "Experimental Evidence for Subradiance". *Phys. Rev. Lett.* 54 (1985), pp. 1917–1920.

[14] RG DeVoe and RG Brewer. "Observation of superradiant and subradiant spontaneous emission of two trapped ions". *Phys. Rev. Lett.* 76 (1996), p. 2049.

[15] Tom Bienaimé, Nicola Piovella, and Robin Kaiser. "Controlled Dicke Subradiance from a Large Cloud of Two-Level Systems". *Phys. Rev. Lett.* 108 (2012), p. 123602.

[16] William Guerin, Michelle O. Araújo, and Robin Kaiser. "Subradiance in a Large Cloud of Cold Atoms". *Phys. Rev. Lett.* 116 (2016), p. 083601.

[17] J. Pellegrino, R. Bourgain, S. Jennewein, Y. R. P. Sortais, A. Browaeys, S. D. Jenkins, and J. Ruostekoski. "Observation of Suppression of Light Scattering Induced by Dipole-Dipole Interactions in a Cold-Atom Ensemble". *Phys. Rev. Lett.* 113 (2014), p. 133602.

[18] S. D. Jenkins, J. Ruostekoski, J. Javanainen, S. Jennewein, R. Bourgain, J. Pellegrino, Y. R. P. Sortais, and A. Browaeys. "Collective resonance fluorescence in small and dense atom clouds: Comparison between theory and experiment". *Phys. Rev. A* 94 (2016), p. 023842.

[19] Stephan Jennewein, Ludovic Brossard, Yvan R. P. Sortais, Antoine Browaeys, Patrick Cheinet, Jacques Robert, and Pierre Pillet. "Coherent scattering of near-resonant light by a dense, microscopic cloud of cold two-level atoms: Experiment versus theory". *Phys. Rev. A* 97 (2018), p. 053816.

[20] Antoine Glicenstein, Giovanni Ferioli, Nikola Šibali ć, Ludovic Brossard, Igor Ferrier-Barbut, and Antoine Browaeys. "Collective Shift in Resonant Light Scattering by a One-Dimensional Atomic Chain". *Phys. Rev. Lett.* 124 (2020), p. 253602.

[21] C. Hettich, C. Schmitt, J. Zitzmann, S. Kühn, I. Gerhardt, and V. Sandoghdar. "Nanometer Resolution and Coherent Optical Dipole Coupling of Two Individual Molecules". *Science* 298 (2002), pp. 385–389.

[22] B. H. McGuyer, M. McDonald, G. Z. Iwata, M. G. Tarallo, W. Skomorowski, R. Moszynski, and T. Zelevinsky. "Precise study of asymptotic physics with subradiant ultracold molecules". *Nat. Phys.* 11 (2014), pp. 32–36.

[23] J. Keaveney, A. Sargsyan, U. Krohn, I. G. Hughes, D. Sarkisyan, and C. S. Adams. "Cooperative Lamb Shift in an Atomic Vapor Layer of Nanometer Thickness". *Phys. Rev. Lett.* 108 (2012), p. 173601.

[24] T. Peyrot, Y. R. P. Sortais, A. Browaeys, A. Sargsyan, D. Sarkisyan, J. Keaveney, I. G. Hughes, and C. S. Adams. "Collective Lamb Shift of a Nanoscale Atomic Vapor Layer within a Sapphire Cavity". *Phys. Rev. Lett.* 120 (2018), p. 243401.

[25] S. L. Bromley, B. Zhu, M. Bishof, X. Zhang, T. Bothwell, J. Schachenmayer, T. L. Nicholson, R. Kaiser, S. F. Yelin, M. D. Lukin, A. M. Rey, and J. Ye. "Collective atomic scattering and motional effects in a dense coherent medium". *Nat. Commun.* 7 (2016).

[26] Ralf Röhlsberger, Kai Schlage, Balaram Sahoo, Sebastien Couet, and Rudolf Rüffer. "Collective Lamb Shift in Single-Photon Superradiance". *Science* 328 (2010), pp. 1248–1251.

[27] Z. Meir, O. Schwartz, E. Shahmoon, D. Oron, and R. Ozeri. "Cooperative Lamb Shift in a Mesoscopic Atomic Array". *Phys. Rev. Lett.* 113 (2014), p. 193002.

[28] Daniel Barredo, Sylvain de Léséleuc, Vincent Lienhard, Thierry Lahaye, and Antoine Browaeys. "An atom-by-atom assembler of defect-free arbitrary two-dimensional atomic arrays". *Science* 354 (2016), pp. 1021–1023.

[29] Manuel Endres, Hannes Bernien, Alexander Keesling, Harry Levine, Eric R. Anschuetz, Alexandre Krajenbrink, Crystal Senko, Vladan Vuletic, Markus Greiner, and Mikhail D. Lukin. "Atom-by-atom assembly of defect-free one-dimensional cold atom arrays". *Science* 354 (2016), pp. 1024–1027.

[30] Waseem S. Bakr, Jonathon I. Gillen, Amy Peng, Simon Fölling, and Markus Greiner. "A quantum gas microscope for detecting single atoms in a Hubbard-regime optical lattice". *Nature* 462 (2009), pp. 74–77.

[31] Jacob F. Sherson, Christof Weitenberg, Manuel Endres, Marc Cheneau, Immanuel Bloch, and Stefan Kuhr. "Single-atom-resolved fluorescence imaging of an atomic Mott insulator". *Nature* 467 (2010), pp. 68–72.

[32] Robert J. Bettles, Simon A. Gardiner, and Charles S. Adams. "Enhanced Optical Cross Section via Collective Coupling of Atomic Dipoles in a 2D Array". *Phys. Rev. Lett.* 116 (2016), p. 103602.

[33] H. H. Jen, M.-S. Chang, and Y.-C. Chen. "Cooperative single-photon subradiant states". *Phys. Rev. A* 94 (2016), p. 013803.

[34] Ephraim Shahmoon, Dominik S. Wild, Mikhail D. Lukin, and Susanne F. Yelin. "Cooperative Resonances in Light Scattering from Two-Dimensional Atomic Arrays". *Phys. Rev. Lett.* 118 (2017), p. 113601.

[35] Dominik S. Wild, Ephraim Shahmoon, Susanne F. Yelin, and Mikhail D. Lukin. "Quantum Nonlinear Optics in Atomically Thin Materials". *Phys. Rev. Lett.* 121 (2018), p. 123606.

[36] R. Bekenstein, I. Pikovski, H. Pichler, E. Shahmoon, S. F. Yelin, and M. D. Lukin. "Quantum metasurfaces with atom arrays". *Nat. Phys.* 16 (2020), pp. 676–681.

[37] A. Asenjo-Garcia, M. Moreno-Cardoner, A. Albrecht, H. J. Kimble, and D. E. Chang. "Exponential Improvement in Photon Storage Fidelities Using Subradiance and "Selective Radiance" in Atomic Arrays". *Phys. Rev. X* 7 (2017), p. 031024.

[38] M T Manzoni, M Moreno-Cardoner, A Asenjo-Garcia, J V Porto, A V Gorshkov, and D E Chang. "Optimization of photon storage fidelity in ordered atomic arrays". *New J. Phys.* 20 (2018), p. 083048.

[39] Jun Rui, David Wei, Antonio Rubio-Abadal, Simon Hollerith, Johannes Zeiher, Dan M. Stamper-Kurn, Christian Gross, and Immanuel Bloch. "A subradiant optical mirror formed by a single structured atomic layer". *Nature* 583 (2020), pp. 369–374.

[40] H. J. Kimble. "Strong Interactions of Single Atoms and Photons in Cavity QED". *Physica Scripta* T76 (1998), p. 127.

[41] Andreas Reiserer and Gerhard Rempe. "Cavity-based quantum networks with single atoms and optical photons". *Rev. Mod. Phys.* 87 (2015), pp. 1379–1418.

[42] Peter Lodahl, Sahand Mahmoodian, Søren Stobbe, Arno Rauschenbeutel, Philipp Schneeweiss, Jürgen Volz, Hannes Pichler, and Peter Zoller. "Chiral quantum optics". *Nature* 541 (2017), pp. 473–480.

[43] Rafael A. de Oliveira, Milrian S. Mendes, Weliton S. Martins, Pablo L. Saldanha, José W. R. Tabosa, and Daniel Felinto. "Single-photon superradiance in cold atoms". *Phys. Rev. A* 90 (2014), p. 023848.

[44] D. E. Chang, V. Gritsev, G. Morigi, V. Vuletić, M. D. Lukin, and E. A. Demler. "Crystallization of strongly interacting photons in a nonlinear optical fibre". *Nat. Phys.* 4 (2008), pp. 884–889.

[45] A. Goban, C.-L. Hung, J. D. Hood, S.-P. Yu, J. A. Muniz, O. Painter, and H. J. Kimble. "Superradiance for Atoms Trapped along a Photonic Crystal Waveguide". *Phys. Rev. Lett.* 115 (2015), p. 063601.

[46] P. Solano, P. Barberis-Blostein, F. K. Fatemi, L. A. Orozco, and S. L. Rolston. "Super-radiance reveals infinite-range dipole interactions through a nanofiber". *Nat. Commun.* 8 (2017), p. 1857.

[47] Neil V. Corzo, Jérémy Raskop, Aveek Chandra, Alexandra S. Sheremet, Baptiste Gouraud, and Julien Laurat. "Waveguide-coupled single collective excitation of atomic arrays". *Nature* 566 (2019), pp. 359–362.

[48] Adarsh S. Prasad, Jakob Hinney, Sahand Mahmoodian, Klemens Hammerer, Samuel Rind, Philipp Schneeweiss, Anders S. Sørensen, Jürgen Volz, and Arno Rauschenbeutel. "Correlating photons using the collective nonlinear response of atoms weakly coupled to an optical mode". *Nat. Photon.* 14 (2020), pp. 719–722.

[49] Riccardo Pennetta, Daniel Lechner, Martin Blaha, Arno Rauschenbeutel, Philipp Schneeweiss, and Jürgen Volz. *Observation of coherent coupling between super- and subradiant states of an ensemble of cold atoms collectively coupled to a single propagating optical mode.* 2021. arXiv: 2112.10806 [quant-ph].

[50] P. Y. Wen, K.-T. Lin, A. F. Kockum, B. Suri, H. Ian, J. C. Chen, S. Y. Mao, C. C. Chiu, P. Delsing, F. Nori, G.-D. Lin, and I.-C. Hoi. "Large Collective Lamb Shift of Two Distant Superconducting Artificial Atoms". *Phys. Rev. Lett.* 123 (2019), p. 233602.

[51] Shoichi Okaba, Deshui Yu, Luca Vincetti, Fetah Benabid, and Hidetoshi Katori. "Superradiance from lattice-confined atoms inside hollow core fibre". *Commun. Phys.* 2 (2019), p. 136.

[52] J. A. Mlynek, A. A. Abdumalikov, J. M. Fink, L. Steffen, M. Baur, C. Lang, A. F. van Loo, and A. Wallraff. "Demonstrating *W*-type entanglement of Dicke states in resonant cavity quantum electrodynamics". *Phys. Rev. A* 86 (2012), p. 053838.

[53] Arjan F. van Loo, Arkady Fedorov, Kevin Lalumière, Barry C. Sanders, Alexandre Blais, and Andreas Wallraff. "Photon-Mediated Interactions Between Distant Artificial Atoms". *Science* 342 (2013), pp. 1494–1496.

[54] Carlo Bradac, Mattias T. Johnsson, Matthew van Breugel, Ben Q. Baragiola, Rochelle Martin, Mathieu L. Juan, Gavin K. Brennen, and Thomas Volz. "Room-temperature spontaneous superradiance from single diamond nanocrystals". *Nat. Commun.* 8 (2017), p. 1205.

[55] Andreas Angerer, Kirill Streltsov, Thomas Astner, Stefan Putz, Hitoshi Sumiya, Shinobu Onoda, Junichi Isoya, William J. Munro, Kae Nemoto, Jörg Schmiedmayer, and Johannes Majer. "Superradiant emission from colour centres in diamond". *Nat. Phys.* 14 (2018), pp. 1168–1172.

[56] Kankan Cong, Qi Zhang, Yongrui Wang, G. Timothy Noe, Alexey Belyanin, and Junichiro Kono. "Dicke superradiance in solids [Invited]". *J. Opt. Soc. Am. B* 33 (2016), p. C80.

[57] Asaf Paris-Mandoki, Christoph Braun, Jan Kumlin, Christoph Tresp, Ivan Mirgorodskiy, Florian Christaller, Hans Peter Büchler, and Sebastian Hofferberth. "Free-Space Quantum Electrodynamics with a Single Rydberg Superatom". *Phys. Rev. X* 7 (2017), p. 041010.

[58] M. D. Lukin, M. Fleischhauer, R. Cote, L. M. Duan, D. Jaksch, J. I. Cirac, and P. Zoller. "Dipole Blockade and Quantum Information Processing in Mesoscopic Atomic Ensembles". *Phys. Rev. Lett.* 87 (2001), p. 037901.

[59] M. Saffman, T. G. Walker, and K. Mølmer. "Quantum information with Rydberg atoms". *Rev. Mod. Phys.* 82 (2010), pp. 2313–2363.

[60] Y. O. Dudin, L. Li, F. Bariani, and A. Kuzmich. "Observation of coherent many-body Rabi oscillations". *Nat. Phys.* 8 (2012), pp. 790–794.

[61] T. M. Weber, M. Höning, T. Niederprüm, T. Manthey, O. Thomas, V. Guarrera, M. Fleischhauer, G. Barontini, and H. Ott. "Mesoscopic Rydberg-blockaded ensembles in the superatom regime and beyond". *Nat. Phys.* 11 (2015), pp. 157–161.

[62] M. Ebert, M. Kwon, T. G. Walker, and M. Saffman. "Coherence and Rydberg Blockade of Atomic Ensemble Qubits". *Phys. Rev. Lett.* 115 (2015), p. 093601.

[63] Johannes Zeiher, Peter Schauß, Sebastian Hild, Tommaso Macrì, Immanuel Bloch, and Christian Gross. "Microscopic Characterization of Scalable Coherent Rydberg Superatoms". *Phys. Rev. X* 5 (2015), p. 031015.

[64] J. D. Pritchard, D. Maxwell, A. Gauguet, K. J. Weatherill, M. P. A. Jones, and C. S. Adams. "Cooperative Atom-Light Interaction in a Blockaded Rydberg Ensemble". *Phys. Rev. Lett.* 105 (2010), p. 193603.

[65] O Firstenberg, C S Adams, and S Hofferberth. "Nonlinear quantum optics mediated by Rydberg interactions". *Journal of Physics B: Atomic, Molecular and Optical Physics* 49 (2016), p. 152003.

[66] Y. O. Dudin and A. Kuzmich. "Strongly Interacting Rydberg Excitations of a Cold Atomic Gas". *Science* 336 (2012), pp. 887–889.

[67] Thibault Peyronel, Ofer Firstenberg, Qi-Yu Liang, Sebastian Hofferberth, Alexey V. Gorshkov, Thomas Pohl, Mikhail D. Lukin, and Vladan Vuletić. "Quantum nonlinear optics with single photons enabled by strongly interacting atoms". *Nature* 488 (2012), pp. 57–60.

[68] D. Maxwell, D. J. Szwer, D. Paredes-Barato, H. Busche, J. D. Pritchard, A. Gauguet, K. J. Weatherill, M. P. A. Jones, and C. S. Adams. "Storage and Control of Optical Photons Using Rydberg Polaritons". *Phys. Rev. Lett.* 110 (2013), p. 103001.

[69] Ofer Firstenberg, Thibault Peyronel, Qi-Yu Liang, Alexey V. Gorshkov, Mikhail D. Lukin, and Vladan Vuletić. "Attractive photons in a quantum nonlinear medium". *Nature* 502 (2013), pp. 71–75.

[70] Daniel Tiarks, Steffen Schmidt-Eberle, Thomas Stolz, Gerhard Rempe, and Stephan Dürr. "A photon–photon quantum gate based on Rydberg interactions". *Nat. Phys.* 15 (2018), pp. 124–126.

[71] Simon Baur, Daniel Tiarks, Gerhard Rempe, and Stephan Dürr. "Single-Photon Switch Based on Rydberg Blockade". *Phys. Rev. Lett.* 112 (2014), p. 073901.

[72] H. Gorniaczyk, C. Tresp, J. Schmidt, H. Fedder, and S. Hofferberth. "Single-Photon Transistor Mediated by Interstate Rydberg Interactions". *Phys. Rev. Lett.* 113 (2014), p. 053601.

[73] Daniel Tiarks, Simon Baur, Katharina Schneider, Stephan Dürr, and Gerhard Rempe. "Single-Photon Transistor Using a Förster Resonance". *Phys. Rev. Lett.* 113 (2014), p. 053602.

[74] H. Gorniaczyk, C. Tresp, P. Bienias, A. Paris-Mandoki, W. Li, I. Mirgorodskiy, H. P. Büchler, I. Lesanovsky, and S. Hofferberth. "Enhancement of Rydberg-mediated single-photon nonlinearities by electrically tuned Förster resonances". *Nat. Commun.* 7 (2016), p. 12480.

[75] Auxiliadora Padrón-Brito, Jan Lowinski, Pau Farrera, Klara Theophilo, and Hugues de Riedmatten. "Probing the indistinguishability of single photons generated by Rydberg atomic ensembles". *Phys. Rev. Research* 3 (2021), p. 033287.

[76] Fabian Ripka, Harald Kübler, Robert Löw, and Tilman Pfau. "A room-temperature single-photon source based on strongly interacting Rydberg atoms". *Science* 362 (2018), pp. 446–449.

[77] D. P. Ornelas-Huerta, A. N. Craddock, E. A. Goldschmidt, A. J. Hachtel, Y. Wang, P. Bienias, A. V. Gorshkov, S. L. Rolston, and J. V. Porto. "On-demand indistinguishable single photons from an efficient and pure source based on a Rydberg ensemble". *Optica* 7 (2020), pp. 813–819.

[78] Christoph Tresp, Christian Zimmer, Ivan Mirgorodskiy, Hannes Gorniaczyk, Asaf Paris-Mandoki, and Sebastian Hofferberth. "Single-photon absorber based on strongly interacting Rydberg atoms". *Phys. Rev. Lett.* 117 (2016), p. 223001.

[79] Q.H.F. Vrehen, M.F.H. Schuurmans, and D. Polder. "Superfluorescence: macroscopic quantum fluctuations in the time domain". *Nature* 285 (1980), pp. 70–71.

[80] Marlan O. Scully, Edward S. Fry, C. H. Raymond Ooi, and Krzysztof Wódkiewicz. "Directed Spontaneous Emission from an Extended Ensemble of N Atoms: Timing Is Everything". *Phys. Rev. Lett.* 96 (2006), p. 010501.

[81] Anatoly A Svidzinsky and Marlan O Scully. "Evolution of collective N atom states in single photon superradiance: Effect of virtual Lamb shift processes". *Opt. Commun.* 282 (2009), pp. 2894–2897.

[82] Anatoly A. Svidzinsky, Jun-Tao Chang, and Marlan O. Scully. "Cooperative spontaneous emission of N atoms: Many-body eigenstates, the effect of virtual Lamb shift processes, and analogy with radiation of N classical oscillators". *Phys. Rev. A* 81 (2010), p. 053821.

[83] Richard Friedberg and Jamal T Manassah. "Effects of including the counterrotating term and virtual photons on the eigenfunctions and eigenvalues of a scalar photon collective emission theory". *Phys. Lett. A* 372 (2008), pp. 2514–2521.

[84] Jamal T. Manassah. "The single photon superradiance from the eigenmode analysis". *Laser Phys.* 19 (2009), pp. 2102–2105.

[85] I. E. Mazets and G. Kurizki. "Multiatom cooperative emission following single-photon absorption: Dicke-state dynamics". *J. Phys. B: At. Mol. Opt. Phys* 40 (Mar. 2007), F105–F112.

[86] G. S. Agarwal. "Quantum-entanglement-initiated super Raman scattering". *Phys. Rev. A* 83 (2011), p. 023802.

[87] M. J. Stephen. "First-Order Dispersion Forces". *The Journal of Chemical Physics* 40 (1964), pp. 669–673.

[88] Edwin A. Power. "Effect on the Lifetime of an Atom Undergoing a Dipole Transition Due to the Presence of a Resonating Atom". *J. Chem. Phys.* 46 (1967), pp. 4297–4298.

[89] R. H. Lehmberg. "Radiation from an N-Atom System. II. Spontaneous Emission from a Pair of Atoms". *Phys. Rev. A* 2 (1970), pp. 889–896.

[90] R. G. Brewer. "Two-ion superradiance theory". *Phys. Rev. A* 52 (1995), pp. 2965–2970.

[91]   Daniel A. Steck. *Quantum and Atom Optics*. revision 0.13.10, 22 September 2021. 2007. eprint: `http://steck.us/teaching`.

[92]   Girish S. Agarwal. *Quantum Optics: Quantum Statistical Theories of Spontaneous Emission and their Relation to Other Approaches*. Vol. 70. Springer Tracts in Modern Physics. Springer Verlag, 1974.

[93]   S. J. Roof, K. J. Kemp, M. D. Havey, and I. M. Sokolov. "Observation of Single-Photon Superradiance and the Cooperative Lamb Shift in an Extended Sample of Cold Atoms". *Phys. Rev. Lett.* 117 (2016), p. 073003.

[94]   Jan Kumlin. "Collective Effects of Light-Matter Interactions in Rydberg Superatoms". PhD thesis. Universität Stuttgart, 2021.

[95]   M. Chalony, R. Pierrat, D. Delande, and D. Wilkowski. "Coherent flash of light emitted by a cold atomic cloud". *Phys. Rev. A* 84 (2011), p. 011401.

[96]   C. C. Kwong, T. Yang, M. S. Pramod, K. Pandey, D. Delande, R. Pierrat, and D. Wilkowski. "Cooperative Emission of a Coherent Superflash of Light". *Phys. Rev. Lett.* 113 (2014), p. 223601.

[97]   Z. Ficek and B. C. Sanders. "Quantum beats in two-atom resonance fluorescence". *Phys. Rev. A* 41 (1990), pp. 359–368.

[98]   Marlan O Scully and Anatoly A Svidzinsky. "The super of superradiance". *Science* 325 (2009), pp. 1510–1511.

[99]   Marlan O. Scully. "Single Photon Subradiance: Quantum Control of Spontaneous Emission and Ultrafast Readout". *Phys. Rev. Lett.* 115 (2015), p. 243602.

[100] Marlan O Scully. "Collective Lamb shift in single photon Dicke superradiance". *Phys. Rev. Lett.* 102 (2009), p. 143601.

[101] R. Wiegner, J. von Zanthier, and G. S. Agarwal. "Quantum-interference-initiated superradiant and subradiant emission from entangled atoms". *Phys. Rev. A* 84 (2011), p. 023805.

[102] R. Friedberg, S.R. Hartmann, and J.T. Manassah. "Frequency shifts in emission and absorption by resonant systems ot two-level atoms". *Phys. Rep.* 7 (1973), pp. 101–179.

[103] Philippe Grangier, Alain Aspect, and Jacques Vigue. "Quantum Interference Effect for Two Atoms Radiating a Single Photon". *Phys. Rev. Lett.* 54 (1985), pp. 418–421.

[104] Line Hjortshøj Pedersen and Klaus Mølmer. "Few qubit atom-light interfaces with collective encoding". *Phys. Rev. A* 79 (2009), p. 012320.

[105] Jan Kumlin, Sebastian Hofferberth, and Hans Peter Büchler. "Emergent universal dynamics for an atomic cloud coupled to an optical waveguide". *Phys. Rev. Lett.* 121 (2018), p. 013601.

[106] Robert J. Bettles, Simon A. Gardiner, and Charles S. Adams. "Cooperative eigenmodes and scattering in one-dimensional atomic arrays". *Phys. Rev. A* 94 (2016).

[107] Robert J. Bettles, Teodora Ilieva, Hannes Busche, Paul Huillery, Simon W. Ball, Nicholas L. R. Spong, and Charles S. Adams. *Collective Mode Interferences in Light–Matter Interactions*. 2018. arXiv: `1808.08415 [physics.atom-ph]`.

[108] D. D. Yavuz. "Superradiance as a source of collective decoherence in quantum computers". *J. Opt. Soc. Am. B* 31 (2014), p. 2665.

[109] Harry Levine, Alexander Keesling, Ahmed Omran, Hannes Bernien, Sylvain Schwartz, Alexander S. Zibrov, Manuel Endres, Markus Greiner, Vladan Vuleti ć, and Mikhail D. Lukin. "High-Fidelity Control and Entanglement of Rydberg-Atom Qubits". *Phys. Rev. Lett.* 121 (2018), p. 123603.

[110] M. Moreno-Cardoner, D. Goncalves, and D. E. Chang. "Quantum Nonlinear Optics Based on Two-Dimensional Rydberg Atom Arrays". *Phys. Rev. Lett.* 127 (2021), p. 263602.

[111] Lida Zhang, Valentin Walther, Klaus Mølmer, and Thomas Pohl. *Photon-photon interactions in Rydberg-atom arrays*. 2021. arXiv: `2101.11375 [quant-ph]`.

[112]   Alexandra S. Sheremet, Mihail I. Petrov, Ivan V. Iorsh, Alexander V. Poshakinskiy, and Alexander N. Poddubny. *Waveguide quantum electrodynamics: collective radiance and photon-photon correlations*. 2021. arXiv: 2103.06824 [quant-ph].

[113]   Hannes Pichler, Tomás Ramos, Andrew J. Daley, and Peter Zoller. "Quantum optics of chiral spin networks". *Phys. Rev. A* 91 (2015), p. 042116.

[114]   Sahand Mahmoodian, Mantas Čepulkovskis, Sumanta Das, Peter Lodahl, Klemens Hammerer, and Anders S. Sørensen. "Strongly Correlated Photon Transport in Waveguide Quantum Electrodynamics with Weakly Coupled Emitters". *Phys. Rev. Lett.* 121 (2018), p. 143601.

[115]   V. A. Pivovarov, L. V. Gerasimov, J. Berroir, T. Ray, J. Laurat, A. Urvoy, and D. V. Kupriyanov. "Single collective excitation of an atomic array trapped along a waveguide: A study of cooperative emission for different atomic chain configurations". *Phys. Rev. A* 103 (2021), p. 043716.

[116]   Jan Kumlin, Kevin Kleinbeck, Nina Stiesdal, Hannes Busche, Sebastian Hofferberth, and Hans Peter Büchler. "Nonexponential decay of a collective excitation in an atomic ensemble coupled to a one-dimensional waveguide". *Phys. Rev. A* 102 (2020), p. 063703.

[117]   P. R. Berman. "Theory of two atoms in a chiral waveguide". *Phys. Rev. A* 101 (2020), p. 013830.

[118]   D E Chang, L Jiang, A V Gorshkov, and H J Kimble. "Cavity QED with atomic mirrors". *New J. Phys.* 14 (2012), p. 063003.

[119]   Thomas Gallagher. *Rydberg atoms.* Cambridge Monographs on Atomic, Molecular, and Chemical Physics 3. Cambridge University Press, 1994.

[120]   Christoph Tresp. "Rydberg polaritons and Rydberg superatoms – novel tools for quantum nonlinear optics". PhD thesis. Universität Stuttgart, 2017.

[121]   E Brion, L H Pedersen, and K Mølmer. "Adiabatic elimination in a lambda system". *J. Phys. A: Math. Theor.* 40 (2007), pp. 1033–1043.

[122]   Michael Fleischhauer, Atac Imamoglu, and Jonathan P. Marangos. "Electromagnetically induced transparency: Optics in coherent media". *Rev. Mod. Phys.* 77 (2005), pp. 633–673.

[123]   Lene Vestergaard Hau, S. E. Harris, Zachary Dutton, and Cyrus H. Behroozi. "Light speed reduction to 17 metres per second in an ultracold atomic gas". *Nature* 397 (1999), pp. 594–598.

[124]   M. Fleischhauer and M. D. Lukin. "Dark-State Polaritons in Electromagnetically Induced Transparency". *Phys. Rev. Lett.* 84 (2000), pp. 5094–5097.

[125]   Sebastian Weber, Christoph Tresp, Henri Menke, Alban Urvoy, Ofer Firstenberg, Hans Peter Büchler, and Sebastian Hofferberth. "Calculation of Rydberg interaction potentials". *J. Phys. B: At. Mol. Opt. Phys.* 50 (2017), p. 133001.

[126]   M. D. Lukin, M. Fleischhauer, R. Cote, L. M. Duan, D. Jaksch, J. I. Cirac, and P. Zoller. "Dipole Blockade and Quantum Information Processing in Mesoscopic Atomic Ensembles". *Phys. Rev. Lett.* 87 (2001), p. 037901.

[127]   D. Tong, S. M. Farooqi, J. Stanojevic, S. Krishnan, Y. P. Zhang, R. Côté, E. E. Eyler, and P. L. Gould. "Local Blockade of Rydberg Excitation in an Ultracold Gas". *Phys. Rev. Lett.* 93 (2004), p. 063001.

[128]   Kilian Singer, Markus Reetz-Lamour, Thomas Amthor, Luis Gustavo Marcassa, and Matthias Weidemüller. "Suppression of Excitation and Spectral Broadening Induced by Interactions in a Cold Gas of Rydberg Atoms". *Phys. Rev. Lett.* 93 (2004), p. 163001.

[129]   Rolf Heidemann, Ulrich Raitzsch, Vera Bendkowsky, Björn Butscher, Robert Löw, Luis Santos, and Tilman Pfau. "Evidence for Coherent Collective Rydberg Excitation in the Strong Blockade Regime". *Phys. Rev. Lett.* 99 (2007), p. 163601.

[130]   E. Urban, T. A. Johnson, T. Henage, L. Isenhower, D. D. Yavuz, T. G. Walker, and M. Saffman. "Observation of Rydberg blockade between two atoms". *Nat. Phys.* 5 (2009), pp. 110–114.

[131] Alpha Gaëtan, Yevhen Miroshnychenko, Tatjana Wilk, Amodsen Chotia, Matthieu Viteau, Daniel Comparat, Pierre Pillet, Antoine Browaeys, and Philippe Grangier. "Observation of collective excitation of two individual atoms in the Rydberg blockade regime". *Nat. Phys.* 5 (2009), pp. 115–118.

[132] Chris H. Greene, A. S. Dickinson, and H. R. Sadeghpour. "Creation of Polar and Nonpolar Ultra-Long-Range Rydberg Molecules". *Phys. Rev. Lett.* 85 (2000), pp. 2458–2461.

[133] Vera Bendkowsky, Björn Butscher, Johannes Nipper, James P. Shaffer, Robert Löw, and Tilman Pfau. "Observation of ultralong-range Rydberg molecules". *Nature* 458 (2009), pp. 1005–1008.

[134] A. Gaj, A. T. Krupp, J. B. Balewski, R. Löw, S. Hofferberth, and T. Pfau. "From molecular spectra to a density shift in dense Rydberg gases". *Nat. Commun.* 5 (2014), p. 4546.

[135] N. Šibalić, J.D. Pritchard, C.S. Adams, and K.J. Weatherill. "ARC: An open-source library for calculating properties of alkali Rydberg atoms". *Comput. Phys. Commun.* 220 (2017), pp. 319–331.

[136] Sergio H Cantu, Aditya V Venkatramani, Wenchao Xu, Leo Zhou, Brana Jelenković, Mikhail D Lukin, and Vladan Vuletić. "Repulsive photons in a quantum nonlinear medium". *Nat. Phys.* 16 (2020), pp. 921–925.

[137] Callum R Murray and Thomas Pohl. "Coherent photon manipulation in interacting atomic ensembles". *Phys. Rev. X* 7 (2017), p. 031007.

[138] Annika Tebben, Clément Hainaut, Andre Salzinger, Titus Franz, Sebastian Geier, Gerhard Zürn, and Matthias Weidemüller. *A stationary Rydberg polariton*. 2021. arXiv: 2108.00657 [quant-ph].

[139] Vladan Vuletic. "When superatoms talk photons". *Nat. Phys.* 2 (2006), pp. 801–802.

[140] D. Felinto, C. W. Chou, J. Laurat, E. W. Schomburg, H. de Riedmatten, and H. J. Kimble. "Conditional control of the quantum states of remote atomic memories for quantum networking". *Nat. Phys.* 2 (2006), pp. 844–848.

[141] Christoph Braun. "Free-space Quantum Electrodynamics with a single Rydberg superatom". Master thesis. Universität Stuttgart, 2017.

[142] Nina Stiesdal. "Intrinsic three photon correlations mediated by a single Rydberg superatom". Master thesis. University of Southern Denmark, 2018.

[143] Nina Stiesdal, Jan Kumlin, Kevin Kleinbeck, Philipp Lunt, Christoph Braun, Asaf Paris-Mandoki, Christoph Tresp, Hans Peter Büchler, and Sebastian Hofferberth. "Observation of Three-Body Correlations for Photons Coupled to a Rydberg Superatom". *Phys. Rev. Lett.* 121 (2018), p. 103601.

[144] Hannes Gorniaczyk. "Single photon transistor mediated by electrically tunable Rydberg-Rydberg interactions". PhD thesis. Universität Stuttgart, 2016.

[145] Florian Christaller. "Construction and setup of a 3rd generation Rydberg Quantum Optics experiment". Master thesis. Universität Stuttgart, 2017.

[146] Johannes Schmidt. "Generation of non-classical light using ultra-cold Rydberg ensembles". Master thesis. Universität Stuttgart, 2014.

[147] Rudolf Grimm, Matthias Weidemüller, and Yurii B. Ovchinnikov. "Optical Dipole Traps for Neutral Atoms". *Advances In Atomic, Molecular, and Optical Physics*. Elsevier, 2000, pp. 95–170.

[148] R. Hanbury Brown and R. Q. Twiss. "Correlation between Photons in two Coherent Beams of Light". *Nature* 177 (1956), pp. 27–29.

[149] Markus Koch, Christian Sames, Maximilian Balbach, Haytham Chibani, Alexander Kubanek, Karim Murr, Tatjana Wilk, and Gerhard Rempe. "Three-Photon Correlations in a Strongly Driven Atom-Cavity System". *Phys. Rev. Lett.* 107 (2011), p. 023601.

[150] C. Ates, I. Lesanovsky, C. S. Adams, and K. J. Weatherill. "Fast and Quasideterministic Single Ion Source from a Dipole-Blockaded Atomic Ensemble". *Phys. Rev. Lett.* 110 (2013), p. 213003.

[151] K. O. Roberts, T. McKellar, J. Fekete, A. Rakonjac, A. B. Deb, and N. Kjærgaard. "Steerable optical tweezers for ultracold atom studies". *Opt. Lett.* 39 (2014), pp. 2012–2015.

[152] Qi-Yu Liang, Aditya V Venkatramani, Sergio H Cantu, Travis L Nicholson, Michael J Gullans, Alexey V Gorshkov, Jeff D Thompson, Cheng Chin, Mikhail D Lukin, and Vladan Vuletić. "Observation of three-photon bound states in a quantum nonlinear medium". *Science* 359 (2018), pp. 783–786.

[153] Kevin Kleinbeck. "Quantum Light Interaction with Superatoms". Master thesis. Universität Stuttgart, 2017.

[154] Gerd Leuchs and Markus Sondermann. "Light–matter interaction in free space". *J. Mod. Opt.* 60 (2013), pp. 36–42.

[155] J.R. Johansson, P.D. Nation, and Franco Nori. "QuTiP: An open-source Python framework for the dynamics of open quantum systems". *Comput. Phys. Commun.* 183 (2012), pp. 1760–1772.

[156] Nina Stiesdal, Hannes Busche, Jan Kumlin, Kevin Kleinbeck, Hans Peter Büchler, and Sebastian Hofferberth. "Observation of collective decay dynamics of a single Rydberg superatom". *Phys. Rev. Research* 2 (2020), p. 043339.

[157] Antoine Glicenstein, Giovanni Ferioli, Antoine Browaeys, and Igor Ferrier-Barbut. *From superradiance to subradiance: exploring the many-body Dicke ladder*. 2021. arXiv: `2112.10635 [quant-ph]`.

[158] T. S. do Espirito Santo, P. Weiss, A. Cipris, R. Kaiser, W. Guerin, R. Bachelard, and J. Schachenmayer. "Collective excitation dynamics of a cold atom cloud". *Phys. Rev. A* 101 (2020), p. 013617.

[159] Jens Honer, R. Löw, Hendrik Weimer, Tilman Pfau, and Hans Peter Büchler. "Artificial Atoms Can Do More Than Atoms: Deterministic Single Photon Subtraction from Arbitrary Light Fields". *Phys. Rev. Lett.* 107 (2011), p. 093601.

[160] Giovanni Ferioli, Antoine Glicenstein, Loic Henriet, Igor Ferrier-Barbut, and Antoine Browaeys. "Storage and Release of Subradiant Excitations in a Dense Atomic Cloud". *Phys. Rev. X* 11 (2021), p. 021031.

[161] Jaromír Fiurášek, Raúl García-Patrón, and Nicolas J. Cerf. "Conditional generation of arbitrary single-mode quantum states of light by repeated photon subtractions". *Phys. Rev. A* 72 (2005), p. 033822.

[162] G. J. Milburn. "Quantum optical Fredkin gate". *Phys. Rev. Lett.* 62 (1989), pp. 2124–2127.

[163] J. S. Neergaard-Nielsen, B. Melholt Nielsen, C. Hettich, K. Mølmer, and E. S. Polzik. "Generation of a Superposition of Odd Photon Number States for Quantum Information Networks". *Phys. Rev. Lett.* 97 (2006), p. 083604.

[164] Alexei Ourjoumtsev, Rosa Tualle-Brouri, Julien Laurat, and Philippe Grangier. "Generating Optical Schrödinger Kittens for Quantum Information Processing". *Science* 312 (2006), pp. 83–86.

[165] Daniel Braun, Pu Jian, Olivier Pinel, and Nicolas Treps. "Precision measurements with photon-subtracted or photon-added Gaussian states". *Phys. Rev. A* 90 (2014), p. 013821.

[166] D. Pinotsi and A. Imamoglu. "Single Photon Absorption by a Single Quantum Emitter". *Phys. Rev. Lett.* 100 (2008), p. 093603.

[167] Io-Chun Hoi, Anton F. Kockum, Tauno Palomaki, Thomas M. Stace, Bixuan Fan, Lars Tornberg, Sankar R. Sathyamoorthy, Göran Johansson, Per Delsing, and C. M. Wilson. "Giant Cross–Kerr Effect for Propagating Microwaves Induced by an Artificial Atom". *Phys. Rev. Lett.* 111 (2013), p. 053601.

[168] Julio Gea-Banacloche and William Wilson. "Photon subtraction and addition by a three-level atom in an optical cavity". *Phys. Rev. A* 88 (2013), p. 033832.

[169] Serge Rosenblum, Orel Bechler, Itay Shomroni, Yulia Lovsky, Gabriel Guendelman, and Barak Dayan. "Extraction of a single photon from an optical pulse". *Nat. Photon.* 10 (2015), pp. 19–22.

[170] Nina Stiesdal, Hannes Busche, Kevin Kleinbeck, Jan Kumlin, Mikkel G. Hansen, Hans Peter Büchler, and Sebastian Hofferberth. "Controlled multi-photon subtraction with cascaded Rydberg superatoms as single-photon absorbers". *Nat. Commun.* 12 (2021), p. 4328.

[171] F. Bariani, Paul M. Goldbart, and T. A. B. Kennedy. "Dephasing dynamics of Rydberg atom spin waves". *Phys. Rev. A* 86 (2012), p. 041802.

[172] Hannes Busche, Paul Huillery, Simon W. Ball, Teodora Ilieva, Matthew P. A. Jones, and Charles S. Adams. "Contactless nonlinear optics mediated by long-range Rydberg interactions". *Nat. Phys.* 13 (2017), pp. 655–658.

[173] Leonard Mandel. "Sub-Poissonian photon statistics in resonance fluorescence". *Opt. Lett.* 4 (1979), pp. 205–207.

[174] C. Ates, T. Pohl, T. Pattard, and J. M. Rost. "Antiblockade in Rydberg Excitation of an Ultracold Lattice Gas". *Phys. Rev. Lett.* 98 (2007), p. 023002.

[175] Thomas Amthor, Christian Giese, Christoph S. Hofmann, and Matthias Weidemüller. "Evidence of Antiblockade in an Ultracold Rydberg Gas". *Phys. Rev. Lett.* 104 (2010), p. 013001.

[176] S Wüster and J-M Rost. "Rydberg aggregates". *J. Phys. B: At. Mol. Opt. Phys.* 51 (2018), p. 032001.

[177] Jinjin Du, Wenfang Li, and Michal Bajcsy. "Deterministic single-photon subtraction based on a coupled single quantum dot-cavity system". *Opt. Express* 28 (2020), pp. 6835–6845.

[178] B. Olmos, W. Li, S. Hofferberth, and I. Lesanovsky. "Amplifying single impurities immersed in a gas of ultracold atoms". *Phys. Rev. A* 84 (2011), p. 041607.

[179] G. Günter, M. Robert-de-Saint-Vincent, H. Schempp, C. S. Hofmann, S. Whitlock, and M. Weidemüller. "Interaction Enhanced Imaging of Individual Rydberg Atoms in Dense Gases". *Phys. Rev. Lett.* 108 (2012), p. 013002.

[180] G. Günter, H. Schempp, M. Robert-de-Saint-Vincent, V. Gavryusev, S. Helmrich, C. S. Hofmann, S. Whitlock, and M. Weidemüller. "Observing the Dynamics of Dipole-Mediated Energy Transport by Interaction-Enhanced Imaging". *Science* 342 (2013), pp. 954–956.

[181] J. Lampen, H. Nguyen, L. Li, P. R. Berman, and A. Kuzmich. "Long-lived coherence between ground and Rydberg levels in a magic-wavelength lattice". *Phys. Rev. A* 98 (2018), p. 033411.

[182] Nicholas L. R. Spong, Yuechun Jiao, Oliver D. W. Hughes, Kevin J. Weatherill, Igor Lesanovsky, and Charles S. Adams. "Collectively Encoded Rydberg Qubit". *Phys. Rev. Lett.* 127 (2021), p. 063604.

[183] Wenchao Xu, Aditya V. Venkatramani, Sergio H. Cantú, Tamara Šumarac, Valentin Klüsener, Mikhail D. Lukin, and Vladan Vuletić. "Fast Preparation and Detection of a Rydberg Qubit Using Atomic Ensembles". *Phys. Rev. Lett.* 127 (2021), p. 050501.

[184] Julien Vaneecloo, Sébastien Garcia, and Alexei Ourjoumtsev. *An Intracavity Rydberg Superatom for Optical Quantum Engineering: Coherent Control, Single-Shot Detection and Optical π Phase Shift.* 2021. arXiv, to appear in PRX: `2111.09088` (quant-ph).

[185] Peng-Fei Sun, Yong Yu, Zi-Ye An, Jun Li, Chao-Wei Yang, Xiao-Hui Bao, and Jian-Wei Pan. "Deterministic Time-Bin Entanglement between a Single Photon and an Atomic Ensemble". *Phys. Rev. Lett.* 128 (2022), p. 060502.

Acknowledgement

The research presented here was done during the pandemic, and I hand in at a point in time where the world I grew up in seems to change dramatically from day to day, from hour to hour. Yet, I hope you can read between the lines in the previous chapters that I greatly enjoyed doing the work that went into this thesis. This is in part because fundamental physics makes good fun, but also, and maybe primarily, because I had the pleasure to always be surrounded by the most amazing people, both in my work and in my private life.

I work with light, my colleagues are bright, and my friends are radiant! I am grateful beyond words.

I would like to mention some of the people[1] who are making every day special for me[2].

Firstly, my family! My parents - I really won the parent-lottery, I got the best ones - and I ALSO have Pernille og Patricia, mormor, farmor og Tove. Godt, vi har hinanden.

Then, without many names I am here also thinking of all my lovely friends! In particular a bunch of girls, ladies, chickas all around the world, at and outside of the university. My Rugby girlz, my sweetest lil WG-wife, Alessa, and the coolest neighbor in the world, Nora[3], have all dealt with a LOT of my PhD- and thesis-madness. Thank you!

I also think of all the physicists at SDU and Uni Bonn who have taught me so much and inspired me in so many ways. These count in particular Richard who provided amazing support during this work, and Santhosh, whose moral support never failed. Also, at SDU I got to know the coolest chemists.

I have also had the pleasure to work with the kindest and friendliest administration: Tina, Sanne, Mette, Suba, Danny, and Dietmar have in particular helped make this PhD project a pleasure.

Some theoreticians should also be mentioned! I am happy that I know and work with the Hans-Peter Büchler, Jan Kumlin, and Kevin Kleinbeck. Jan and Kevin, you may not know it, but I consider you 'my' theoreticians - But if I have a say, you can come work with me in the

---

[1] A lot of equipment also gave me special days! I would actually like to dedicate this little footnote as a thank you for your service to some pieces of equipment, both the stupid piece of crap-machine-devices, and the always-well-behaved pieces. Everything worked when it had to. Rest assured, dear devices, that I will pat y'all gently when I'm back in the lab.

[2] You may notice that I have the best parents, the sweetest friends, and the coolest supervisor. What can I say? I am very lucky!

[3] Whose favorite waveguide is a surf instructor, btw!

lab ANY day if the calculations get too trivial! Thomas Pohl and Lida Zhang are excellent company. Our first excursion went to the world of vapor cells, I look forward to seeing where we will go next.

The research presented here could not have taken place without amazing group-members, current, and former. These count the ytterbium team, and the fiber-team, and my former team-mates. including Mikkel Gaard Have and Mogens From, my master masters! I thought, I should teach you, but you taught me a lot.

Finally, my daily dream team: Julia Gamper, Eduardo Urunuela, Cedric Style Wind, Hannes Busche, and Lukas Ahlheit.

Julia always cheers me up. Thank you, Julia, for bringing warmth and humor to the team. For every handwritten note, for persisting in talking German with me, and for every excellent question about physics. I look forward to your talk tomorrow, and for fun and work with you in the future.

Eduardo is the best office mate in the world! Despite the window-open/window-closed discussion. I really look forward to the next deep talk, and for lots of future

$$pro\frac{gress + crastination}{\sqrt{2}}.$$

Cedric is my buddy for every occasion. Running, gym, board games, beer, and fundamental physics, you name it! You are one in a melon ;)

Lukas is my amazing lab-mate and friend. I like it when you laugh. I put a lot of $\heartsuit$ into this lab, please take good care of it.

Hannes. Without Hannes this thesis would not have existed. Hannes, I may not be the best at saying it out loud, but you are totally **awesome**. Thank you for being my friend, thank you for everything. I know that we are the most kickass team. We managed broken lasers, moves, Ikea trips, beer, jogging, physics, and now this thesis. I look very much up to you, and I feel very privileged to know that I can call you up (even at odd times) and just say 'Hannes, say it will all be OK!'. You, Hannes, make it OK.

Last, but not least, I would not have bothered doing this without Sebastian Hofferberth. It's been quite a while now, and I am still very thankful that you gave me the option to join the team. I am very happy to have a PhD supervisor - a Doctorvater - who is also a whole human being. Thank you for being present, and for sharing good days and bad days with me. For sending me memes, bruh! Sometimes fellow students tell me 'wow, your supervisor is really cool', and I can only say 'Yeah, I know'.

Thank you for being my excellent boss, colleague, mentor, and friend.